ULTRAFAST ENERGY DYNAMICS OF TWO DIMENSIONAL SEMICONDUCTING AND TOPOLOGICAL MATERIALS

by

Vasudevan Rajagopal Iyer

A Dissertation

Submitted to the Faculty of Purdue University

In Partial Fulfillment of the Requirements for the degree of

Doctor of Philosophy

School of Mechanical Engineering

West Lafayette, Indiana

May 2020

THE PURDUE UNIVERSITY GRADUATE SCHOOL
STATEMENT OF COMMITTEE APPROVAL

Dr. Xianfan Xu, Chair

School of Mechanical Engineering

Dr. Ali Shakouri

School of Electrical and Computer Engineering

Dr. Yong P. Chen

Department of Physics and Astronomy
&
School of Electrical and Computer Engineering

Dr. Amy Marconnet

School of Mechanical Engineering

Approved by:

Dr. Nicole Key

Head of the Graduate Program

To my parents

ACKNOWLEDGMENTS

I would first like to thank my advisor, Prof. Xianfan Xu for his wonderful guidance and support. He has provided me with the perfect balance of research freedom along with timely directions when I went astray. His deep intuition of experimental techniques and patience during the setup phases helped me obtain meaningful data. He has always given me the opportunity to work with interesting research problems. I express my gratitude to Prof. Ali Shakouri, Prof. Yong Chen and Prof. Amy Marconnet for agreeing to serve on my committee. I have learnt much from collaborative projects with Prof. Peide Ye, Prof. Liang Pan and Prof. Bryan Boudouris, for which I am very grateful. I also thank Prof. Andy Weiner, Prof. Tim Fisher and Prof Zubin Jacob, whose courses laid a solid foundation for my work and inspired me to take up challenging research problems.

I am happy to have an excellent group of friends and colleagues who constantly encourage me both professionally and personally and have provided their support in all matters during my stay at Purdue. My thanks to Prabhu Kumar, Dr. Anurup Datta, Shouyuan Huang, Paul Sommers, Hakan Salihoglu and Mauricio Segovia for help with device fabrication, AFM and many discussions on matters big and small. I would like to thank Dr. Liang Guo, Qiaomu Yao, Dr. Alexei Lagoutchev and Dr. Roger Luo for teaching me many of the experimental techniques and concepts. My sincerest thanks to Maj. Dr. Levi Thomas and Dr. Aman Satija for letting me learn from their experimental facility on numerous occasions. Shout out to Dr. Adam Huss for keeping our lasers in top shape. Again, without my friends at the Birck center, Harsha, Punya, Vaibhav, Rahul, Krishnakali, Emroz, Aveek and many others, the learning would be incomplete. The staff at Birck, especially Mary Jo, have been very supportive and helpful throughout. Outside the lab, my friends Dheeraj, Vaidehi, Pramod, Akash, Devah, Sridhar, Tejasvi, Aalok, Akshay, Shivaram, Tapasvi and so many more have made me feel at home, though I was in a new and unfamiliar land. My special thanks to Prof. Amit Varma, who has been a long time mentor.

I would like to express deep gratitude to my parents for having lovingly supported and encouraged me in all my life's undertakings. Their constant efforts for my sake are the reason for my achievements so far. Finally, I thank my wonderful sister, brother-in-law, and my delightful niece for the love and all the fun times.

TABLE OF CONTENTS

LIST OF TABLES

LIST OF FIGURES

ABSTRACT

Invention of the transistor in the 1950s marked a revolution in the history of scientific advancement. Today, our lives are propelled by the tremendous power of electronics which is within everyone's reach. This has been possible due to the thorough understanding of the transistor and other related electronic components. Silicon, which is abundantly available in nature, has been the material of choice for fabricating most of the electronic components we use today. It is a very robust and well performing semiconductor. However, we are reaching a stage where silicon electronics can no longer be improved, and the scientific community is keenly looking for alternatives to achieve continued progress.

The search for faster computing and better electronic devices has led to the opening up of several promising routes, which are being actively researched. These include spintronics, valleytronics, topological computing, quantum computing and exotic two-dimensional (2D) material based systems, to name a few. Each field has seen a tremendous amount of effort in the past decade. Broadly, this thesis explores some of the fundamental aspects of 2D semiconducting and topological materials, via an optical spectroscopy approach. The technique of choice is femtosecond ultrafast pump and probe laser spectroscopy, which has proven to be a powerful tool for investigating fundamental microscopic phenomena.

First, we look at emerging 2D materials, black phosphorus and tellurium, which have useful properties such as anisotropic electronic and optical response, good carrier mobility and direct bandgap. Black phosphorus and tellurium are Van der Waals materials, similar to graphene and hence can be cleaved using scotch tape or in liquid phase to obtain thin samples. In this work, a 65 nm black phosphorus flake was obtained and its relaxation following optical excitation was probed from near-infrared (1500 nm) to mid-infrared (4500 nm) wavelengths. The bandgap of the material was clearly resolved and relaxation times in the sub 100 ps range was observed. Wavelength dependent electron-phonon coupling and recombination was observed, which points to the importance of choosing the correct probing energies in ultrafast experiments. An upper estimate of the carrier mobility was obtained from the extracted electron-phonon scattering time. Moreover, the spectral evolution of reflectance was used to obtain hot carrier relaxation times by modeling with a Fermi-Dirac distribution. Lastly, surface oxidation effects were proposed to explain anomalous features in the transient data.

Tellurium flakes with thicknesses ranging from 12 nm to 160 nm were obtained by solution growth and a strong dependence of the recombination times on thickness was observed. Thin flakes show a fast decay on the order of 20 ps, whereas thicker flakes have a decay in the 100s of ps range. The recombination mechanism in thin flakes was attributed to fast carrier capture by mid-gap defect states arising from surface defects and that in the thick flakes to radiative recombination. Recombination coefficients were extracted using a diffusion-recombination model. A surface and bulk scattering model was used to qualitatively explain the observed thickness dependent field effect mobilities in literature.

Next, we look at another emerging material, Bi_2Te_2Se (BTS221). This material is a Van der Waals topological insulator and can be cleaved using scotch tape. Similar to black phosphorus and tellurium, BTS221 is also a direct band gap semiconductor, with a comparable bandgap. However, BTS221 possesses an exotic property due to its topological nature. It has Dirac like energy states on the surface, crossing the bandgap. This makes it metallic on the surface and semiconducting in the bulk. Hence, the term topological insulator. Here, mid-infrared, helicity resolved pump-probe spectroscopy was performed to couple light with the surface states, thereby generating transient spin-currents due to the spin-momentum locking feature of the surface. It was found that thin flakes (<20 nm) responded strongly and produced long lasting spin lifetimes in the 10 ps range. The findings were supplemented by Hall measurements and helicity dependent photocurrent measurements. The experiments revealed that BTS221 can be a very promising candidate for spintronic applications. Alongside, coherent phonons in the material were also launched and detected for varying flake thickness and one of the Raman modes could be observed in thicker flakes.

Furthermore, using topological insulator for switching magnets has been attempted. Optically excited spins in TIs can be transferred to ferromagnets in close proximity, eventually leading to the flipping of the magnet for strong light fields. A magneto-optic Kerr effect system is built to monitor the magnetization state of the ferromagnet. Hence, an all-optical switching and detection scheme is used. Preliminary results have been obtained. Lastly, studies were performed with a scanning pump-probe setup to monitor the ambipolar carrier diffusion in a variety of materials. For example, an attempt to distinguish the surface and bulk state diffusion properties of TIs is attempted. Thin flakes were back gated to manipulate the Fermi-level and increase or decrease the surface state contribution. Unconventional effects were observed.

1. INTRODUCTION

Solid state physics is one of the most widely studied fields in engineering and physics, due to its widespread applications in everyday human life. Much of the progress in numerous areas is directly due to the improved understanding and application of the theory of solids. These include computers, portable electronics, healthcare devices, satellite components, aircraft components and lasers to name a few. It is therefore extremely important to obtain microscopic as well as macroscopic, steady as well as transient properties of the materials which make up these solid state devices. To this end, several characterization techniques are in place such as electrical two/four probing, hall measurement, electron and optical microscopy, x-ray diffraction, atomic force microscopy to name a few. Ultrafast femtosecond spectroscopy is another versatile technique to study the microscopic transport properties of almost all classes of solid state materials such as metals, semiconductors, insulators and semi-metals. A plethora of important phenomena such as electron-phonon coupling, electron scattering, phonon scattering and electron recombination take place on the femtosecond to nanosecond timescales. The fastest available electronics cannot exceed the GHz to low THz speeds and hence a method, not based on electronics, is required to study the above mentioned phenomena. Optical femtosecond spectroscopy can satisfy these requirements and has therefore been used for over five decades, starting shortly after the invention of ultrafast lasers in the early 1970s. This thesis is centered on using the ultrafast optical technique to study semiconducting and topological two-dimensional materials of technological interest. In the following sections, the basics of band theory, which is central to solid state physics will be introduced, followed by a brief overview of two-dimensional materials and then a review of black phosphorus, tellurium and Bi_2Te_2Se, which are investigated in this thesis. The chapter will conclude with an explanation of the ultrafast optical technique and typical results obtained in literature for more widely studied materials such as graphene, MoS_2, metals and bulk semiconductors.

1.1 Band theory in solids

This section provides a brief overview of band theory and is based on the textbooks Solid State Physics by Ashcroft and Mermin [1], and Introduction to Solid State Physics by Kittel [2].

Consider the simplest atom, hydrogen. It consists of one proton and one electron. The electron's behavior is described quantum mechanically. The time independent Schrödinger's equation can be solved to obtain the energy levels (orbitals) of the electrons. The spatial distribution of the electron wavefunction can also be readily obtained. Figure 1.1a shows the discrete energy levels in a simple atom such as hydrogen, where the potential experienced by the electron due to the proton is well shaped.

As atoms bond together and forms molecules and finally solids, the potential experienced by the electrons becomes more complicated. Figure 1.1b shows the situation for two atom molecule, where each energy level (orbital) is split into two to allow for Pauli's exclusion principle, i.e. two electrons cannot have the exact same energy. When the number of atoms is very large (Figure 1.1c), the energy levels are split into a continuous band to accommodate all the bonding electrons. The outermost occupied band is usually called the conduction band and electrons are free to move about in the entire crystal in this band. The lower energy electrons are typically confined closer to their parent atom.

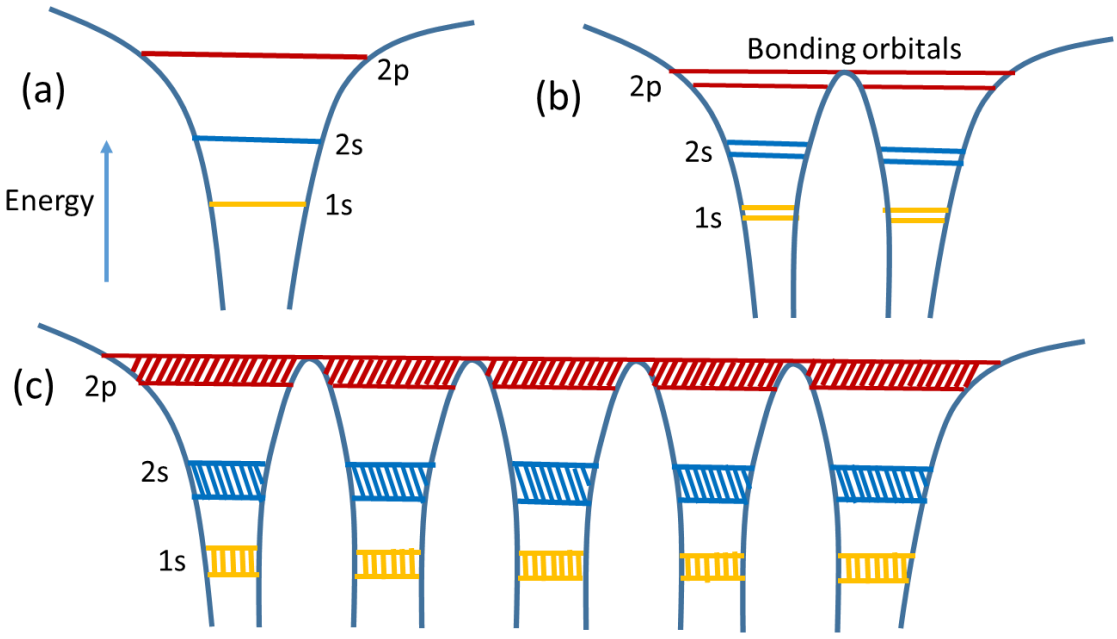

Figure 1.1: Formation of bands in solids, (a) a single atom is considered as a potential energy well and electrons occupy discrete energy levels as in hydrogen, (b) two atom bond, each energy level (orbital) is split into two and (c) solid with many atoms, where an almost continuous band of energies is formed in each orbital (colored shaded regions). The outermost band usually contains electrons that are delocalized throughout the crystal.

The well-known classification of solids into insulators, metals and semi-conductors can be understood using the band theory. Insulators have a filled valence band and an empty conduction band at 0 K. Due to the very large band gap, very few electrons are thermally excited into the conduction band at low/room temperatures and hence they show poor electrical conductivity. Metals on the other hand, have half-filled conduction band at 0 K and a spread around the Fermi-level at room temperature, which makes them excellent conductors. Semi-conductors are like insulators in the sense that they have no electrons in the conduction band at 0K but due to their smaller bandgap and externally induced dopants, they have a sizable number of electrons in the conduction band at higher temperatures. Hence the name semiconductors. A depiction of the band filling is shown in Figure 1.2. Furthermore, when semi-conductors are doped with other atoms, that replace some of the atoms in the lattice, the materials is called an extrinsic semiconductor. The doping process increases the carrier concentration and improves conductivity.

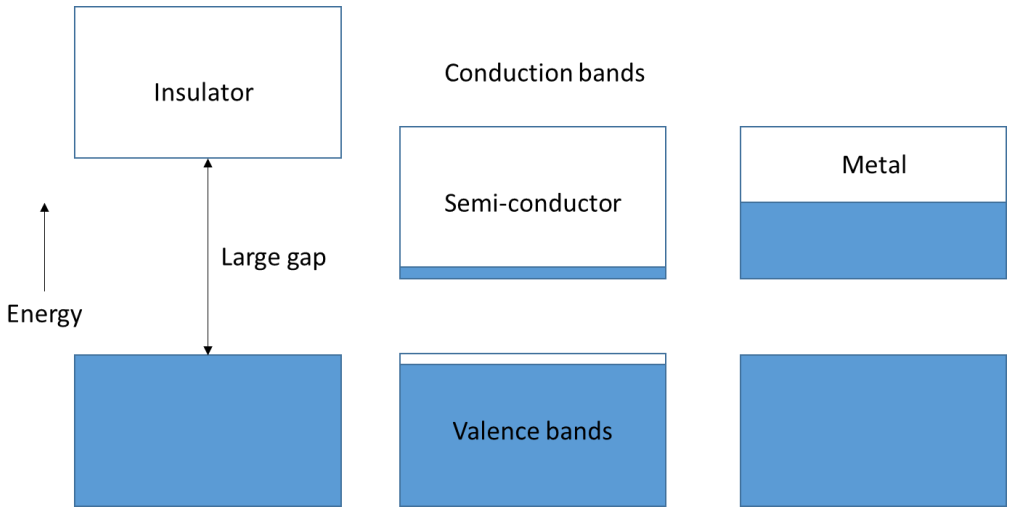

Figure 1.2: Band filling in insulator, semi-conductor and metal. Large gap between valence and conduction band prevents thermal excitation of electrons in insulator. Semi-conductors have sizable electron population in the conduction band. Metals have their conduction band half filled.

Quantum mechanically, an electron moving in free space can be represented by a wavefunction as follows:

$$\psi_k(\boldsymbol{r}) = \exp(i\boldsymbol{k}.\boldsymbol{r}) \tag{1-1}$$

Here *k* is the wavevector of the electron, which is a vector pointing in the direction of the electron's motion and having a magnitude that is 1/wavelength. The wavevector *k* may take any magnitude and direction.

Every crystalline solid occurs in a particular crystal structure, i.e. lattice, and has a corresponding reciprocal lattice, which can describe the energy distribution of electrons. For example, the real space lattice and reciprocal lattice for GaAs is shown in Figure 1.3 [3].

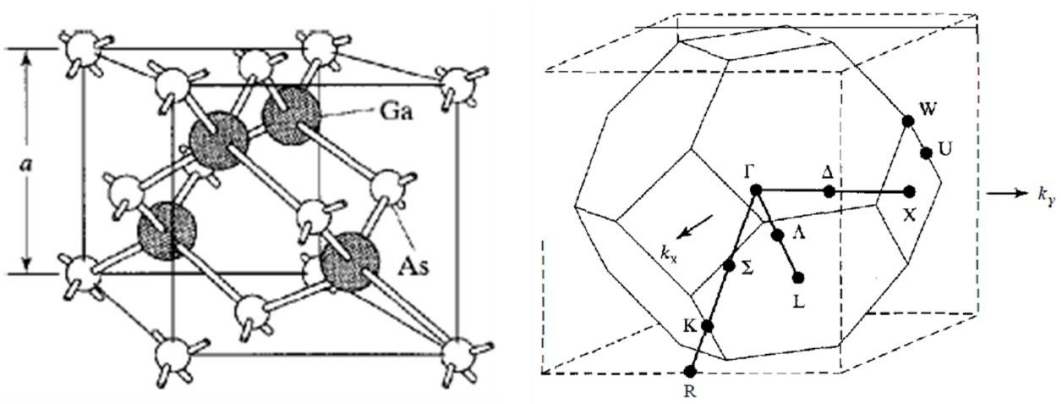

Figure 1.3: Real space arrangement of atoms (left) and reciprocal space (right) for GaAs, which has a zinc blend structure [3]. Both the real space lattice and reciprocal lattice are periodic.

Unlike a free electron, an electron present in a crystal lattice experiences a periodic potential due to the regular arrangement of the positively charged nucleus. Bloch proposed that the wavefunction of the electron would be modified in the lattice due to the periodic potential and take the following form:

$$\psi_{nk}(\boldsymbol{r}) = e^{i\boldsymbol{k}.\boldsymbol{r}} u_{nk}(\boldsymbol{r}) \tag{1-2}$$

u_{nk} is a function that has a periodicity of the Bravais lattice (reciprocal lattice). For a given wavevector *k*, there exists multiple allowed energy states represented by *n*. Conversely, each energy band *n* is described by a wavefuntion ψ_k. This function is used in the single particle, non-relativistic, time independent Schrodinger equation to obtain the energy distribution of electrons:

$$\left[-\frac{\hbar^2}{2m}\nabla^2 + V(r)\right]\psi(r) = E\psi(r) \tag{1-3}$$

An appropriate form for the function u_{nk}, and potential V(r) must be chosen, both of which depends on the model used, such as the tight binding, Kronig Penny etc. The solutions for real materials are usually obtained computationally and methods such as density functional theory

(DFT) have almost become a standard method to calculate the band structure of materials. As the end result, an energy vs wavevector in 3D reciprocal space is obtained, as we would expect from Equation 1-3. Since u_{nk} is a function of n and k, we obtain multiple solutions for each k, which correspond to successive bands. Since a four-dimensional E vs k cannot be visualized, the E vs k is generally shown for a few important directions along the Brillouin zone (reciprocal unit lattice). Examples of band structure for silicon and GaAs are shown in Figure 1.4 [3]. It can be seen that silicon is an indirect bandgap semiconductor and GaAs is a direct bandgap semiconductor.

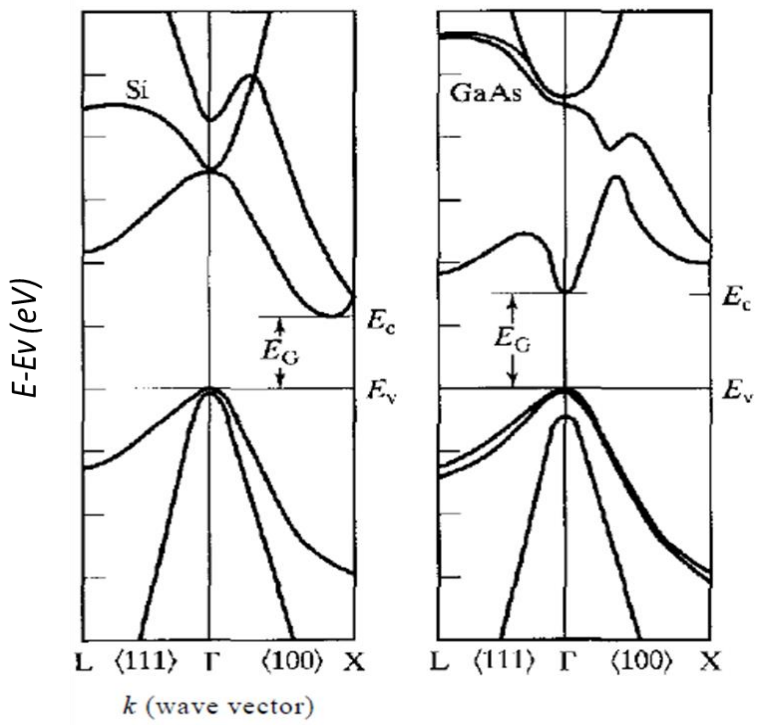

Figure 1.4: Bandstructure for silicon (left) and GaAs (right) in the Γ-X (<100>) and Γ-L (<111>) directions. Silicon has an indirect bandgap because the valence band maximum and conduction band minimum do not occur at the same wavevector [3].

1.2 Exotic properties of two-dimensional materials

The field of two-dimensional materials gained prominence in 2004 after mono-layer graphene was exfoliated using scotch tape by subsequent Nobel laureates Novoselov and Geim [4]. Graphene is a semi-metal, exhibiting no band-gap and a linear dispersion in energy around the Dirac point (point separating valence and conduction bands) as shown in Figure 1.5 [5].

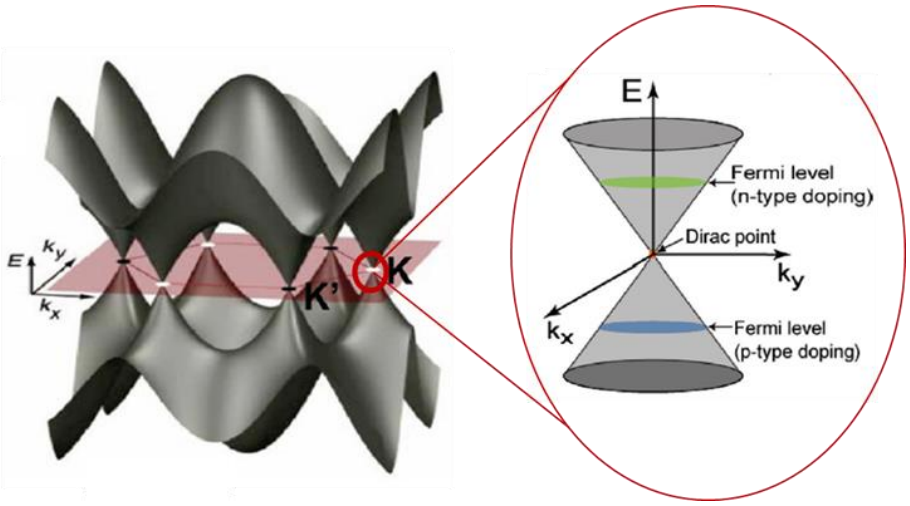

Figure 1.5: Band structure of graphene showing linear dispersion around the Dirac point that separates the valence and conduction bands (adopted from [5]).

Graphene possesses extraordinary properties such as ultrahigh thermal conductivity (1000-3000 W/m/K [6]), highest known electron mobility (μ = 200,000 $cm^2/V/s$ [7]), high mechanical strength [8] and a universal optical absorption [9] in the visible to infrared wavelengths. However, due to the lack of bandgap, graphene could not be successfully used in transistors and diodes which are at the heart of modern computers. Hence the search for other two-dimensional materials lead to the discovery of hundreds of interesting compounds, such as transition metal dichalcogenides (MoS_2, WS_2, $MoSe_2$), oxides, oxyhalides, etc. A list of 2D materials along with their properties is shown in the Figure 1.6 [10]. It can been seen that 2D materials of different classes possess very different and exotic properties which include superconductivity, giant magnetoresistance, topological insulation, and quantum spin hall effect to name a few. They can range from being an insulator to a metal and also show magnetic properties. All these qualities, along with their atomically thin cross-section, makes them suitable for nanotechnology applications, a field which by itself has spread into almost all branches of science and engineering.

Currently, most 2D materials are obtained by cleaving their corresponding bulk crystal with scotch tape and repeatedly exfoliating it to obtain thin flakes. This is possible because the layers in a 2D materials are weakly bonded by Van der Waals bonds. Exfoliation results in random distribution of thickness and does not allow precise placement of the desired flakes. However, several researchers are actively working towards the synthesis of different 2D materials from the bottom up, i.e. growing them layer by layer, an example of which is shown in Figure 1.7 [11], for

CVD growth of MoS_2 on h-BN. Growth of high quality 2D materials is crucial for commercialization of future technologies.

Table 1. A List of 2D vdW Materials with Their Composition and Representative Physical Properties

Component	Representative compounds			Insulator	Semiconductor	Metal	Magnetism	Superconductivity	Notice
1	Graphene					x		x	Dirac fermion
	Si, Ge, Sn				x				Unstable
	P				x				Oxidized in the ambient condition
2	Boride		MgB_2			x		x	
	Nitride		BN	x					
			Ca_2N			x			Electride
	Oxides	MO_3	MoO_3, WO_3, TaO_3		x				Strong correlation materials
	Chalcogenides	MCh	GaSe, InSe		x				
			FeSe			x	x	x	
		MCh_2	2H-MoS_2, 2H-NbS_2		x	x		x	
			1T-NbS_2, 1T-PtS_2		x	x		x	
			T_d-WTe_2			x			Giant magnetoresistance, Weyl semimetal
		MCh_3	$NbSe_3$, $ZrTe_3$			x		x	Quasi-one dimensional CDW
		$M2Ch_3$	Bi_2Te_3, Sb_2Te_3		x				Topological insulators
	Halides	MH	ZrBr		x				Quantum spin hall insulators
		MH_2	CdI_2, $CoCl_2$		x				
		MH_3	$CrCl_3$, $RuCl_3$		x		x		Spin chain
3	Oxyhalides	MOH	FeOCl		x		x		
	Nitrohalides	MNH	TiNCl, ZrNCl					x	Quantum spin hall insulators
	Phosphorous trichalcogenides	$MPCh_3$	$FePS_3$, $SnPS_3$		x		x		
	Sili-tritelerides	M(Si,Ge) Te_3	$CrSiTe_3$		x		x		

Figure 1.6: Table adopted from [10] showing different classes of 2D materials and their properties.

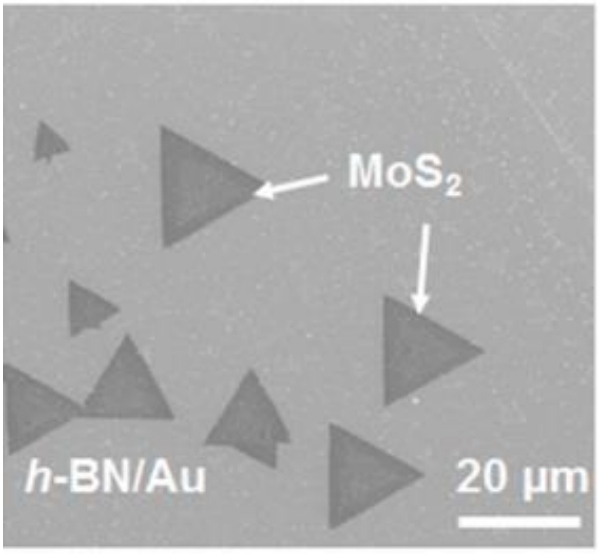

Figure 1.7: Growth of MoS_2 on h-BN [11]

Black phosphorus and tellurium are emerging 2D semiconductors which have been successfully tested as transistor and diode material [12,13]. Due to their direct low energy bandgap, they are also suitable for mid-infrared photodetection [14]. The properties of black phosphorus and tellurium will be elucidated in detail in section 1.3 and 1.4 and experiments will be presented in Chapter 2 and Chapter 3.

Topological two-dimensional materials form a new class of exciting materials that hold promise for applications such as quantum computing and spintronics. They behave as insulators in their bulk but are metallic on the surface. The origins of topological effect and recent discoveries on 3D topological insulators will be provided in section 1.5. Experiments on the topological insulator Bi_2Te_2Se will be presented in Chapter 4.

1.3 Structure and properties of black phosphorus

Black phosphorus can be obtained from white phosphorus by applying high pressure of around 1.2 GPa and moderate temperature of 200˚C. The popularly used methods are the Bridgeman method and the bismuth-flux method. Black phosphorus can also be obtained from red phosphorus by applying 3.8 GPa pressure and 270˚C temperature. Recently, low pressure synthesis of black phosphorus has also been achieved by using mineralizer as reaction promoters. The above mentioned methods are provided in an excellent review article by Liu et al [15]. Due to its

increasing use in research, highly pure black phosphorus is available for purchase from chemical manufactures such as SigmaAldrich and smart-elements. A picture of a commercially available ampoule is shown in Figure 1.8. In this thesis, thin flakes are obtained by cleaving the bulk crystal purchased commercially.

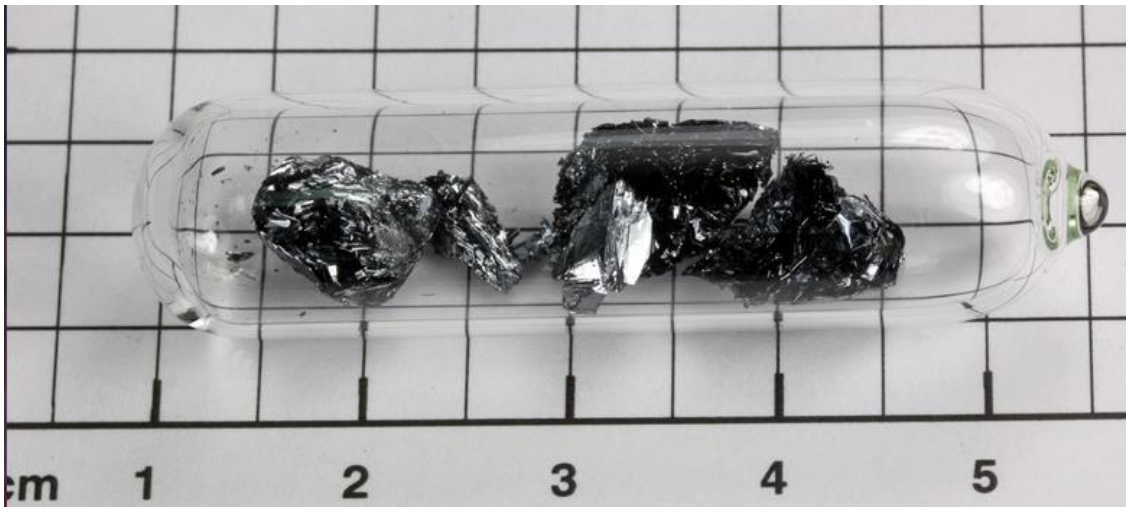

Figure 1.8: Commercially available ampoule of black phosphorus. Source: smart-elements.com

Being a two-dimensional material, black phosphorus has strong in-plane bonding and weak interlayer Van-der Waals bonding, which makes it possible to cleave a bulk crystal with dicing tape and obtain thin films. The arrangement of phosphorus atoms is shown in Figure 1.9 [12,16].

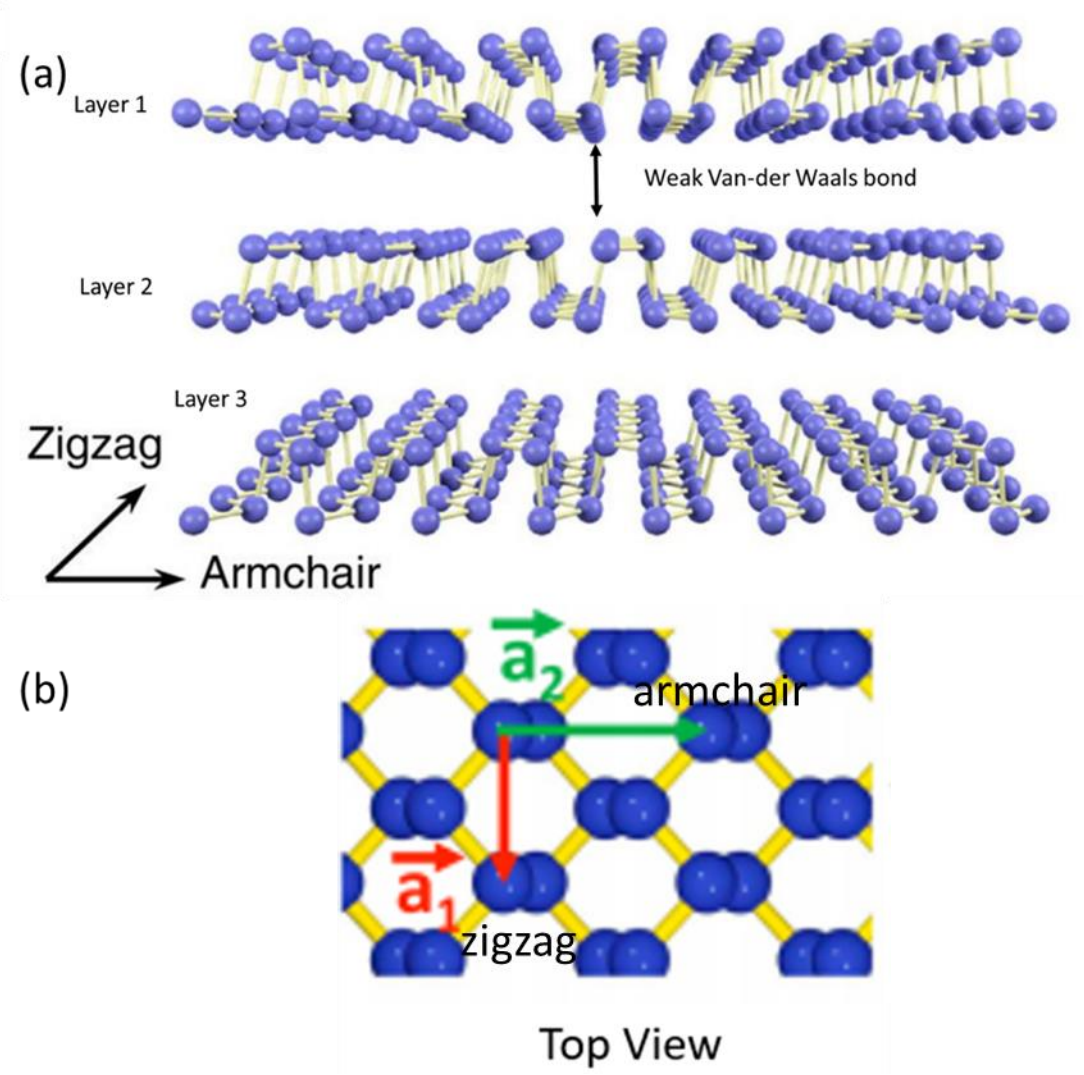

Figure 1.9: Arrangement of black phosphorus atoms in puckered honeycomb lattice structure. (a) shows side view with three layers [16] and (b) shows top view with lattice vectors a_1 and a_2 [12].

It can be seen that the structure is a puckered honey comb lattice. The armchair and zigzag directions are shown in Figure 1.9a. Black phosphorus displays anisotropic properties along the zigzag and armchair directions. The optical, thermal and electronic properties with direction are shown in Figure 1.10 [12,16,17].

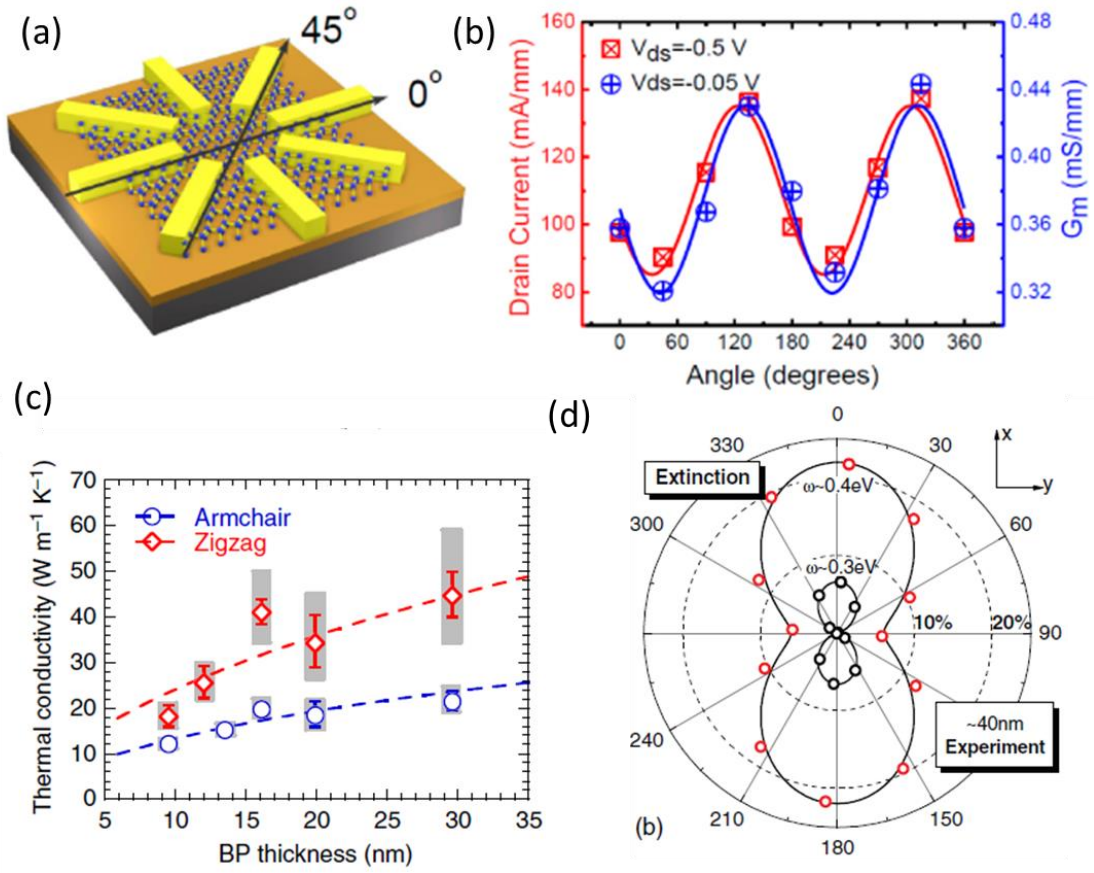

Figure 1.10: Anisotropic in-plane properties of black phosphorus: (a) fabricated device schematic for measuring anisotropic conductivity (b) drain current vs angle showing sinusoidal conductivity [12] (c) thermal conductivity vs thickness along the armchair and zigzag directions [16] (d) Optical extinction plotted with angle [17].

An almost 50% change in electrical and thermal conductivity along the zigzag and armchair directions was observed, with electrical conductivity being higher in the armchair direction (Figure 1.10b), and thermal conductivity being higher in the zigzag direction (Figure 1.10c). The optical absorption is more than two-times higher along the armchair direction (Figure 1.10d).

Black phosphorus is a direct bandgap semiconductor in the mono-layer, few-layer and in the bulk. The bandgap ranges from 0.3 eV in the bulk and upto 1.7 eV in the monolayer, as shown in Figure 1.11 [18].

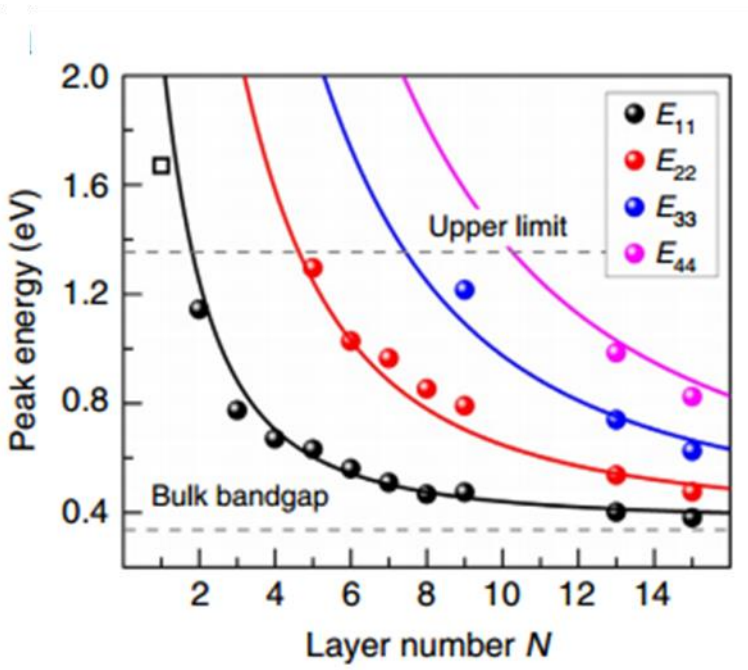

Figure 1.11: Layer dependent bandgap extracted from FTIR (Fourier transform infrared) measurements. E_{11} corresponds to the direct bandgap transition. E_{22}-E_{44} are higher energy transitions [18].

The band structure of bulk black phosphorus is shown in Figure 1.12 [19]. The Z-G direction corresponds to the armchair direction and Z-A(') corresponds to zigzag. From Figure 1.12, it can be seen that the armchair and zigzag directions possess a different effective mass, zigzag being almost one order of magnitude higher. This is one of the major reasons for anisotropic behavior, which will be further discussed in Chapter 2.

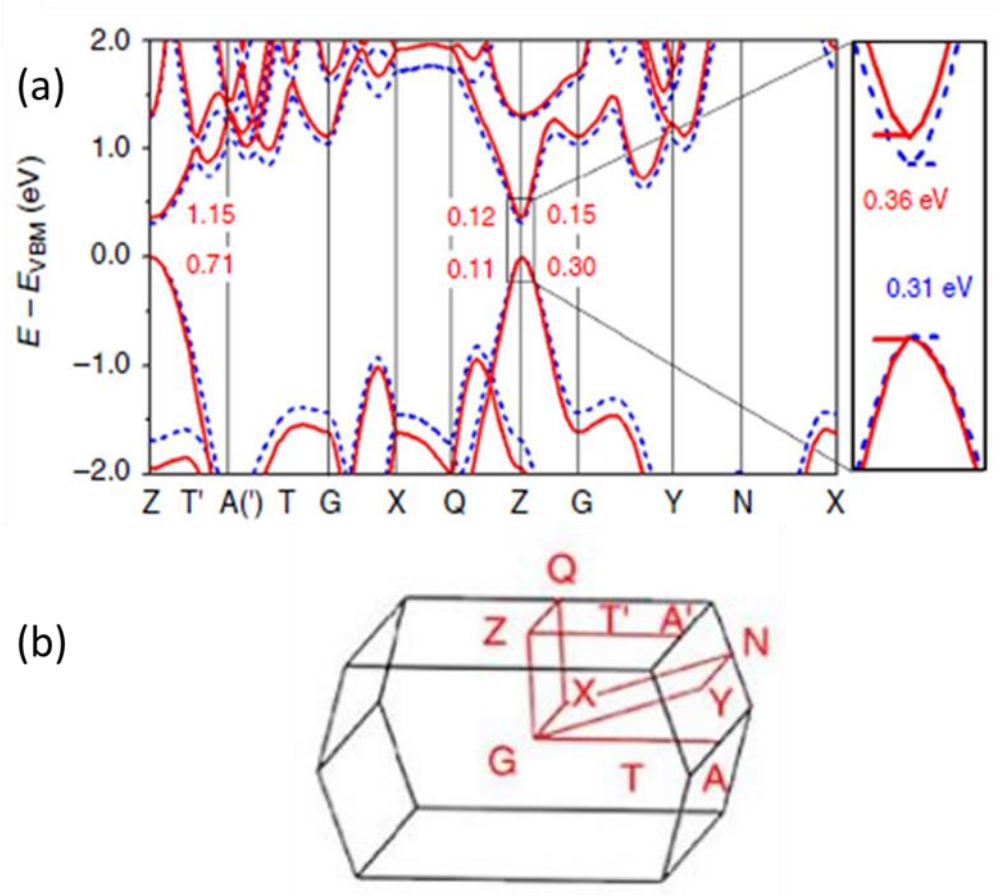

Figure 1.12: (a) Band structure of bulk black phosphorus (> 15 nm). The Z-G direction corresponds to the armchair direction and Z-A(‘) corresponds to zigzag. (b) Brillouin zone showing the points in reciprocal space [19].

With a direct bandgap ranging from mid-infrared in the bulk to visible wavelengths in the few layer regime, black phosphorus has potential in several applications. A comparison of black phosphorus with other two-dimensional materials is provided in Figure 1.13 [20]. Several technologically important applications such as thermal imaging, photovoltaics, telecom, thermoelectric and photodetection can be benefitted by the use of black phosphorus.

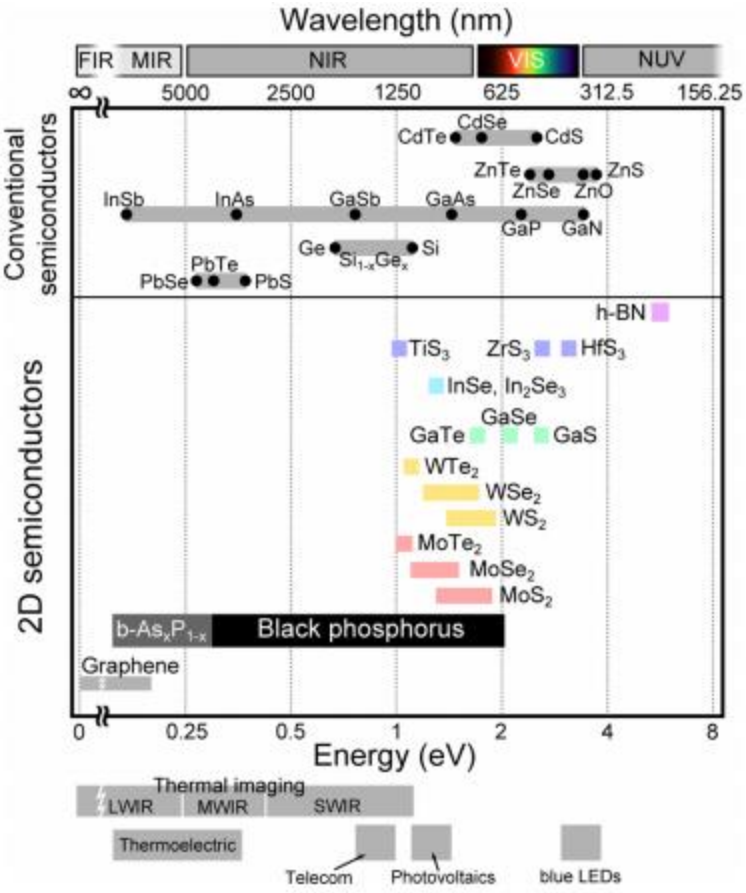

Figure 1.13: Comparison of black phosphorus with other two-dimensional semiconductors and conventional semiconductors [20].

1.4 Properties of tellurium

Tellurium flakes can be synthesized using a substrate free solution growth method [13]. Na_2TeO_3 and polyvinyl pyrrolidone (PVP) are put into double-distilled water at room temperature with magnetic stirring to form a homogeneous solution for 5 hours. The resulting solution is poured into a Teflon-lined steel autoclave, which is then filled with aqueous ammonia solution and hydrazine hydrate. The autoclave is sealed and maintained at 180^{o}C for 40 hours. Then the autoclave is cooled to room temperature. The resulting products are precipitated by centrifuge at 5000 rpm for 5 minutes and washed with distilled water and acetone. The suspended 2D Te flakes can be scooped out from the solution onto a substrate.

Tellurium has an anisotropic crystal structure and the arrangement of atoms is shown in Figure 1.14.

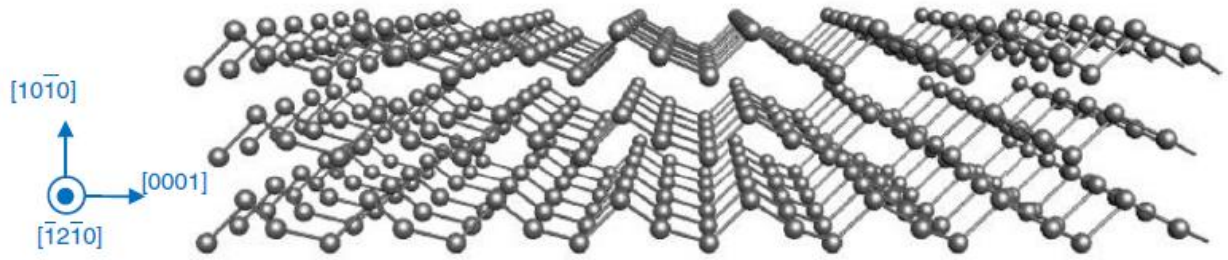

Figure 1.14: Layered atomic structure of tellurium showing in-plane anisotropy along the [0001] and [$\bar{1}$2$\bar{1}$0] directions [13].

Similar to black phosphorus, properties such as thermal conductivity and electrical conductivity are anisotropic, as shown in Figure 1.15.

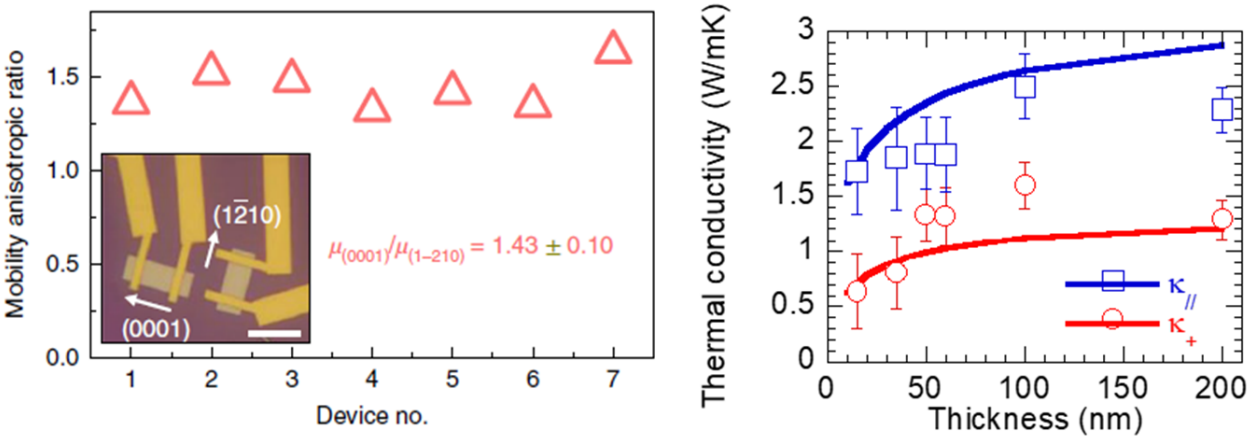

Figure 1.15: Anisotropic mobility ratio (left panel) obtained from devices fabricated along the [0001] and [$\bar{1}$2$\bar{1}$0] directions [13]. Anisotropic thermal conductivity (right panel), where $k_{||}$ is the [0001] direction and $k_{\perp}$ is the [$\bar{1}$2$\bar{1}$0] direction [21].

Unlike black phosphorus, bulk tellurium exhibits a direct bandgap along the [$\bar{1}$2$\bar{1}$0] and an indirect bandgap along the [0001] (c-axis) direction as evidenced by the absorption measurements near the band edge shown in Figure 1.16 [22].

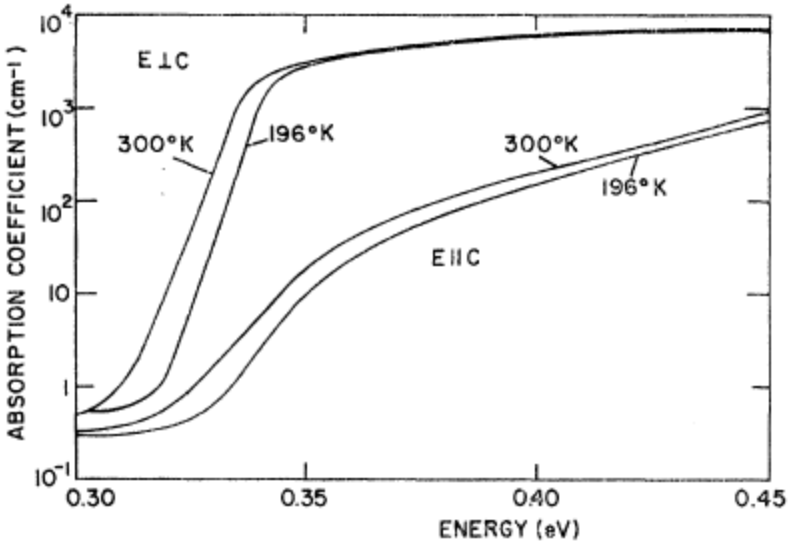

Figure 1.16: Absorption coefficient near the band edge of 0.35 eV. The sharp transition for light polarized perpendicular to the c-axis indicates a direct bandgap [22].

1.5 Introduction to topological insulators

The field of topology is derived from mathematics and has been very successfully applied to condensed matter physics by Nobel prize winners Kosterlitz, Haldane and Thouless [23]. Insulators, metals and semi-conductors were introduced in section 1.1. With the band structure perspective in mind, topological insulators are materials with an insulating bulk and conducting surface, i.e. there is a bandgap in the bulk of the material but a continuous set of energy states on the surface. The first topologically ordered state of matter was discovered in the quantum Hall state, that occurs at low temperature and when a strong magnetic field is applied to a planar electron gas (e.g. an interface sandwiched between two semiconductors), as shown in Figure 1.17.

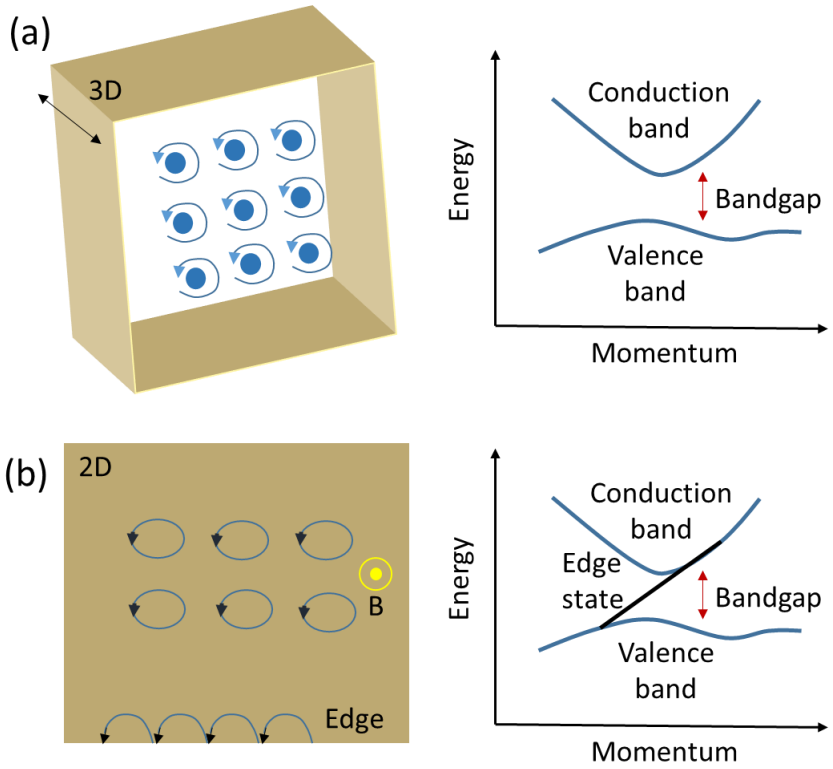

Figure 1.17: (a) Usual insulator possessing a bandgap because the energy of the electron orbits are quantized. (b) quantum Hall state for 2D gas with application of a strong magnetic field that allows continuous energy states to exist at the edge due to the hopping of electron orbit.

The discovery of quantum Hall state prompted the investigation into material systems that could display this kind of surface/edge conduction without the need for an externally applied magnetic field. It was found that strong spin-orbit coupling could essentially play the role of magnetic field and hence produce a similar surface state, but with an added degree of spin [24]. The experimental realization of the 2D quantum spin Hall effect came in 2007, in a quantum-well structure made by sandwiching a thin layer of mercury telluride (HgTe) between layers of mercury cadmium telluride (HgxCd1–xTe) [25]. A depiction of the quantum spin Hall state is shown in Figure 1.18.

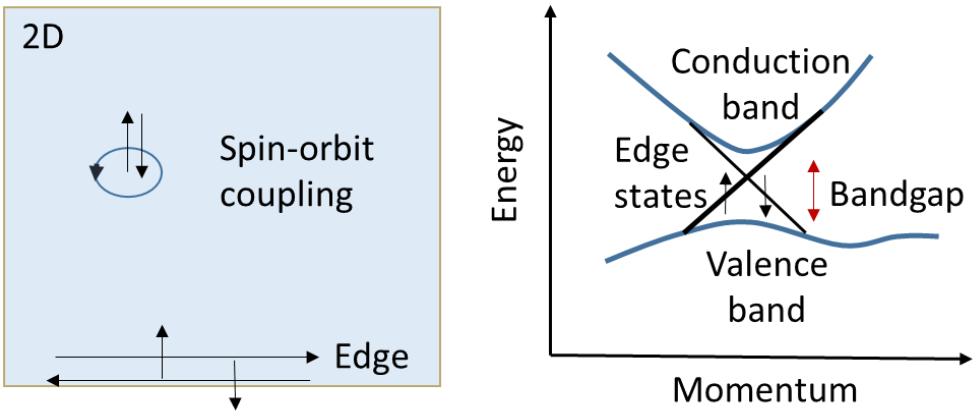

Figure 1.18: Quantum spin Hall state. The edge has two continuous bands instead on one, as in the quantum Hall state (Figure 1.17b). The two bands arise due to the two spins (up and down) and each band carries only electrons of one spin type.

Subsequently, 3D topological insulators were discovered, where the spin-orbit coupling leads to the existence of spin-momentum locked surface states on the entire surface of the 3D bulk material. Angle resolved photoemission spectroscopy (ARPES) has been widely used to study 3D topological insulators and Figure 1.19 [26] shows the ARPES data on Bi_2Se_3.

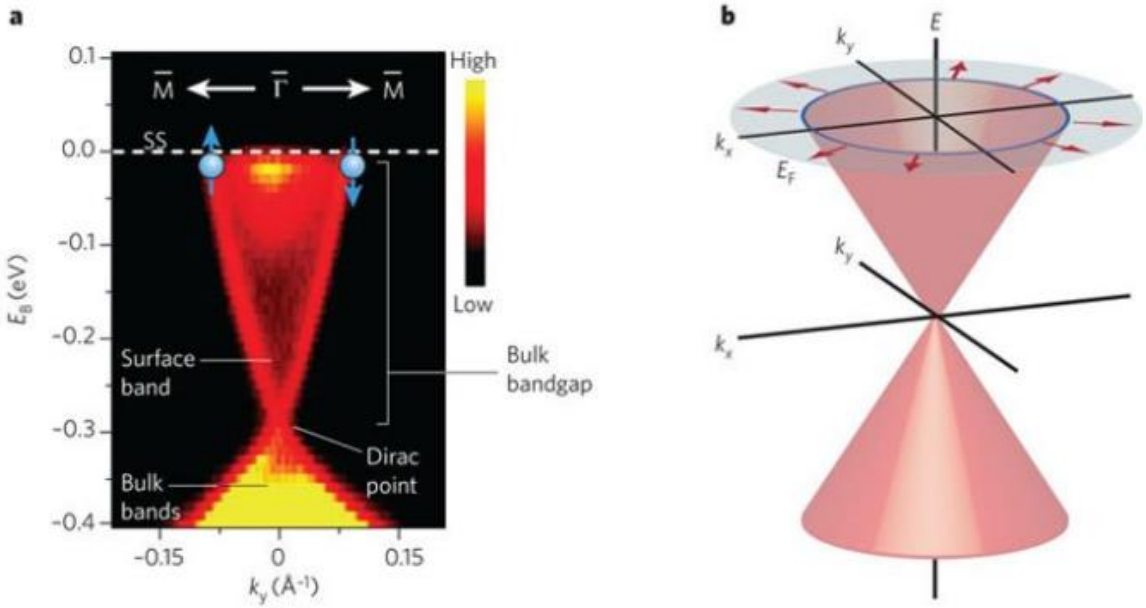

Figure 1.19: Surface states in 3D topological insulator Bi_2Se_3 where (a) is the ARPES data in the Γ-M direction clearly revealing the surface band and (b) shows the energy dispersion along both directions. The spin (represented by arrows) is always perpendicular to the momentum [26].

Fundamentally, surface states arise in only select materials because of a topological invariant. This concept is derived from the branch of topology in mathematics. A common example is the invariant for closed surfaces. If we consider a tea cup and a donut, we find that both have one hole in their structure, whereas a sphere has no holes. The tea cup can be smoothly reshaped and made into the donut shape without having to cut or paste, as shown in Figure 1.20 [27]. Hence both surfaces are classified as having the integer invariance of 1, i.e. the number of holes.

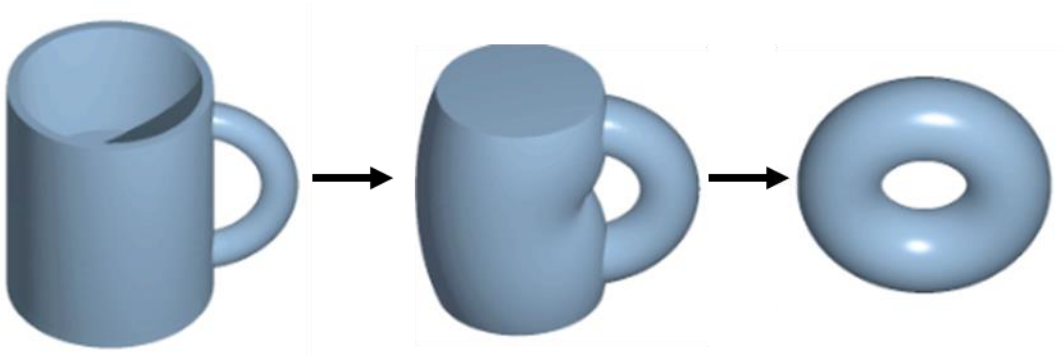

Figure 1.20: Closed surfaces with one hole can be deformed smoothly from a tea cup to a donut shape. The number of holes in a closed surface is its topological invariant [27].

This concept is extended to the energy bands in the reciprocal space. Consider a simple case for 1D system, where the reciprocal space spans from $-\pi/a$ to $+\pi/a$ as shown in Figure 1.21:

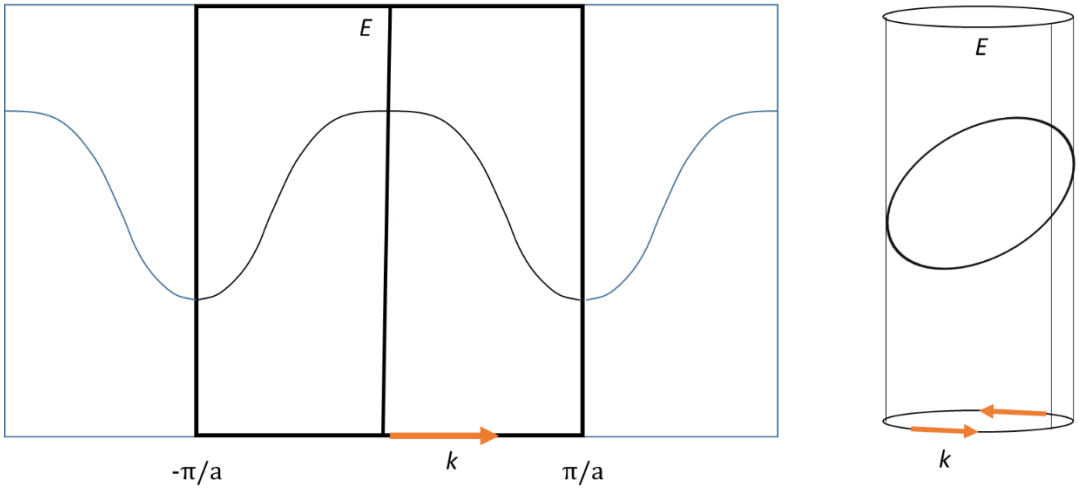

Figure 1.21: Energy diagram of a simple 1D solid showing periodic reciprocal space (left) and wrapping around of the reciprocal space on itself (right).

The Berry phase ϕ, for Bloch bands is defined as:

$$\phi = \oint i\langle u_{nk} | \partial_k u_{nk} \rangle dk \quad (1\text{-}4)$$

Where u_{nk} is as defined in Eq. (1-2). The integrand is known as the Berry connection (The integral can be converted to an area integral using the Stokes theorem, in which case the integrand is known as the Berry curvature). In Equation 1-4, the integration is done from $-\pi/a$ to $+\pi/a$ and results in an integer multiple of 2π. This is known as the Chern theorem and the resultant integer is the Chern number, which is the topological invariant for the bands. For simple one-dimensional bands as shown in Figure 1.21, a Su-Schrieffer-Heeger (SSH) model is typically used to describe the topological properties. Detailed analysis can be found in standard treatments of the subject [28]. The particular band structure shown in Figure 1.21 is for electrons in a simple one-dimensional periodic potential and does not possess any topological properties. Chern number calculations for a widely used 3D topological insulator, Bi_2Se_3, can be found in literature [29].

For Chern insulators (e.g. quantum hall state), the Chern number is > 0. C = 0 corresponds to topologically trivial state such as vacuum and whenever the Chern number for the energy bands in a semiconductor is greater than 0, a continuous energy band is formed at the surface to allow transition of the topology. The offshoot of this is that the surface states are protected from disorder and impurities [28]. For 3D topological insulators, the Z_2 invariant is the topological invariant, which is also related to the Berry curvature. Z = 0 corresponds to topologically trivial state and Z = 1 corresponds to topological insulator state. Detailed quantum mechanical calculations of the integration of Berry curvature are available in the article by Hasan and Kane [30].

Surface states in 3D topological insulators have very useful properties such as spin-momentum locking, backscattering protection from impurities and defects and high mobility, which makes them suitable for the growing field of spintronics. When light excites electrons in a material, energy and momentum must be conserved. Light incident at an oblique incidence with circular polarization carries in-plane angular momentum. Since the surface state electrons are confined on the top-surface, their spins lie on that surface. Light can therefore preferentially excite electrons in either of the two surface bands depending on its helicity. This simple conservation principle has been exploited to observe helicity dependent photocurrents in Bi_2Se_3 as shown in Figure 1.22 [31]. When the in-plane angular momentum of light is parallel to the contacts, the spins parallel to the contact are excited, leaving behind the spins that are anti-parallel as seen in Figure 1.22a. Due to the spin-momentum locking, the electrons move towards the contacts and a

helicity dependent current is generated. Figure 1.22b,c show that the helicity dependent current component vanishes if the spins perpendicular to the contacts are excited or are isotropically excited.

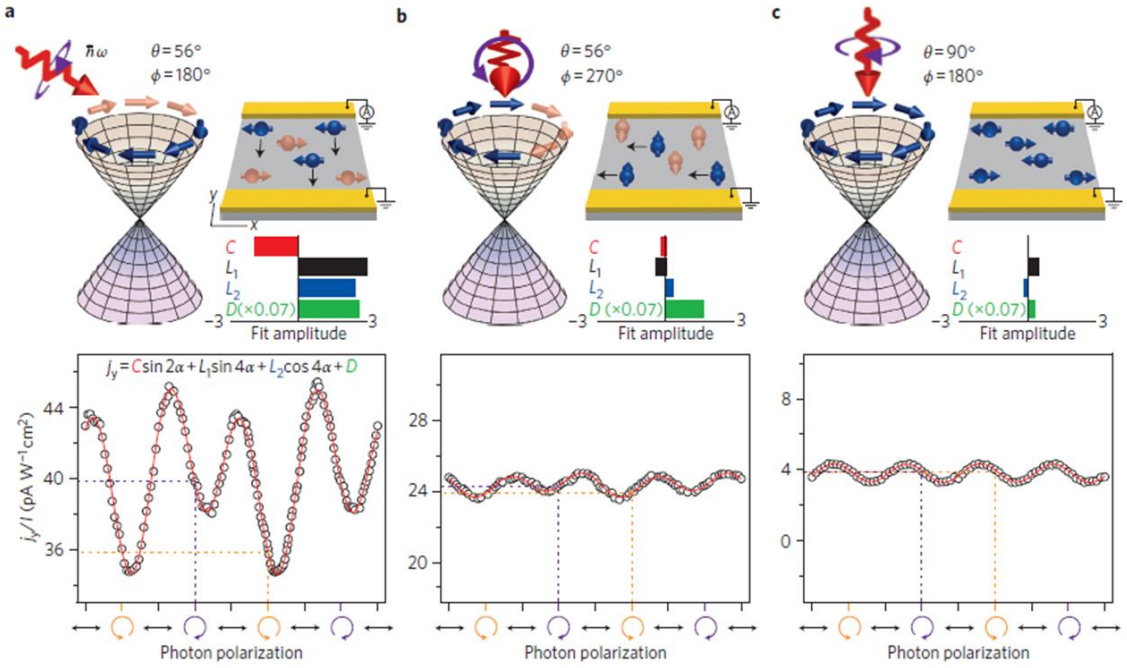

Figure 1.22: Light helicity dependent photocurrent in Bi_2Se_3. Panel (a) shows in-plane angular momentum of light is parallel to the contacts, leading to clear helicity dependence, (b) light has in-plane angular momentum perpendicular to the contacts and (c) angular momentum is out of plane leading to isotropic excitation of the Dirac cone [31].

The selective excitation of the surface states have also been observed in ARPES studies on Bi_2Te_3 with oblique, circularly polarized light as shown in Figure 1.23 [32].

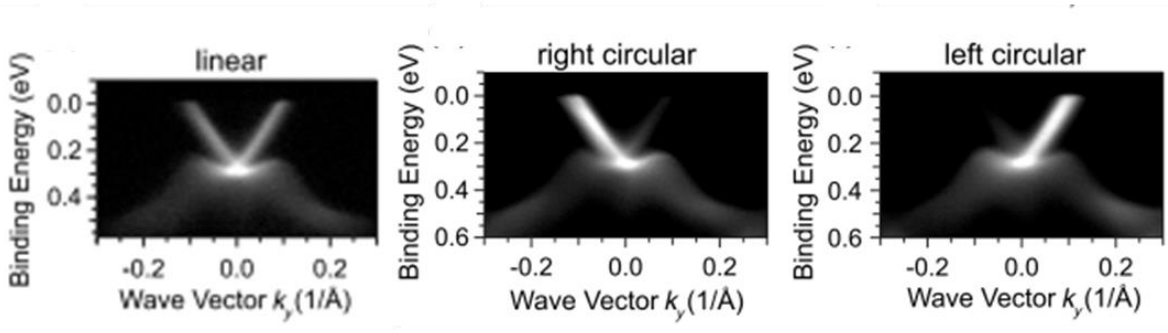

Figure 1.23: Selective excitation of surface state branches with circularly polarized light in Bi_2Te_3 [32].

The spin momentum locking feature of topological insulators can be favorably used for applications such as spintronics, where the electron's spin, instead of its charge is used to perform logic operations [33]. Optical means of controlling spin currents are attractive for a photonic approach to spin devices. Compared to widely studied Bi_2Se_3 and Bi_2Te_3, topological insulators Bi_2Te_2Se (BTS) and $BiSbTeSe_2$ have better bulk insulating properties due to the Fermi-level being situated near the middle of the bandgap [34,35]. Hence, we chose Bi_2Te_2Se for our study. The band structure of Bi_2Te_2Se is shown around the Dirac point in Figure 1.24 [35]. The acceptor states near the valence band makes the bulk of the material p-type. The bandgap is about 0.3 eV.

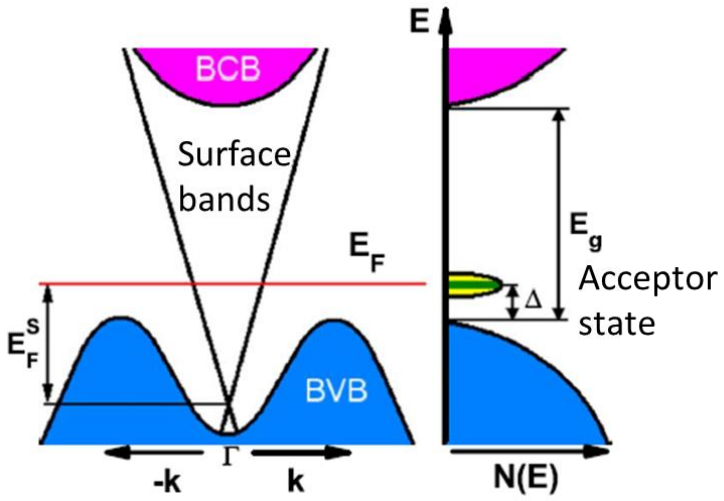

Figure 1.24: Band structure of Bi_2Te_2Se around the Dirac point. The acceptor states near the valence band makes the bulk of the material p-type [35].

Recent electrical and thermal transport measurements have shown a striking contribution of the surface states in Bi_2Te_2Se as shown in Figure 1.25 [36]. There is a rapid increase in thermal and electrical conductivity for thin films, pointing to the metallic nature of the surface states.

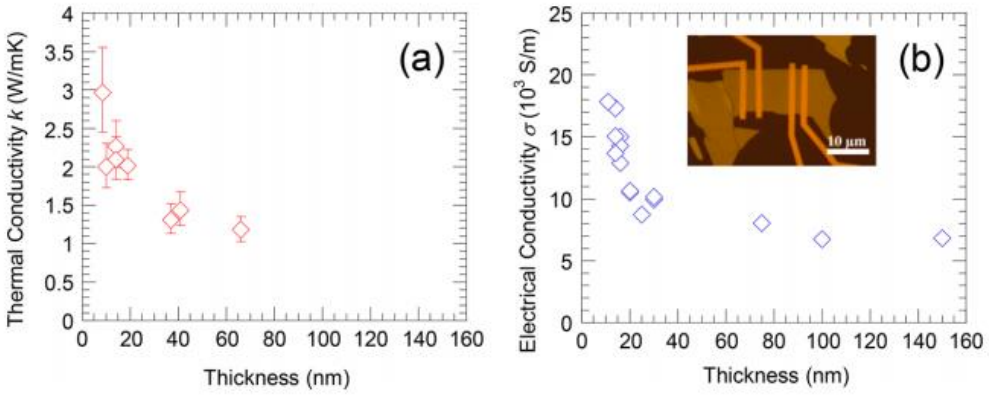

Figure 1.25: (a) Thermal conductivity vs thickness (b) Electrical conductivity vs thickness [36].

1.6 Femtosecond pump-probe technique

Pump and probe technique relies on the use of ultrashort laser pulses. Typically, a Ti-Sapphire laser generates sub 100 fs pulses centered at 800 nm wavelength and a bandwidth of 20-30 nm. The output beam is split into a pump arm and a probe arm, one of which is sent though a translation stage before combining again and reaching the sample. The pump is typically one to two orders of magnitude larger than the probe, and is also slightly larger at the focal point on the sample to ensure uniform illumination in the probe region. The probe/pump may or may not be sent through an optical parametric amplifier system to convert the wavelength, which can range from ultraviolet to mid infrared. The pump excites carriers in the material, which then relax to their initial state by losing energy to the lattice. During the time when the electrons are perturbed from their ground state, the probe's reflection/transmission changes from the unperturbed condition. This change is recorded by photodetectors and forms the signal that is analyzed to extract useful information such as electron-phonon coupling constants and electron recombination mechanisms.

1.6.1 Description of Coherent laser system

In this work, a commercial amplified laser system (Coherent Inc) is used to perform the experiments. Figure 1.26 shows the picture of the laser system. The seed laser is a Nd:YAG pumped Ti:Sapphire laser that produces modelocked train of femtosecond pulses at 78 MHz repetition rate. The cavity has a slit and prism pair which can be adjusted to tune the center wavelength and bandwidth of the output. The system is typically run at 805 nm center wavelength

and 60 nm bandwidth, producing about 400 mW of optical power. The Ti-Sapphire crystal must be periodically cleaned with solvent such as acetone to ensure optimum performance.

The seed output then enters the amplifier. The amplifier is divided into the stretcher, cavity and compressor portions. The seed first enters the stretcher, where the femtosecond duration pulse is stretched to nanosecond by using a grating and retroreflectors. This step is important because otherwise, the Ti:Sapphire crystal in the amplifier cavity can be damaged by the intensities that would be created by the femtosecond pulses. The nanosecond pulse ensures amplification without the possibility of damage to the cavity components. This technique is known as 'chirped pulse amplification'. The stretched pulse then enters the cavity through a pockel cell, which is equivalent to an electronically operated switch for light. It works on the principle of electric-field induced bi-refringence. Only one out of 15600 pulses is selected to enter into the cavity for amplification, making the output from the cavity to be at 5 KHz. The Ti:Sapphire crystal is pumped by a Q-switched Nd:YAG laser to achieve the required amplification. The seed undergoes about 4-5 passes inside the cavity before it is ejected by another pockel cell into a single pass amplification stage. At this stage the seed gets amplified to about 5 W. After passing through the single pass amplification stage, the seed emerges at about 11 W. Finally the beam is sent through the compressor portion, where the pulses are again compressed to femtosecond duration by grating and retroreflector. The final output power is close to 10 W and 40 fs.

Just at the exit of the amplifier, the laser beam is split in a 90:10 ratio and the larger part is send into an optical parametric amplifier (OPA). The OPA has a two (three) stage conversion process for obtaining 1200-2500 nm (2500-14,000 nm) light. In the first stage a portion of the laser beam is sent through to generate white light continuum and a specific wavelength is selected, which is then amplified in the second stage. The conversion process creates three beams, namely the signal (1150-1550 nm), idler (1550-2400 nm) and the 800 nm itself, which is dumped. A third stage can be used which further creates a difference frequency of the signal and idler in order to obtain low frequencies. Hence, the OPA can be continuous tuned from 1.2 μm to 14 μm wavelength.

The output from the OPA is sent into a custom built, nitrogen purged experiment chamber as shown in Figure 1.27 . The inset shows the chamber from outside. Nitrogen purging prevents infrared absorption due to oxygen and CO_2. A pair of reflective objectives is used to allow chromatic aberration free focusing of pump and probe beams to a 15 μm spot size. The experiment

can be performed with 800 nm pump and infrared probe (counter-propagating or co-propagating) or with infrared pump and probe (counter-propagating). This allows transmission and reflection mode operation.

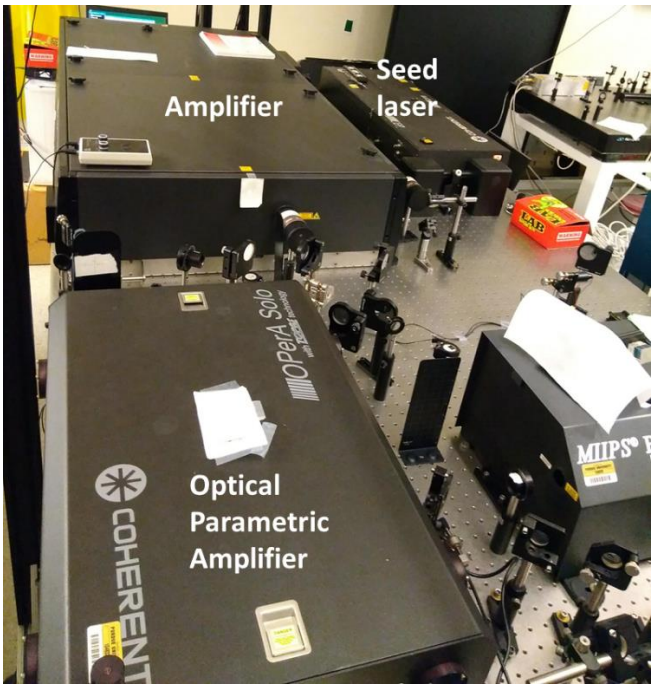

Figure 1.26: Components of Coherent commercial laser system

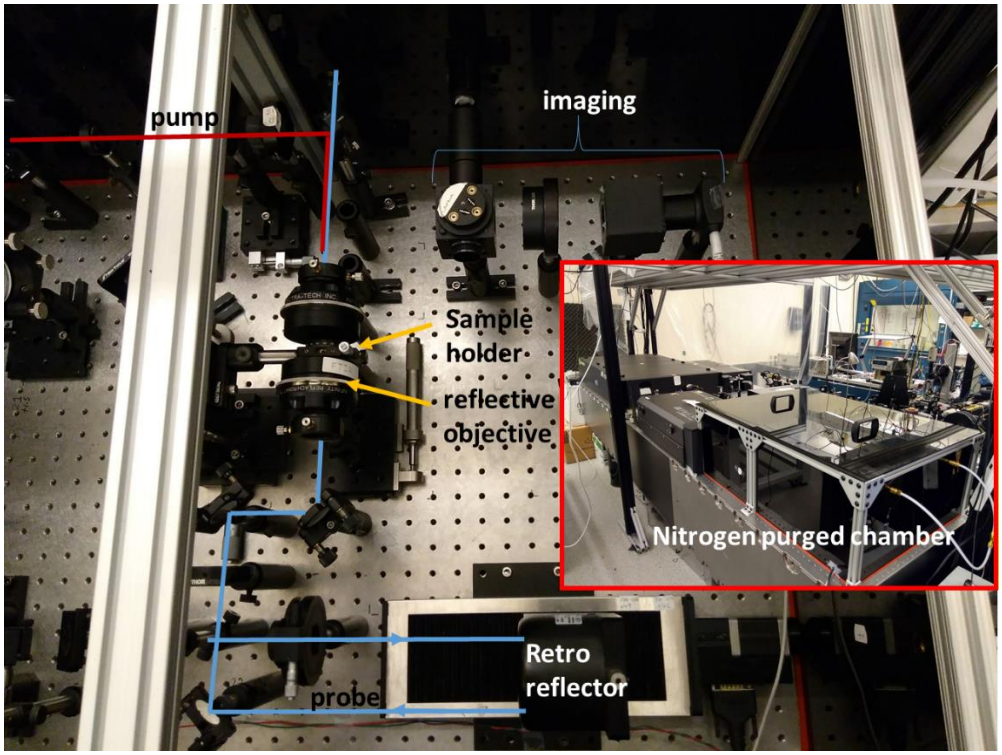

Figure 1.27: Pump-probe experiment chamber with nitrogen purging. Reflective objectives are used to avoid chromatic aberration when using infrared wavelengths. Inset shows the chamber from outside.

The specifics of a particular experiment (pump/probe wavelengths) will be presented in the corresponding chapter.

1.6.2 Detection scheme with lock-in amplifier

The train of pump pulses at 5 KHz is chopped at 500 Hz frequency using an optical chopper. This leads to the detector response as shown in Figure 1.28. Modulating at 500 Hz means that 10 pump pulses are blocked and unblocked as the chopper rotates. The reflected/transmitted probe pulse undergoes a modulation at the same frequency. The detector detects only the probe pulses (the pump is rejected by filters) and hence its response is also modulated at 500 Hz. The 5 KHz background is rejected by the lock-in amplifier and only the change to the reflected probe is detected at 500 Hz. This scheme provides excellent signal to noise ratio and changes in reflectivity down to 10^{-4} – 10^{-5} can be detected. A difference detector may be used further improve signal to noise ratio.

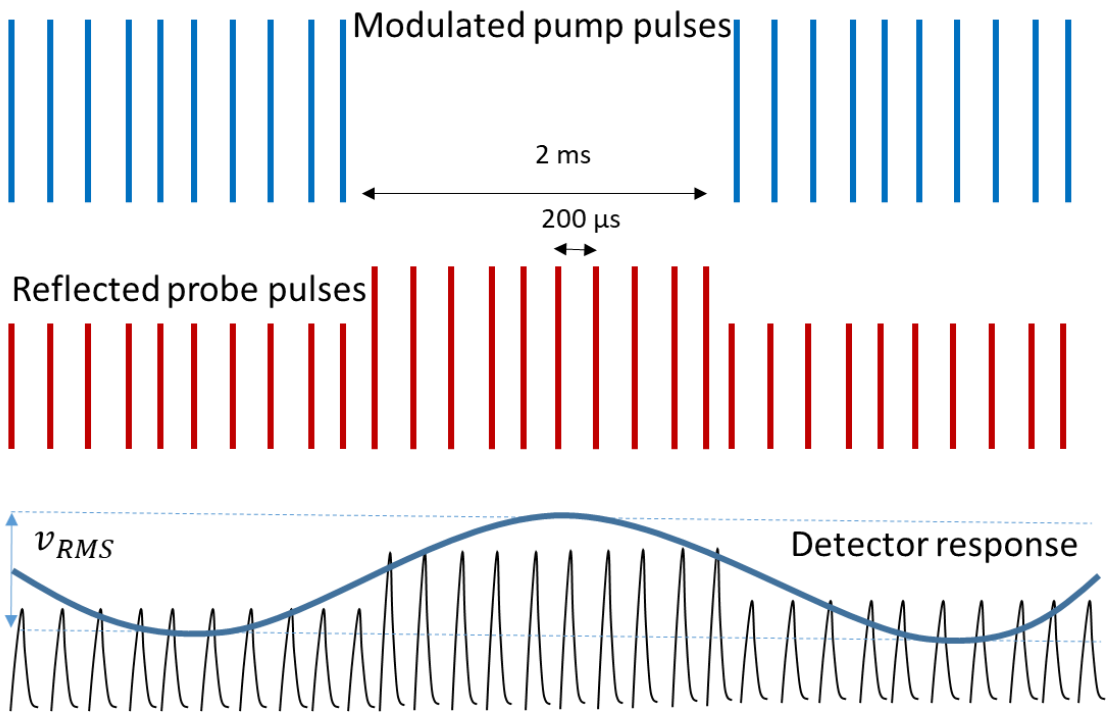

Figure 1.28: Lock-in detection scheme showing pump and probe pulse trains and detector response. The lock-in amplifier locked to pump modulation frequency, detects only the change in probe amplitude depicted by the sinusoidal curve.

Care must be taken to correctly set the phase of the lock-in amplifier since the final sign of the acquired data depends upon the phase. An ideal way is to allow some of the 500 Hz pump beam to leak into the detector while blocking the probe beam and then applying the auto-phase setting in the lock-in amplifier. This sets the de-modulating sinusoidal to have its peak value when the pump is incident on the detectors. Hence, the lock-in detects the change in probe intensity during the time the pump is unblocked and leads to correct sign of the signals.

1.6.3 Examples of femtosecond pump-probe experiments from literature

In this section, results on a few commonly studied materials in literature will be presented. In order to understand the features in the data for the materials of interest, i.e. black phosphorus, tellurium and topological insulators, a closer examination of results for metals, direct and indirect band gap semiconductors is useful. Comparison with metallic graphene and semiconducting MoS_2 is also instructive.

Figure 1.29 [37,38] shows the carrier dynamics on a picosecond time scale for 2D material graphene and compares it with thin film gold. It can be seen that both materials relax within about 5 ps. Hence we would expect the relaxation mechanisms in both materials to be similar. Electron-phonon coupling is the dominant mechanism for relaxation since there is no bandgap in both materials and the electrons can continuously slide down in energy by emitting either optical or acoustic phonons (gold does not have optical phonons, but graphene does). A schematic of the relaxation process is shown in Figure 1.30 [37,38]. Electrons in both graphene and gold undergo a rapid non-thermalized state after laser excitation and then thermalize around the Dirac point (Fermi-level in gold), after which they undergo further relaxation. Usually, a temperature can be ascribed to the hot electron population, which arises from the Fermi-Dirac distribution. The relaxation process can be thought of as exchange of heat between electrons and phonons and hence a transient temperature evolution of both systems. The efficiency of this transfer is captured by the electron-phonon coupling constant [38].

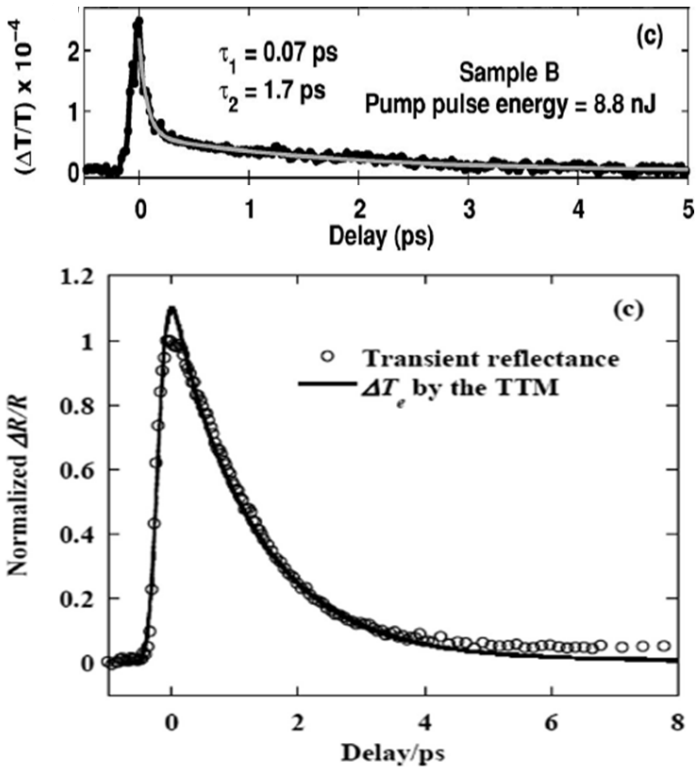

Figure 1.29: Transient carrier dynamics in graphene (top, [37]) and gold (bottom, [38]) . TTM fitting stands for two-temperature model fitting, which is used to describe the relaxation process by considering heat transfer between electrons and lattice.

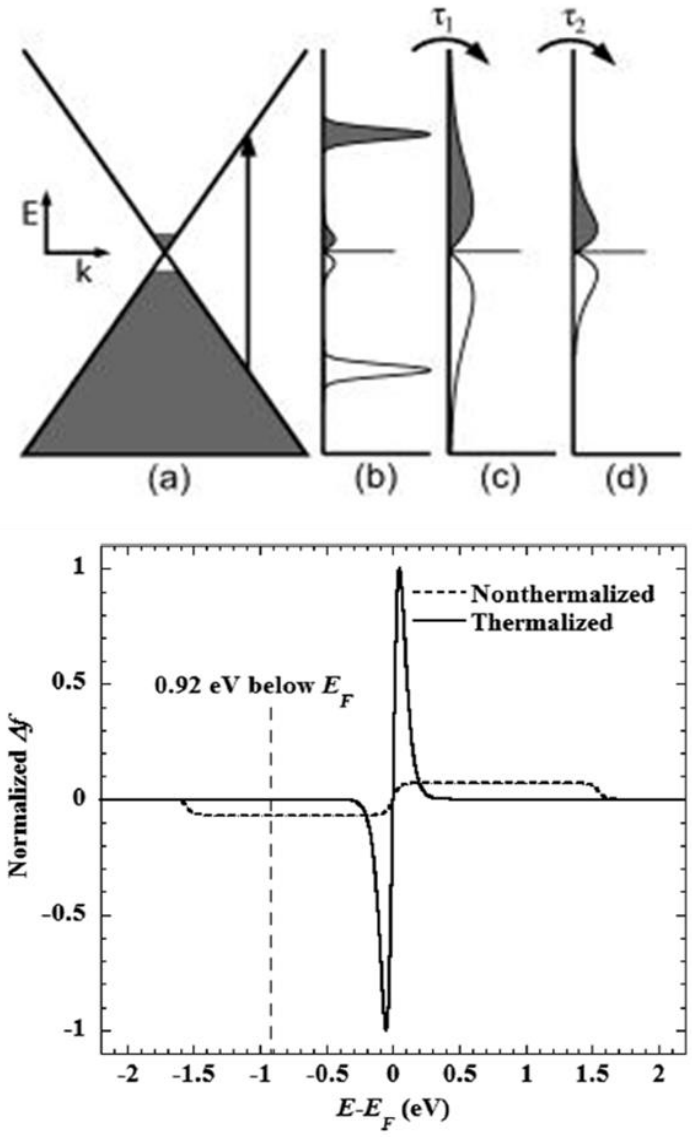

Figure 1.30: Process of relaxation via electron thermalization and electron phonon coupling in graphene (top, [37]) and gold (bottom, [38]). The electrons thermalize around the Fermi-level (Dirac point in graphene).

We next look at the dynamics in 2D material black phosphorus (800 nm pump and near bandgap 4000 nm probe) and compare it with bulk semiconductor GaAs (800 nm pump and near bandgap 860 nm probe), as shown in Figure 1.31. Both black phosphorus and GaAs are direct band gap semiconductors. The relaxation dynamics are similar and in the few 10s to 100 ps range. Similar to metals, excited electrons in semiconductors also undergo thermalization and phonon emission in the first few picoseconds but subsequently the carriers (electrons and holes) accumulate at the band edges (conduction and valence band edge). They cannot further relax

without pathways that allow them to cross the bandgap, which are known as recombination mechanisms. Direct bandgap semiconductors can emit photons and undergo radiative recombination. The carriers can also hop down through defect states present in the bandgap, usually requiring phonon assistance, known as Shockley-Read-Hall recombination. The relaxation processes are depicted in Figure 1.32.

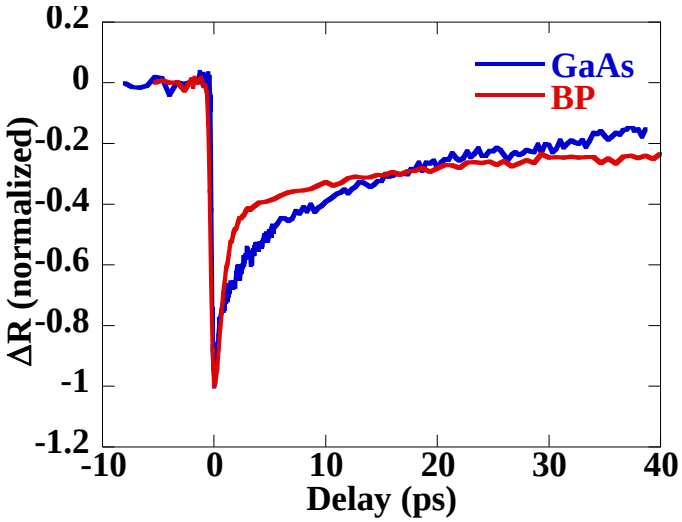

Figure 1.31: Carrier dynamics in direct bandgap 2D material black phosphorus and bulk semiconductor GaAs.

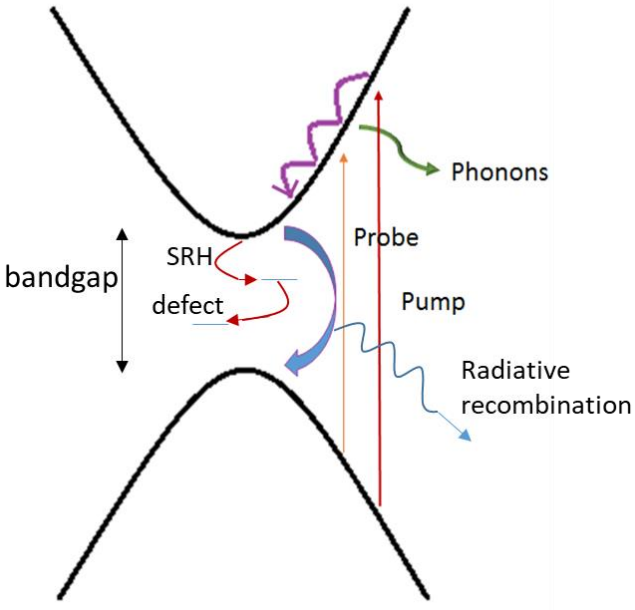

Figure 1.32: Excitation and relaxation processes in direct-bandgap semiconductors.

Lastly we look at the relaxation dynamics of 2D material MoS_2 (thin-film) and compare it with silicon, both of which are indirect bandgap semiconductors. From Figure 1.33 [39], we see that MoS_2 and silicon have relaxation timescales of 100s of ps, pointing to the similar relaxation mechanisms. In an indirect bandgap semiconductor, the band edges are at different locations in the k-space, and hence recombination is slower than in direct bandgap semiconductors because of the requirement of phonon and defect assisted pathway. The radiative pathway is not so effective because direct transition from conduction band edge to valence band edge is prohibited by momentum conservation.

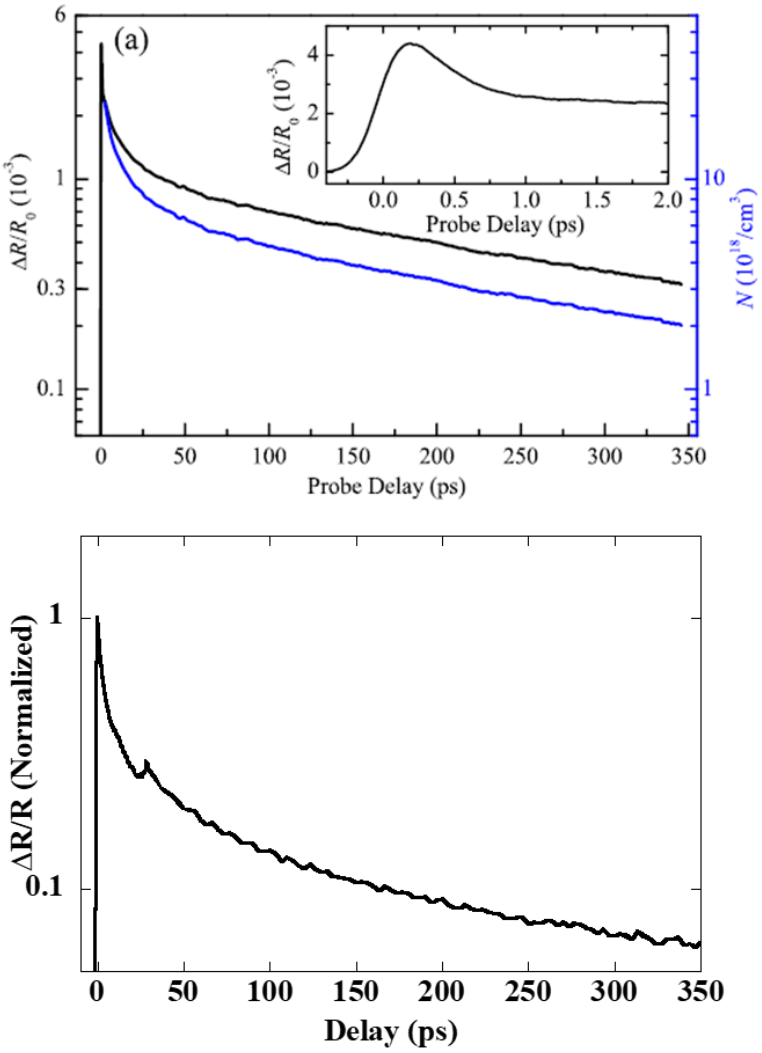

Figure 1.33: Carrier dynamics in MoS_2 (top, [39]) and silicon (bottom), showing similar timescales for relaxation.

The excitation and relaxation process is shown in Figure 1.34 [39], where the generated electrons and holes are separated in reciprocal space after thermalization and hence cannot radiatively recombine.

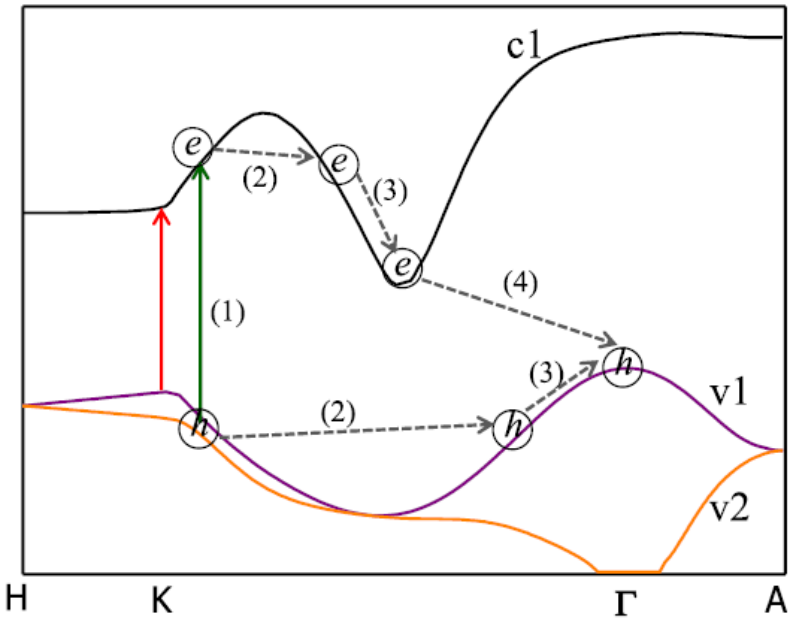

Figure 1.34: Excitation and relaxation in indirect bandgap semiconductor MoS_2 [39].

1.7 Outline of the report

In this work, 2D materials black phosphorus, tellurium and Bi_2Te_2Se have been studied by optical pump-probe spectroscopy to obtain a deeper understanding of the carrier and spin dynamics. The obtained results provide detailed information about electron-phonon interactions, recombination dynamics and carrier diffusion. The spin-lifetimes in Bi_2Te_2Se were also obtained and the materials shows viability in spintronic applications.

Chapter 2 discusses carrier dynamics in black phosphorus, for a 65 nm flake pumped with 800 nm light and probed with varying wavelengths starting from 1600 nm upto 5,000 nm. This covers the energy states that are far from the band edge all the way upto and below the band gap. The importance of selecting the right probing wavelengths will be discussed along with the obtained carrier-phonon and recombination lifetimes for near band gap probing.

Chapter 3 looks at thickness dependent relaxation dynamics in solution grown tellurium flakes with thickness in the 12 to 160 nm range. A near band edge probe is utilized and the obtained

data is modeled using a diffusion recombination equation. Radiative recombination and surface recombination emerge as the dominant mechanisms. A scattering model is used to describe the field-effect mobility obtained in literature.

Chapter 4 will present the study on 3D topological insulator Bi_2Te_2Se. The study was performed on thin flakes ranging from 14 to 75 nm and the corresponding charge and spin dynamics was probed. The effects of flake thickness, which manifests itself as varying Fermi-level will be discussed along with effects of pumping with different wavelengths. From the obtained spin relaxation, estimates of the spin diffusion lengths can be obtained, which is important for spintronics applications. Furthermore, coherent phonon generation will also be discussed.

Chapter 5 explores studies on optically induced spin transfer. Optically excited spins in TIs can be transferred to ferromagnets in close proximity, eventually leading to the flipping of the magnet for strong light fields. A magneto-optic Kerr effect system is built to monitor the magnetization state of the ferromagnet. Hence, an all-optical switching and detection scheme is used. Preliminary results have been obtained. This chapter also presents spatially resolved pump-probe studies to monitor the carrier diffusion in a variety of materials. For example, an attempt to distinguish the surface and bulk state diffusion properties of TIs is attempted. Thin flakes were back gated to manipulate the Fermi-level and increase or decrease the surface state contribution. Unconventional effects were observed.

2. ULTRAFAST CARRIER DYNAMICS OF THIN FILM BLACK PHOSPHORUS

This chapter has been partially reproduced from a previous publication*: Iyer, V.; Ye, P.; Xu, X. Mid-Infrared Ultrafast Carrier Dynamics in Thin Film Black Phosphorus. 2D Mater.* ***2017****, 4 (2), 021032.*

Since the last decade there has been an increasing interest in the study of 2D materials, especially graphene and transition metal dichalcogenides (TMDC) for fabricating many electronic and optoelectronic devices [40–44]. Black phosphorus has emerged as a recent material in this field and has shown promises with its direct bandgap, anisotropic electronic, optical, and thermal properties, and good device performance [12,16,17,19,20,45]. Black phosphorus has a direct bandgap in the bulk of around 0.35 eV and can become as large as 1.5 eV in the monolayer form according to first principles calculations, photoluminescence studies, and electrical measurements [12,19,46–48]. The direct bandgap is attractive for use in electronic devices such as solar cells [49,50] and photodetectors [51–53]. Black phosphorus has also been successfully tested as a transistor channel material [54,55]. Given the vast interest in black phosphorus, it is important to investigate its properties at a fundamental level. Ultrafast optical spectroscopy is very useful in understanding carrier scattering, relaxation, and recombination processes. Many ultrafast studies have been carried out on graphene [37,56–59] and TMDC such as MoS_2 [60–62]. There have also been a few ultrafast optical studies on black phosphorus which have brought out the enhancement of anisotropic behavior after photoexcitation [63], provided upper bounds for mobility values through spatial scanning study [64], and highlighted the carrier decay process at long time scales which was attributed to carrier lifetime, i.e. recombination [65]. A recent article investigated the decay process of excited carriers at short time scales on liquid exfoliated black phosphorus nanosheets and determined the carrier-phonon scattering times at a few different probing energy levels corresponding to commonly encountered laser emission lines [66]. Most ultrafast pump-probe studies are performed with one excitation wavelength and one probe wavelength. On the other hand, probing a range of wavelengths or equivalently a range of energy states, especially near the band edge, can uncover the vital information about the carrier relaxation process as demonstrated for graphene and MoS_2 [56,67,68]. In this study, we focus on understanding the evolution of the decay of excited states with varied probe energy approaching

the band gap of black phosphorus, and relate the ultrafast dynamics with fundamental transport properties. The scattering processes in black phosphorus in different directions are studied in order to gauge their importance in the observed anisotropic carrier mobility. A previous study [66] obtained a direction averaged scattering rate using randomly oriented flakes produced by liquid exfoliation and present the carrier dynamics at select probing energies.

In this chapter, we present data obtained on thin film of black phosphorus with 800 nm pump energy and varying probe energies around the bandgap, followed by analysis of the data. We systematically varied the probing direction and energies on a mechanically exfoliated flake, and find carrier scattering rates along the armchair and zigzag directions with a saturation of scattering time as the probe energy is tuned closer to and below the band edge, which helps to reveal the origin of anisotropic transport properties. The information on recombination was obtained when the probing wavelength was tuned to the band gap energy. Finally, the ultrafast spectroscopy data also revealed surface charge induced by oxidation.

2.1 Experiment on 65 nm black phosphorus flake

Bulk black phosphorus crystals are mechanically cleaved a few times (5-6) using Nitto dicing tape to obtain thin film flakes with flat and freshly exposed surface. The tape must be pulled rapidly to obtain good cleavage. A cotton earbud can be used to gently press the two tape pieces together before pulling to ensure a uniform bond. The flakes are then transferred to a clean (Ultra-sonicated with acetone and IPA for 5 minutes each) glass substrate. Gold coated markers were pre-fabricated on the glass substrate to determine the location of the flakes. To determine the arm-chair and zigzag directions (See section 1.3) of the flake, polarized Raman spectroscopy is performed, which is a fast and accurate method [16]. The Raman spectrum when the polarization direction is aligned with the armchair direction is shown in Figure 2.1, in agreement with previous studies. The B_g^2 peak (near 440 cm^{-1}) is nearly invisible, indicating good alignment between the laser polarization direction and the armchair direction.

The optical image of the sample is shown in Figure 2.1 as an inset. No degradation of the sample is observed before and after the experiments. This also is confirmed by the fact that the Raman signal, transient signal and appearance of the sample remained unchanged. The thickness of the sample is 65 nm as determined by atomic force microscopy (AFM) measurements.

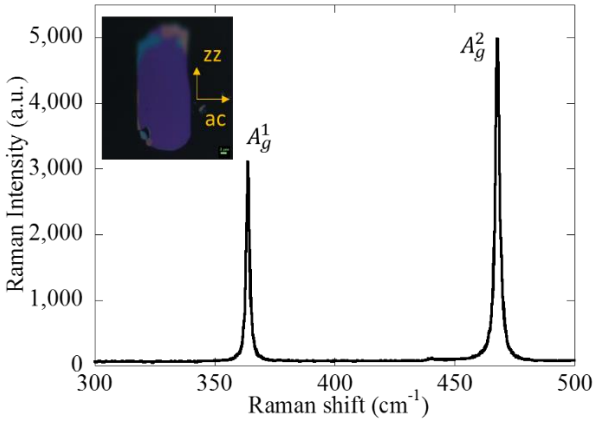

Figure 2.1: Armchair polarized Raman signal. Inset shows flake. Scale bar is 2 μm. zz stands for zigzag direction and ac stands for armchair direction.

A Coherent ultrafast Ti:Sapphire amplified laser system is used to generate 40 fs pulses at 792 nm center wavelength and 5 kHz repetition rate. The beam is split by a beam splitter and majority of the power is used to pump an optical parametric amplifier (OPA, Light Conversion) which generates wavelengths from 1.2 to 20 μm with 120 fs pulse duration. The weaker half is sent through a translation stage and is used to excite the sample. The OPA output is used as the probe. Once the pump and probe are made collinear, they are focused onto the sample surface using a 20x-0.42NA objective (Mitutoyo) for wavelengths up to 2.2 μm and with a parabolic mirror for longer wavelengths. The reflected light is re-collimated by the same objective/mirror and enters the photodetector (Thorlabs DET10D/Electro-optical systems MCT detector). The pump is chopped at a frequency of 500 Hz and lock-in detection is used to obtain good signal-to-noise ratio. A half-waveplate is used to control the polarization of the pump, whereas the sample is rotated to align it parallel or perpendicular to the probe polarization. A photograph of the setup (only near the sample) with parabolic mirror is shown in Figure 2.2.

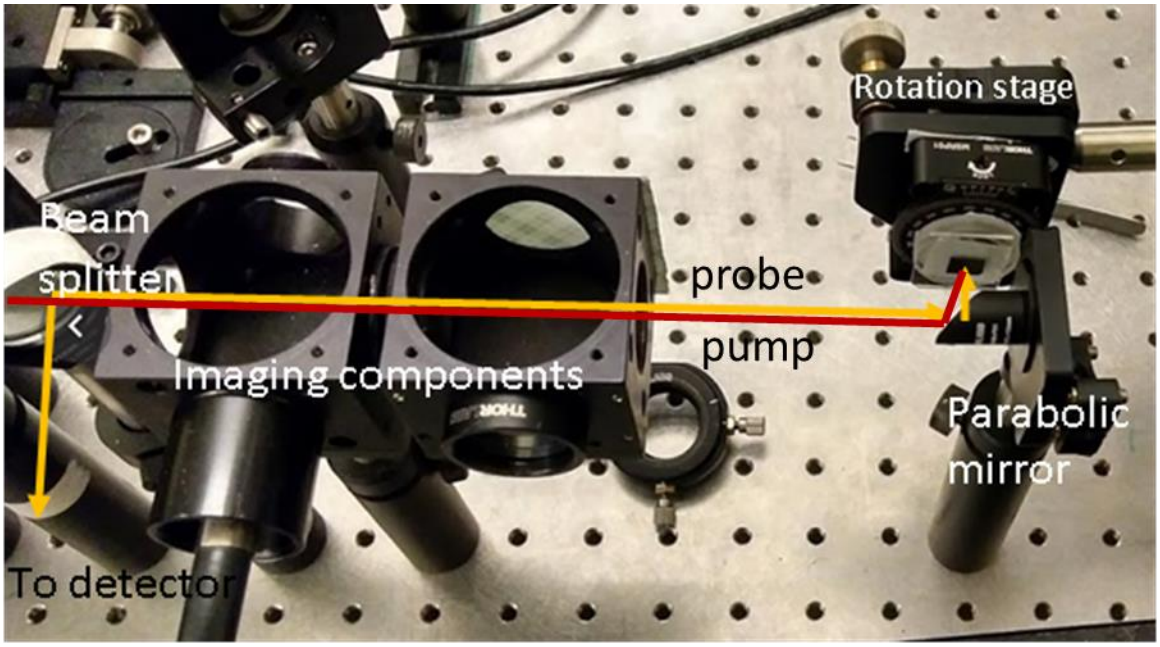

Figure 2.2: Picture of the setup with parabolic mirror

The diameter of the pump and probe spot is 10 μm and the probe is at least two orders of magnitude weaker than the pump. The pump energy is about 6 nJ per pulse and fluence dependence test confirmed a linear response of the acquired data around this pump energy as shown in Figure 2.3. Pure nitrogen is blown over the sample to prevent oxygen and water vapor from reaching the surface and degrading the sample. All experiments were done at room temperature.

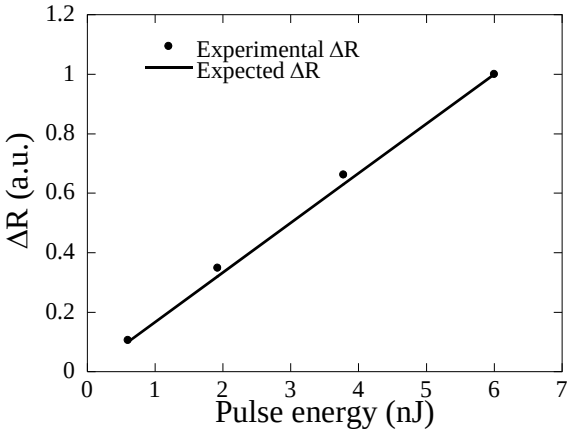

Figure 2.3: Fluence dependent reflectivity at 2,000 nm probe wavelength shows a linear response of the signal amplitude.

The transient reflectance data obtained using the 792 nm pump wavelength polarized along the armchair direction and probe wavelengths varied from 1,700 nm to 2,200 nm, also polarized along the armchair direction are presented in Figure 2.4a. Data for wavelengths from 2,500 nm to 4,600 nm are shown in Figure 2.4b. All the datasets have been normalized by their minimum values to -1. Change in reflectance is defined as the reflectance after pump excitation minus the reflectance without any pump excitation.

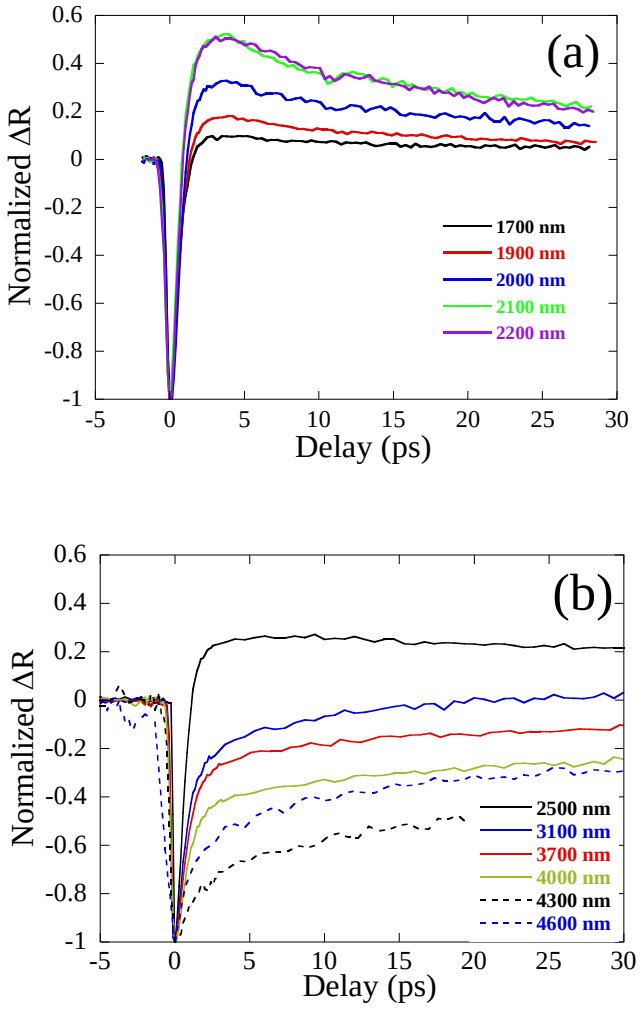

Figure 2.4: Transient reflectivity of black phosphorus for probing wavelengths from (a) 1,700 nm to 2,200 nm and (b) 2,500 nm to 4,600 nm.

During photoexcitation by a femtosecond laser pulse, carriers are generated at those energy levels in the conduction and valence band that correspond to vertical transitions in an E-k band diagram at the pumping energy. These carriers have momentum along the polarization direction

of the pump. They then randomize their momentum and energy by carrier-carrier scattering processes. This randomization process is fast and beyond the measurement time resolution as seen from Figure 2.5. The transient signal at maximum possible time resolution permitted by the system for armchair pumping and zigzag pumping keeping the probe polarization fixed along the armchair direction is found to begin and peak at the same delay for both cases. This indicates that carriers generated in the zigzag direction rapidly randomize their momentum and orient in the armchair direction.

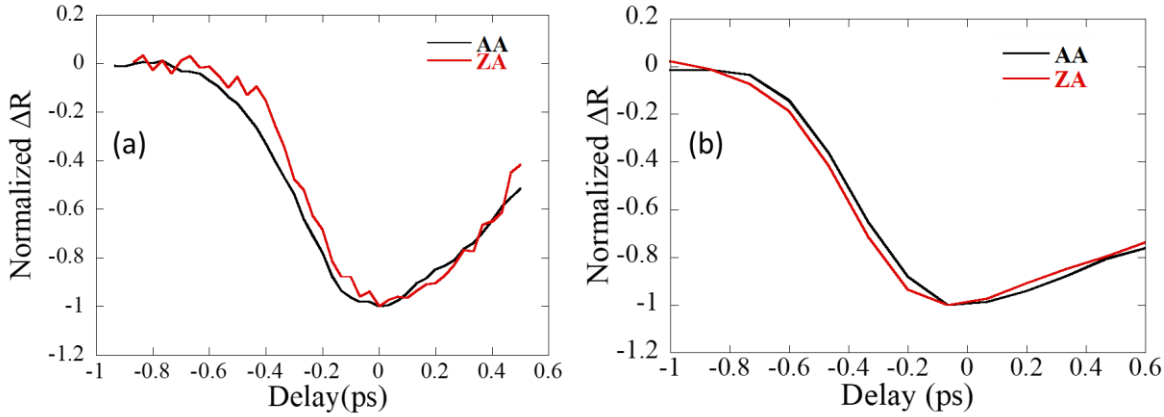

Figure 2.5: Fast randomization in k-space is observed by probing along the armchair direction with (a) 2,000 nm and (b) 4,000 nm but pumping along two perpendicular directions. AA stands for armchair pump and armchair probe. ZA stands for zigzag pump and armchair probe.

The next step is the formation of a thermalized distribution which can be represented by the Fermi-Dirac distribution. In order to achieve thermalization, carriers must move closer to the band edge in energy space and this implies intraband relaxation. The first decay in the experimental data starting at zero picosecond (rising from $\Delta R = -1$) and of the order of one picosecond is attributed to Pauli blocking (or electron bleach) and carrier-phonon scattering leading to the formation of a thermalized carrier distribution [65,66]. Pauli blocking is a result of occupation of carriers at the probing energy level. As the carriers emit phonons and relax to states closer to the band edge, the contribution from Pauli blocking diminishes, reflecting in the rise in the reflectivity signal. The second decay that starts from a few picoseconds, and is much slower, is attributed to the carrier recombination and lattice heating, and the time scales (10-100 picoseconds) are in good agreement with published work [63–65]. This second decay is thus an interband relaxation process.

As can be seen from Figure 2.6a, for wavelengths closer to the band edge, $\Delta R_{max}/R_0$ is greater. This is because energies closer to the band edge have a higher carrier population after carrier-carrier thermalization and thus produce a higher ΔR, though the distribution is non Fermi-Dirac. The data shown in Figure 2.6a also indicates that the bulk bandgap is close to 4,000 nm (0.31 eV), in agreement with previous theoretical work [12, 17, 39], recent FTIR data [18], and electrical measurements [48]. Additionally, a second peak about 40 meV below the band edge was also observed, which can be attributed to either exciton as theoretically predicted [46] or acceptor energy state as experimentally observed [69,70]. Figure 2.6b shows the temporal evolution of $\Delta R/R_0$ along with simulation using Fermi-Dirac statistics for carrier occupation. The experimental data can be well represented by the Fermi-Dirac distribution after carrier thermalization. The slight increase below 3000 nm is due to the sign change in the signal which arises due to the surface doping and will be discussed subsequently. The transient signal vanishes when the probe wavelength is above 4,600 nm (below the sub-band gap energy state)

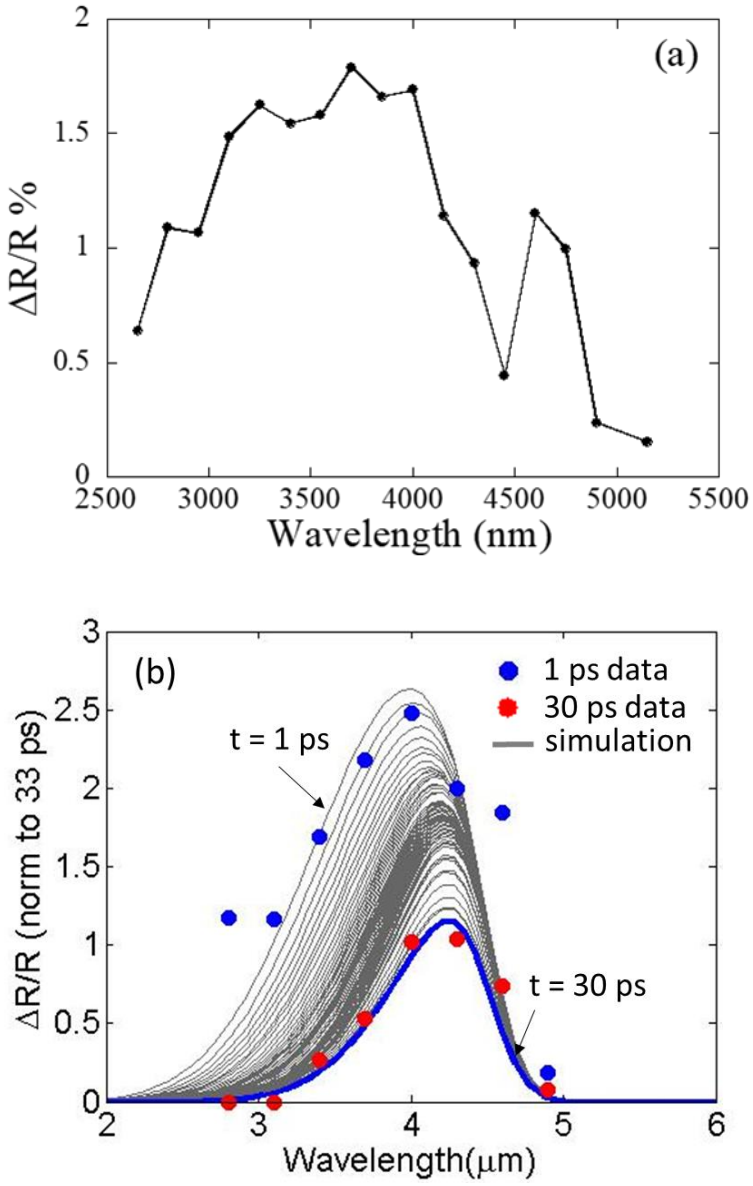

Figure 2.6: (a) ΔR(t=0)/R0 vs wavelength showing the bandgap near 0.31 eV and the presence of sub-band gap energy state. (b) Temporal evolution of ΔR/R0 showing the formation of Fermi-Dirac distribution

The simulation is performed by setting the Fermi-level at 0.05 eV above the valance band (p-type), resulting in a carrier density of $p_0 \sim 5 \times 10^{17}\ cm^{-3}$. Assuming $\frac{\Delta R}{R}(E) \propto \frac{\Delta p}{p_0}(E)$, the following set of equations describes the energy distribution of carriers:

$$p(E) = \big(1 - f(E)\big)D(E) \tag{2-1}$$

$$f(E) = \frac{1}{1 + \exp\left(\frac{E - E_f}{kT}\right)} \tag{2-2}$$

$$D(E) = \frac{\sqrt{2}(E)^{\frac{1}{2}}(m_{de})^{3/2}}{\pi^2 \hbar^3} \tag{2-3}$$

$$m_{de} = (m_1^* m_2^* m_3^*)^{1/3} \tag{2-4}$$

$\Delta p(E)$ results due to a perturbation in electronic temperature, T or Fermi-level E_f. $\Delta p(E)$ is convolved with the laser bandwith of 20 meV and then expressed as a function of wavelength, i.e. $\Delta p(\lambda)$. The Fermi level and electronic temperature are allowed to vary to obtain the best fit to the experimental data points and their temporal evolution is shown in Figure 2.7.

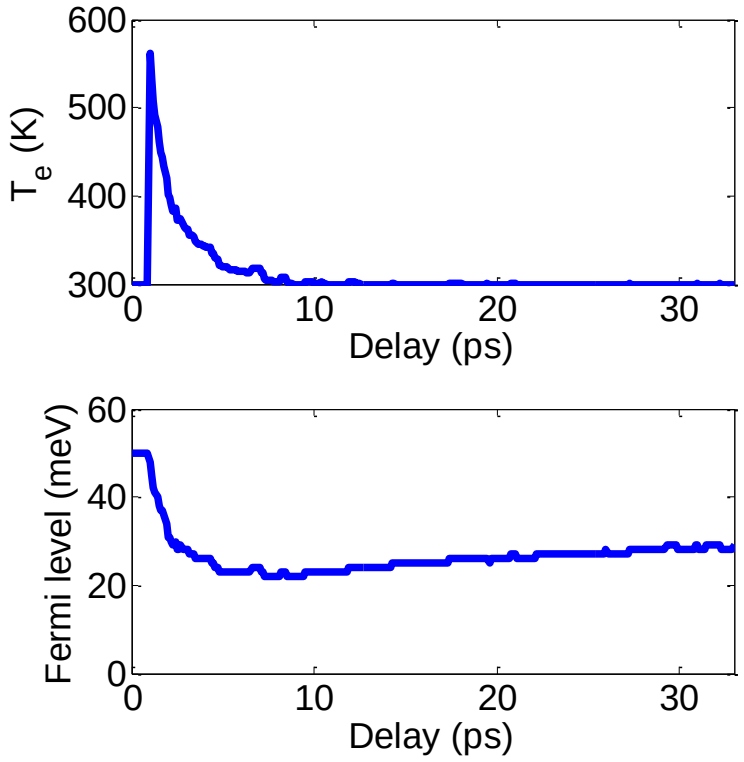

Figure 2.7: Temporal evolution of electronic temperature and Fermi-level

A rapid decrease in T_e is observed in the first 10 ps, which corresponds to hot-carrier cooling. The electrons rapidly exchange their energy with optical and acoustic phonon resulting in a lattice temperature rise. Because the lattice specific heat is much larger than the electronic specific heat, the change in lattice temperature is negligible (< 3 K), and hence the electrons cool down to near their initial temperature of 300 K. Within the same time span, a shift in the Fermi level in observed, indicating the increase in carrier density due to optical generation. The Fermi-level takes a significantly longer time to recover due to the slow recombination processes.

To further confirm the bandgap of black phosphorus, a relatively flat, thick piece of black phosphorus was placed on a 1 mm thick Calcium fluoride substrate for the transmission measurements. The substrate has a transmission of 95% for wavelengths ranging from 2 to 8 μm, and hence we have neglected all multiple reflection effects. The transmission of black phosphorus is calculated using equation 2-5 and shown in Figure 2.8. P_{flakes} is the power measured with the flakes and P_{input} is the input power.

$$T = \frac{P_{flakes}}{0.95 \times P_{input}} \tag{2-5}$$

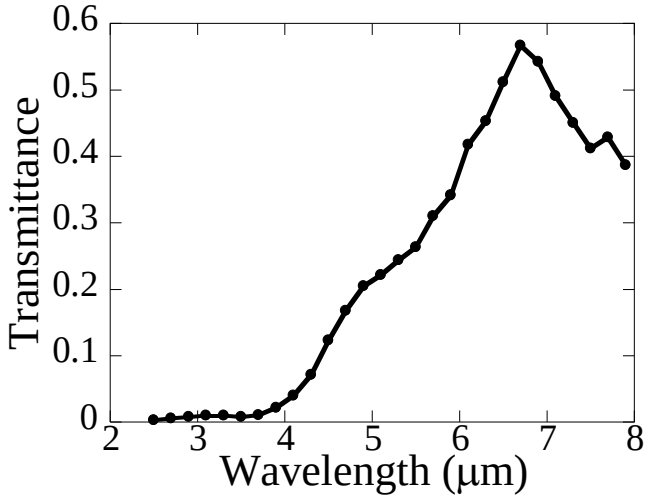

Figure 2.8: Transmittance of bulk black phosphorus. The flakes are randomly oriented.

The bandgap at around 4,000 nm is well resolved but the sub-band gap feature is not clearly visible. An increase and roll-off of the transmission below the bandgap at around 7000 nm is likely due to free carrier absorption as is observed in many semiconductors for infrared wavelengths [71].

To better understand anisotropic properties, tests at 2,200 nm and 4,000 nm for all polarization/sample orientation combinations was performed. The transient signals for the four combinations, namely, armchair pump-armchair probe (AA), armchair pump-zigzag probe (AZ), zigzag pump-armchair probe (ZA) and zigzag pump-zigzag probe (ZZ) are shown in Figure 2.9.

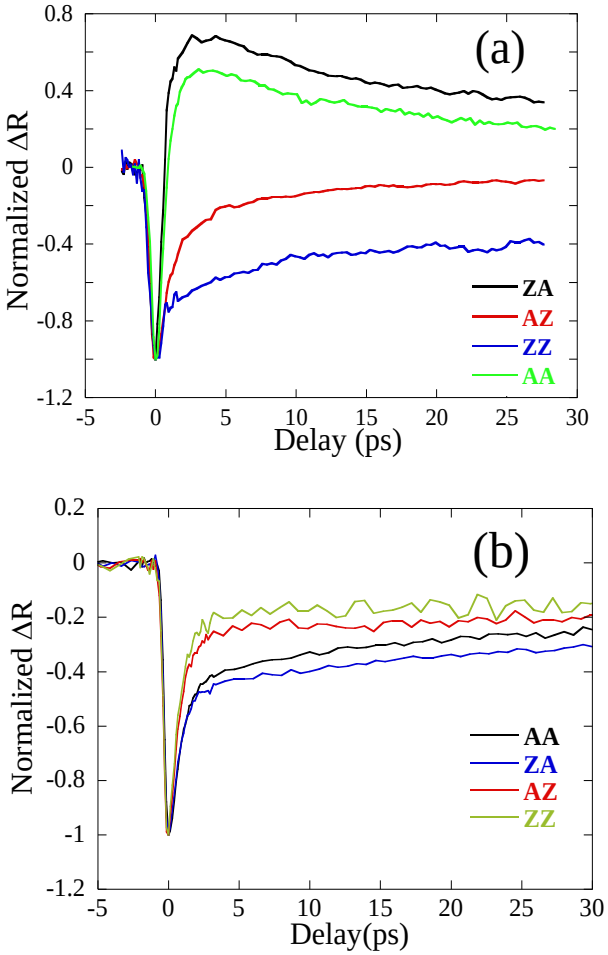

Figure 2.9: Transient reflectivity for ZA, AZ and ZZ and AA combinations using (a) 2,200 nm and (b) 4,000 nm probe wavelength.

It can be seen from Figure 2.9a that the sign of the signal changes from positive to negative only when probing along the armchair direction with 2,200 nm probe. The origin of the sign change will be discussed in section 2.3 and the lack of sign change in zigzag direction is attributed to the almost one order of magnitude larger effective mass compared to the armchair direction. For near

bandgap probing, Figure 2.9b, all pump probe combinations lead to similar dynamics with changes in absolute magnitude due to the anisotropic absorption.

2.2 Analysis of the transient dynamics

In this section, the obtained data from section 2.1 will be analyzed by performing fitting to the transient curves and using a simple model of surface oxidation to account for anomalous sign changes observed in Figure 2.4.

Bi-exponential fitting is used to extract the time constants for the fast and slow decays at different wavelengths:

$$\Delta R_{t>0} = A * \exp\left(-\frac{t}{\tau_1}\right) + B * \exp\left(-\frac{t}{\tau_2}\right) + C \qquad (2\text{-}6)$$

The constant term C is attributed to the much slower thermal energy dissipation due to lattice heating. A and B are the amplitudes for the exponentials. τ_1 and τ_2 are the fast and slow decay times. Examples of fitting for the 2,200 and 4,000 nm probes using Equation 2-6 are shown in Figure 2.10, which show that the bi-exponential function can represent the signals well. The peak transient signal amplitude was about 50 times the noise floor and the experiments were found to be repeatable when performed over a period of one week.

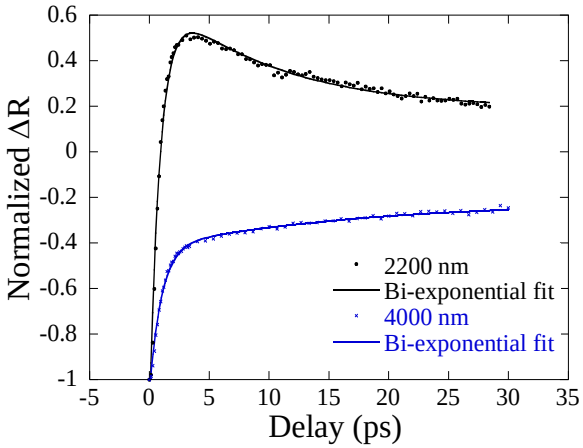

Figure 2.10: A least squares fitting routine is used to fit a bi-exponential curve for the transient data starting from delay time of 0 picoseconds.

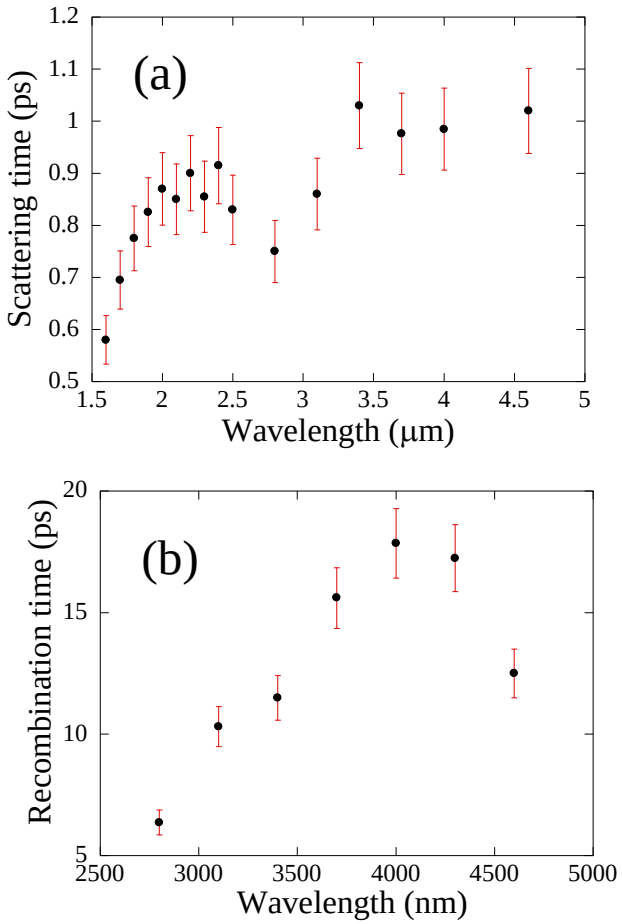

Figure 2.11: (a) Fast and (b) slow time constants with different probe energy. The fit uncertainty is about 8%.

Figure 2.11a shows that the carrier-phonon scattering time at different energy levels approaches a value of about 1 ps as the probe energy approaches the band gap energy. This increase in the scattering time can be understood by the fact that as carriers approach the band edge, there are fewer channels to dissipate energy in the intraband relaxation process. From the Raman measurements, the optical phonon energy for black phosphorus is about 50 meV. Though there are other lower energy phonon modes, their strength (population) is much lower compared to the A_g and B_{2g} mode phonons [72]. Probing the sample with 0.4 eV (3,100 nm) photons corresponds approximately to 50 meV above the band edge in both conduction and valence band. Since the excited carriers are expected to form a thermalized distribution a few meV above the band edge, carriers probed by 0.4 eV light are at the limit of one optical phonon emission, and probing with photon energy less than 0.4 eV leads to the relaxation time saturation behavior. Due to the

femtosecond pulse width, the high bandwidth of the laser (20meV energy resolution) is another limiting factor which could prevent us from observing the effects of lower energy phonon modes.

Using the carrier-phonon scattering times τ_1 obtained at the probing wavelength corresponding to the band gap, and $\mu = \frac{q\tau}{m^*}$, carrier mobility can be calculated. It is known that black phosphorus exhibits anisotropic transport properties along its armchair and zigzag directions such as mobility [12,19]. Therefore, carrier-phonon scattering time for the zigzag direction was extracted from data in Figure 2.9. All transient data can be fit with the bi-exponential function Eq. 2-6 and the fast relaxation time constant for zigzag probing is found to be about 0.9 ps at 4,000 nm, which is close to the value when using armchair probing.

An ambipolar mobility of about 1900 $cm^2/V{\cdot}s$ along the zigzag direction and 22,000 $cm^2/V{\cdot}s$ along the armchair direction are obtained. The effective mass of electrons (holes) along the armchair direction is taken as 0.0825 (0.0761) m_0 whereas along the zigzag direction is 1.027 (0.648) m_0 [72]. Since electrons and holes have similar effective mass, the ambipolar mobility, defined as $\mu_a = \frac{2\mu_e\mu_h}{\mu_e + \mu_h}$, can be considered as an average carrier mobility. The ambipolar mobility is determined from the experimental since the experimental data are a result of relaxation of both electrons and holes. The scattering time obtained is the upper limit for both holes and electrons, and given the comparable valence and conduction bands, similar scattering times are expected for electrons and holes. Our estimation of the mobility is reasonable compared to previous ultrafast experimental work (but with a probe wavelength of 810 nm) which determined a value of around 3000 $cm^2/V{\cdot}s$ for the zigzag direction and 50,000 $cm^2/V{\cdot}s$ for the armchair direction [64]. From Figure 2.11 we can see the importance of probing near the bandgap to extract the correct scattering rates needed in calculations. Theoretical study predicted values in the 10^3 $cm^2/V{\cdot}s$ range [19]. However for fabricated devices, the mobilities were found not to exceed 1000 $cm^2/V{\cdot}s$ [12,15,45,54,73,74]. The bulk and surface impurity scattering at equilibrium, which affects only the momentum of carriers (not their energy), would account for further reduction in mobility in devices which were not captured in the ultrafast spectroscopy experiments that are sensitive to changes in energy. Thus our experiment provides an upper limit for mobility.

The slow decay time (recombination time), τ_2, also increases when the probing wavelength approaches the band gap energy. This is because the carriers, not at the band edge (4,000 nm), scatter with phonons and move toward low energy levels. Hence, due to the additional relaxation

channel, the higher energy carriers appear to have a faster recombination time. The recombination time, independent of carrier phonon scattering, must be evaluated at the bandgap energy. At the 4,000 nm probing wavelength, the recombination time τ_2 is found to be about 18 ps. Figure 2.11b also shows that the recombination time at sub-band gap wavelength 4,600 nm is about 12 ps. Since the data indicate both sub-band gap carriers and carriers in the delocalized bands relax with a comparable time, we expect a similar recombination mechanism for both, e.g., phonon assisted recombination. It is likely that the sub-band gap signal arises from acceptor states (vs. from excitons) because it displays features similar to the band edge probe (4,000 nm). These states are filled after rapid carrier-carrier scattering (fast drop in ΔR) and subsequently carrier-phonon scattering displaces carriers from the sub-band gap states to the delocalized states (fast rise in ΔR). For excitons, we would expect a different dynamics because the bound states should possibly show much longer decay times [39,68].

2.3 Calculation of surface doped layer thickness

It is worthwhile to look more closely at the relaxation process as the wavelength is varied. For shorter wavelengths (e.g., 2,200 nm, Figure 2.4a), a positive peak is observed, but the peak does not rise above zero for wavelengths longer than 3,100 nm (Figure 2.4b). We propose that such optical response is related to surface charges. It is known that oxidation can induce surface doping on the order of 10^{12} cm^{-2} [73]. Photoexcited holes in the bulk thermalize close to the band edge whereas photoexcited holes at the surface thermalize with the existing hole population due to doping by oxidation. This creates an excess hole population at slightly higher energies in the valence band and changes the dielectric constant. The change in dielectric constant is reflected in the spectroscopy data, which indicates variation of the (peak) reflectivity at different probing wavelengths corresponding to different energy levels in the valence band. A calculation of the change in the dielectric constant at the surface and bulk and its relation it to the change in reflectivity is performed.

We begin by considering the sample's band diagram with surface doping as shown in Figure 2.12.

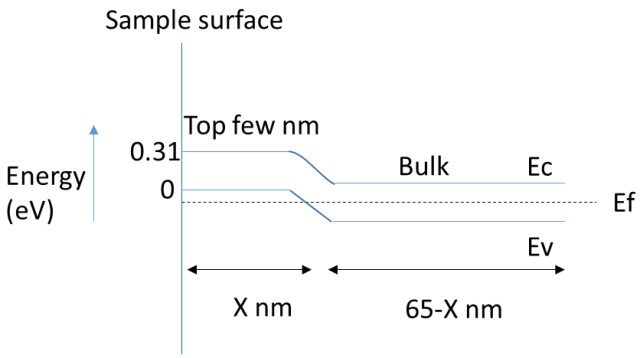

Figure 2.12: Band diagram of surface doped black phosphorus

We can first calculate the hole density N as a function of energy (in the valence band) as follows [75]:

$$N(E) = \big(1 - f(E)\big)D(E) \tag{2-7}$$

$$f(E) = \frac{1}{1 + \exp(\frac{E - Ef}{kT})} \tag{2-8}$$

$$D(E) = \frac{\sqrt{2}(E_h - E)^{\frac{1}{2}}(m_{de})^{3/2}}{\pi^2 \hbar^3} \tag{2-9}$$

$$m_{de} = (m_1^* m_2^* m_3^*)^{1/3} \tag{2-10}$$

where N is the carrier density, f is the Fermi-Dirac distribution, D is the density of states, m_{de} is the density of states effective mass, $\hbar$ is the reduced Planck's constant, and k is the Boltzmann constant. The zero reference is taken as the valence band maximum as shown in Figure 2.12. The effective mass values are obtained from literature [72]. The choice of fermi-level E_f determines the population distribution. For E_f = -0.077 eV, which is obtained iteratively to match our experimental data (see below, Figure 2.16), the hole distribution is shown in Figure 2.13.

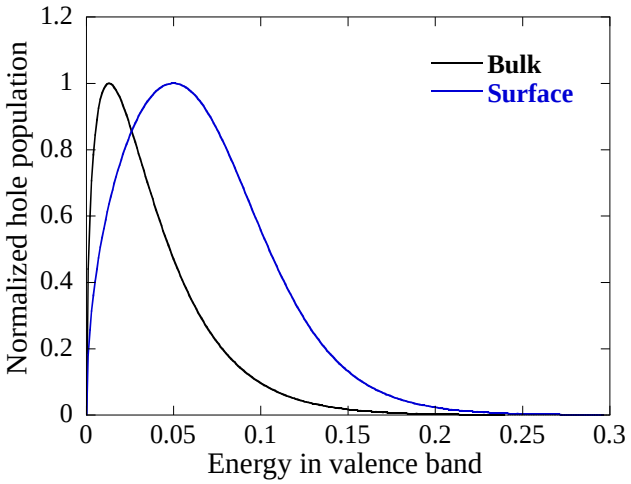

Figure 2.13: Hole population in bulk and surface doped layers

After optical excitation, new carriers are generated which thermalize with the existing population. This can be modeled as a perturbation in the Fermi level. The calculated change in carrier population using Eq. 2-7, after applying the perturbation, as a function of energy in the valence band is shown in Figure 2.14. Black phosphorus has similar effective mass for conduction and valence band and hence the dynamics are expected to be similar. Therefore, for simplicity we only consider bulk valence band carrier contribution. The surface contribution exists only in the valence band.

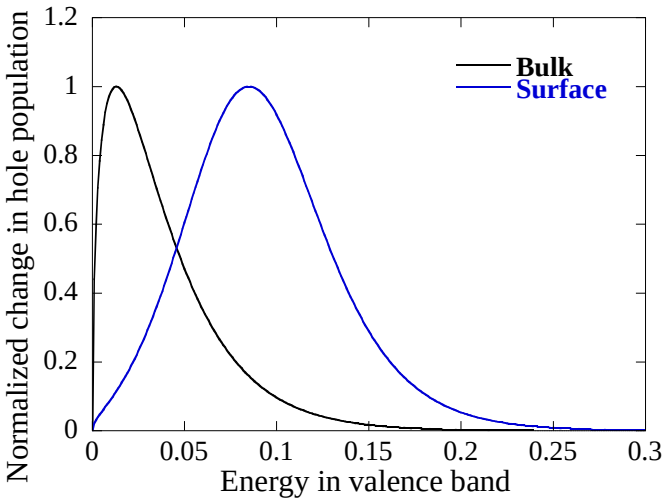

Figure 2.14: Change in hole population for small perturbation in fermi level

The change in the imaginary part of the dielectric constant, $\Delta\varepsilon_2$, is proportional to the change in carrier population but with an opposite sign, i.e. for an increase in population, $\Delta\varepsilon_2$ decreases. We have made this assumption based on the fact that ε_2 is related to loss in metals and dielectrics [76]. The increased occupation of states would lead to lower absorption and hence a lower loss. The change in the real part of the dielectric constant, $\Delta\varepsilon_1$, is then obtained by Kramers-Kronig integration. The calculated change in optical constants as a function of energy in the valence band is presented in Figure 2.15.

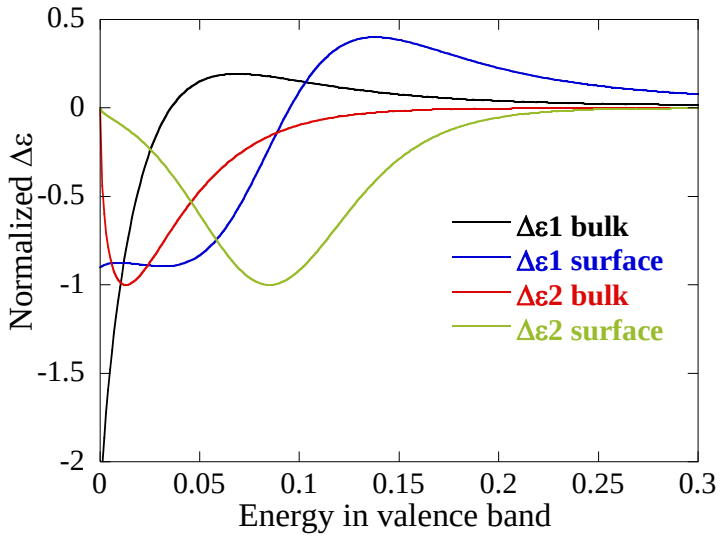

Figure 2.15: Change in dielectric constant after photoexcitation

We can then calculate the change in reflectivity as a result of the change in optical constants using multilayer reflectivity model as [77]:

$$\frac{\Delta R}{R} = \frac{\left(\frac{\partial R}{\partial \varepsilon_1}\Big|_{surf}\Delta\varepsilon_{1,surf} + \frac{\partial R}{\partial \varepsilon_2}\Big|_{surf}\Delta\varepsilon_{2,surf} + \frac{\partial R}{\partial \varepsilon_1}\Big|_{bulk}\Delta\varepsilon_{1,bulk} + \frac{\partial R}{\partial \varepsilon_2}\Big|_{bulk}\Delta\varepsilon_{2,bulk}\right)}{R} \quad (2\text{-}11)$$

$$r = \frac{\gamma_0 m_{11} + \gamma_0\gamma_s m_{12} - m_{21} - \gamma_s m_{22}}{\gamma_0 m_{11} + \gamma_0\gamma_s m_{12} + m_{21} + \gamma_s m_{22}} \quad (2\text{-}12)$$

$$\gamma_0 = n_0\sqrt{\varepsilon_0\mu_0},\ \gamma_s = n_s\sqrt{\varepsilon_0\mu_0} \quad (2\text{-}13)$$

$$R = r * r^* \quad (2\text{-}14)$$

n_0 and n_s are the refractive indices of air and glass (substrate). m_{11}, m_{12}, m_{21}, and m_{22} are the resultant matrix elements. ε_0, μ_0 are the permittivity and permeability of free space. The reflectance (Eq 2-14) was numerically differentiated with respect to each of the four ε's and then multiplied with the obtained Δε's. ε_1 and ε_2 at 1,550 nm was measured to be 10.5 and 2.15, respectively, along

the armchair direction. This value was used for all wavelengths as an estimation. The thickness of the layers, X and 65-X (see Figure 2.12), are embedded in the matrix elements and so is the wavelength.

For a given value of dopant density the change in dielectric constant is calculated by perturbing the fermi-level as discussed previously. The dopant density also yields a surface layer thickness of X = 5.7 nm by using the measured surface carrier density of 7.5×10^{12} cm^{-2} [2]. The reflectivity from the entire structure is then calculated

Various values of the dopant density were used till the calculated $\Delta R/R$ as a function of probe wavelength matches the experimental data for wavelengths around 2,000 nm as shown in Figure 2.16. For the data shown in Figure 2.16, the dopant density value used is 1.3×10^{19} cm^{-3} (Fermi-level of -0.077 eV), and the corresponding X is 5.7 nm.

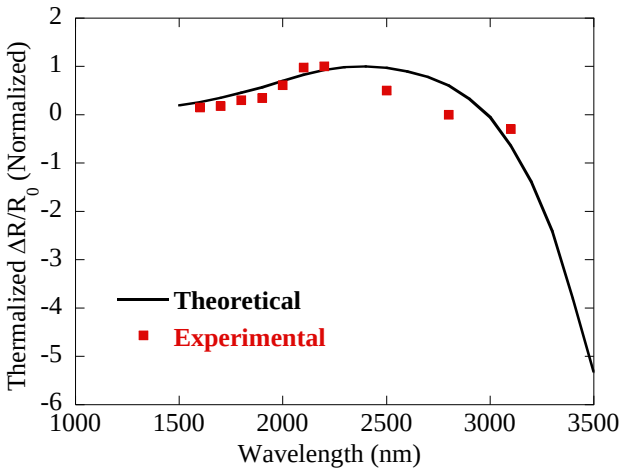

Figure 2.16: Theoretical estimate of $\Delta R/R$ and experimental values.

The positive reflectivity does not appear in the data using zigzag direction probing (Figure 2.9b) because for the same Fermi level, the population density in the zigzag direction is one order of magnitude higher than in the armchair direction owing to the large effective mass. The sensitivity is thus lost in the large background surface hole density. These features in the transient reflectivity signals were also observed in other works [63,65] at similar wavelengths but no detailed discussions were given. The MATLAB code for the above calculation is provided in Appendix A.

2.4 Experiments and observations on bulk crystals of black phosphorus

Before experiments were performed on 65 nm thin film of black phosphorus, thick bulk crystal (~1mm) were investigated to acquire a general understanding of the material. Some of the relevant observation that are different from thin film are summarized in this section.

Coherent oscillations were observed on a thick crystal of black phosphorus when pumped with 800 nm and probed with 2000 nm light as shown in Figure 2.17a.

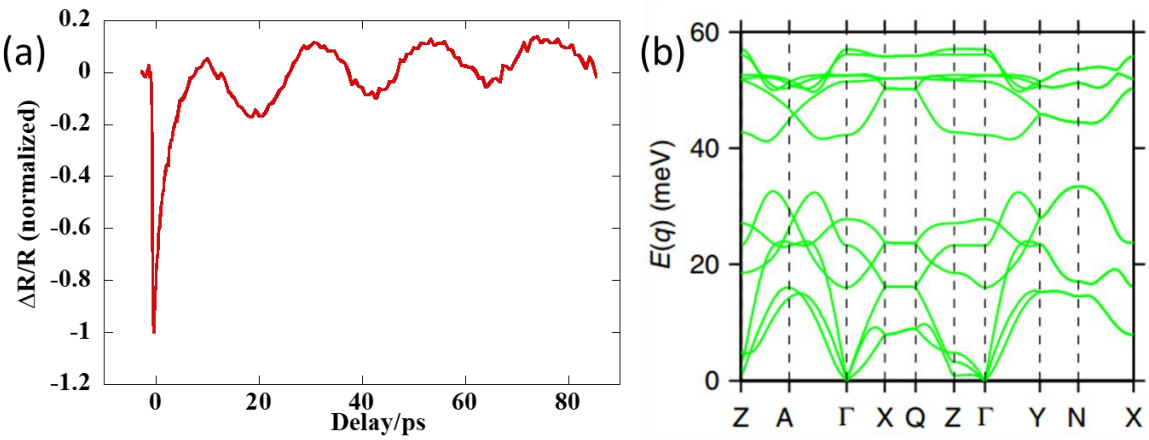

Figure 2.17: (a) Coherent acoustic phonon oscillations in bulk crystal of black phosphorus pumped with 800 nm and probed with 2,000 nm light and (b) calculated phonon band structure of black phosphorus [16] .

The period of the oscillations is 21 ps seconds, which corresponds to 0.2 meV and hence the phonon mode likely arises from the zone center, judging by the phonon band structure of black phosphorus, Figure 2.17b [16]. Since light has negligible linear momentum, quasiparticles like electrons and phonons near the zone center typically respond more strongly to the light field. Figure 2.18 shows another instance of very low energy phonon mode as observed when the sample is pumped with 800 nm light and probed with 1350 nm. Such oscillations have also been observed in other 2-D materials like MoS_2 [78] and Bi_2Se_3 [79], where the phonon mode was identified as coherent longitudinal acoustic phonon. The timescales are also similar, ranging from few picoseconds to 10s of picoseconds. A photo-induced thermo-modulation mechanism, where the sudden heating of the laser irradiated surface causes heating of phonons and stress due to expansion, is the likely explanation. This stress converts to a strain wave and generation of longitudinal phonons propagating away from the surface. The mechanism is also described in literature as

impulsive stimulated Brillouin scattering (ISBS) [80], a counterpart of impulsive stimulated Raman scattering (ISRS) for optical phonon generation [81].

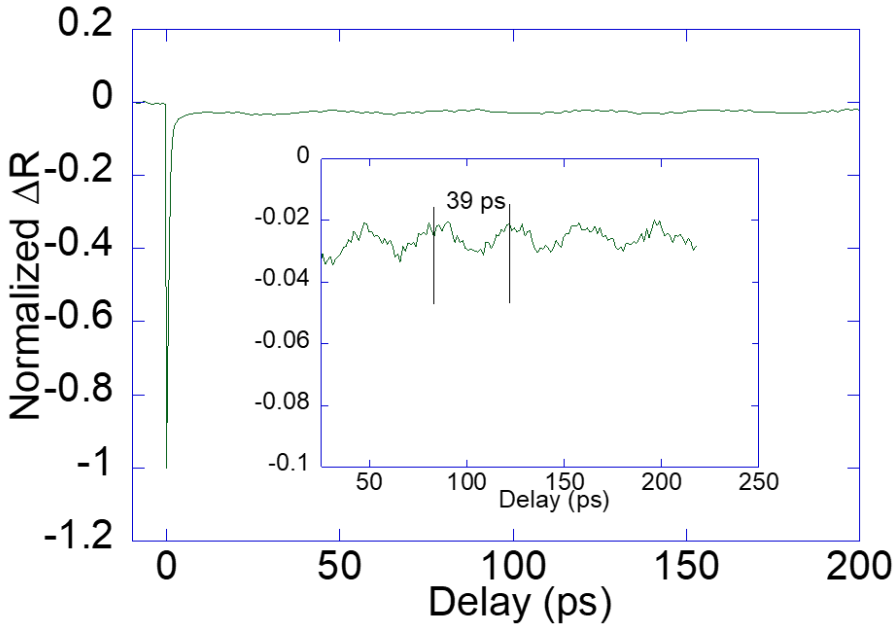

Figure 2.18: Lower energy acoustic phonon in black phosphorus. Inset shows the oscillations with 39 ps duration.

Another set of experiments were performed on very thick flakes (~10 μm) of black phosphorus that were peeled onto the tape from the bulk crystals but not transferred onto any substrate. The tape was directly mounted on the sample holder for experiments. An optical image of the flakes is shown in Figure 2.19, along with the boundary between two adjacent flakes marked by the black oval.

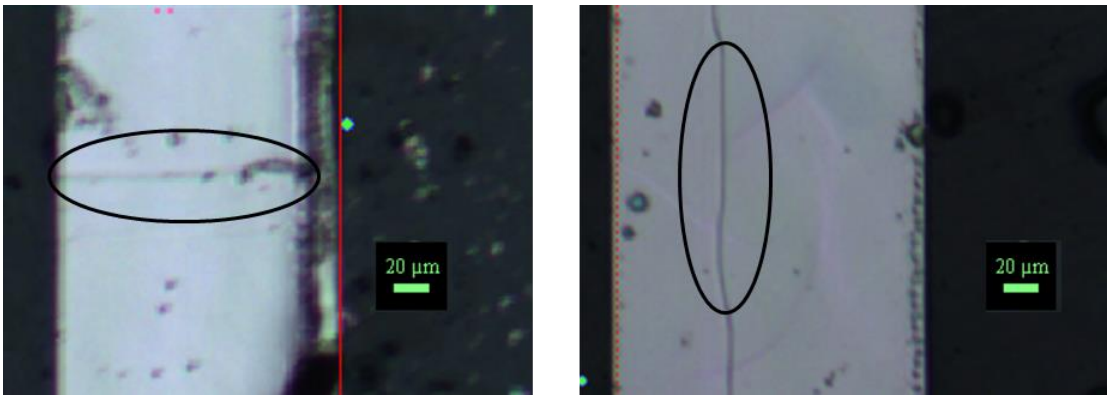

Figure 2.19: Bulk black phosphorus flakes on dicing tape. The black oval shows the boundary between two flakes.

The sign of the transient reflectance varies periodically with wavelength and is exactly complementary for the flakes on the two sides of the boundary as shown in Figure 2.20.

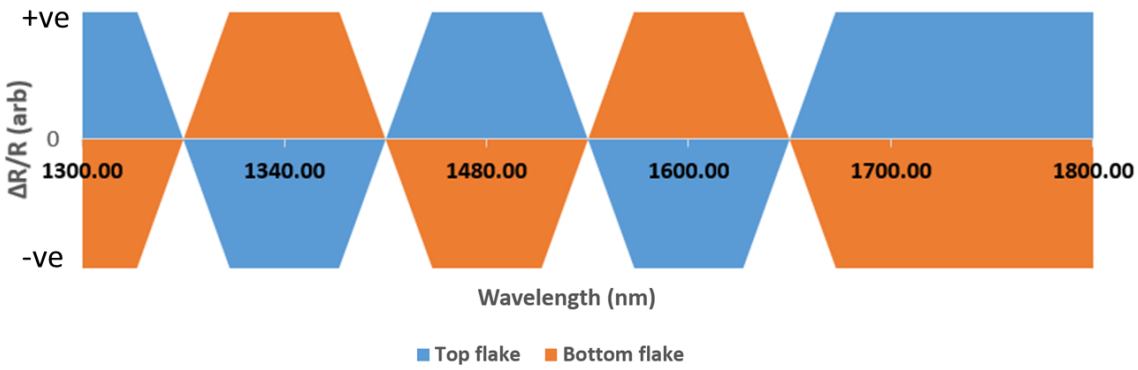

Figure 2.20: Opposite sign across the boundary for flakes shown in Figure 2.19, from 1300 to 1800 nm probing in the zigzag direction.

A possible explanation could be the effects of compressive and tensile strain on the flakes arising at the boundaries. The sign of the signal far away from the boundary was the same for both flakes and hence this effect can be exclusively attributed boundary related modifications. Furthermore, the absence of this effect for armchair direction and strong modulation when probing in the zigzag direction is in agreement with theoretical works, which calculated changes in band structure due to strain and found larger changes in the zigzag direction as compared with armchair direction [82,83] .

2.5 Summary

In conclusion, we have carried out ultrafast infrared spectroscopy on thin film black phosphorus and found that the near band gap phonon-scattering time is close to 1 picosecond which is limited by the optical phonon scattering processes. By investigating energy relaxation of carriers with a tunable probe energy, it is found that carrier-phonon scattering time saturates when the probe energy reaches close to the band edge, which can be used to extract fundamental properties such as mobility. From the transient reflectivity data for different excitation and probing polarizations corresponding to the different anisotropic directions in black phosphorus, we find a similar scattering time along the armchair and zigzag directions. The major factor controlling the carrier mobility is thus the difference in the effective mass resulted from anisotropic band structure of the material rather than the scattering processes. The recombination time was seen to increase as the probing wavelength approached the band edge. A sub-band gap energy state was also observed and attributed to acceptor states. We used an optical property model for qualitatively explaining the spectroscopic features in the data, and found contributions due to surface doping by oxidation. Our work shows the importance of selecting the right probing wavelengths to study carrier dynamics in semiconductors displaying variety of interesting phenomena. Lastly, experiment on bulk flakes revealed coherent acoustic phonon oscillations and boundary induced strain effects.

3. ULTRAFAST STUDIES ON THIN FILMS OF SOLUTION GROWN TELLURIUM

This chapter has been partially reproduced from a previous publication: *Iyer, V.; Segovia, M.; Wang, Y.; Wu, W.; Ye, P.; Xu, X. Infrared Ultrafast Spectroscopy of Solution-Grown Thin Film Tellurium. Phys. Rev. B* ***2019****, 100 (7), 075436.*

Two-dimensional (2D) materials are being intensely studied to ascertain their utility for next generation of transistors, photodetectors, interconnects and a host of other components [14,43,84]. After several successful applications of graphene [5,40], its limited performance in transistors due to lack of band gap [85] lead to investigation and discovery of many other 2D materials such as transition metal dichalcogenides [86], black phosphorus [12,45], and topological insulators [87]. Even these new materials suffered from some limitations. For example, transition metal dichalcogenides exhibit low electron/hole mobilities in general [88,89] and black phosphorus is unstable in air due to oxidation [90]. The enhanced properties of topological insulator surface states could not be harnessed to their full potential due to bulk contribution [91]. Another major challenge is the fabrication of these 2D materials on a large scale, with extensive efforts being invested in techniques such as chemical vapor deposition [92], molecular beam epitaxy [93], and liquid phase exfoliation [94]. Only a few materials such as some transition metal dichalcogenides and graphene are being produced on wafer scale [95,96].

Tellurium, like black phosphorus, is an elemental two-dimensional material which is emerging as a promising candidate for electronic and optoelectronic applications. A novel substrate free solution growth method has been developed which facilitates controllable flake thickness [13,97]. Moreover, using the Langmuir–Blodgett process and ink-jet printing, the flakes can be assembled to obtain large area samples [13]. Apart from the feasibility of scalable growth, tellurium transistors have been shown to exhibit high mobility, good on/off ratio, and large drain current [13,98–100]. Furthermore, the bandgap is thickness tunable, which could prove useful in tunable light absorption [13]. Finally, the material is air stable without the need for encapsulation [13], thus overcoming many of limitations discussed previously. A more detailed description of the properties of this material can be found in a recent review [101]. Due to the rising interest in this material, it is important to understand the fundamental electron/hole carrier dynamics which directly impacts the performance of devices. Ultrafast pump-probe spectroscopy

is a useful tool to investigate hot carrier dynamics, carrier scattering and recombination in a variety of materials such as nanoparticles [102], quantum dots [103], metals [38], and 2D materials [104,105]. There have been ultrafast studies on the coherent phonon dynamics in bulk tellurium crystals [106,107], but no studies on the near bandgap and free carrier dynamics on thin films to the best of our knowledge. Since most devices rely on near band edge phenomena, it is essential to understand the infrared transient response of the material, which can access the small bandgap of 0.35 eV [22].

3.1 Experimental setup and sample characterization

To carry out the infrared pump-probe spectroscopy, we use a commercial Coherent Ti-Sapphire amplified laser system (800 nm, 40 fs, 5 kHz). A part of the laser output is used as the pump beam and the remainder is sent through an optical parametric amplifier (Light Conversion, Opera Solo) to obtain the mid-infrared probe pulses through difference frequency generation. The time resolution in mid-IR is about 500 fs. The pump and probe beam are focused though a reflective objective to avoid chromatic aberration. The pump beam is slightly enlarged using a lens pair to achieve uniform excitation in the probe region. The transmitted probe beam is collected onto a liquid nitrogen cooled HgCdTe detector (Electro Optical Systems Inc.). The pump probe delay is controlled by a mechanical stage with 13 fs resolution and the pump is chopped at 500 Hz to enable lock-in detection. A gate integrator (Stanford Research Systems) is used to increase the duty cycle of the signals and offset the background to allow amplification. The pump fluence was set at 0.02 mJ/cm^2 and the probe fluence was about 0.05 mJ/cm^2. The pump absorption coefficients from reflection and transmission measurements were obtained as $\alpha_{\parallel c} = 2.12 \times 10^5\ cm^{-1}$ and $\alpha_{\perp c} = 1.18 \times 10^5\ cm^{-1}$. The absorption coefficient for the probe is expected to be about 2 to 3 orders of magnitude lower [22] and could not be accurately measured due to the low absorption in the thin films used in this work. The pump excited carrier concentration is ~ 2 x 10^{18} cm^{-3}. The low absorption coefficient of the probe ensures at least one order of magnitude lower carrier excitation compared to the pump. The experiments were performed at room temperature.

Tellurium flakes were obtained using the solution growth method (courtesy Yixui Wang and Dr. Wenzhuo Wu, Industrial Engineering, Purdue University) as discussed earlier and the suspended 2D Te flakes were scooped out from the solution onto a CaF_2 substrate with pre-

deposited gold location markers. The flakes were identified with an optical microscope (Figure 3.1a), followed by collecting a Raman spectrum (Horiba LabRAM, Figure 3.1b, courtesy Mauricio Segovia) to determine the flake orientation [13]. The red arrow in Figure 3.1a is the direction perpendicular to the c-axis (or parallel to $[1\bar{2}10]$ axis) and the blue arrow is parallel to the c-axis ($[0001]$ axis). An AFM scan was done to determine the thickness. FTIR (Fourier-Transform Infrared Spectroscopy) transmission scans were also performed using an FTIR microscope (Thermo Fisher Scientific, Continuum) as shown in Figure 3.1c for three flakes of thickness 14, 60 and 160 nm. The point where the slope changes in the 160 nm flake, indicated by the intersected straight line in Figure 3.1c, corresponds to the bandgap of 0.35 eV. The 14 nm flake shows weak hump like features near 0.3 eV, which could be due to many body effects such as excitons. A recent study theoretically predicted exciton binding energy of up to 670 meV in monolayer suspended tellurium, and decreased strength for supported samples and thicker films [108]. Detailed thickness dependent photoluminescence excitation spectroscopy [109,110] could reveal more details and is beyond the scope of this work. Bulk flakes were predicted to have <10 meV binding energy at room temperature and hence we have neglected excitonic effects in our analysis for >20 nm flakes. More discussion on <20 nm samples will be provided later. Ultrafast pump-probe transmission spectroscopy was carried out on the flakes. The change in transmission ($\Delta T/T$) at a pump-and-probe delay time of 7 ps, for a 130 nm flake, with the probe wavelength varying across the bandgap, is shown in Figure 3.1d. The pump and probe were both either polarized along the c-axis ($\parallel$ c) or perpendicular to the c-axis ($\perp$ c). The transmission data for light polarization perpendicular to the c-axis is more indicative to the bandgap, as has been observed previously in literature for bulk crystal [22]. The photo generated carriers accumulate near the band edge, hence there is a larger change in the transmission of the probe when its wavelength is tuned close to the bandgap. The change of transmission vs. wavelength can be seen clearer by fitting a spline curve through the experimental data points by performing a numerical differentiation [111] to obtain the point of maximum, which is indicated by the black dashed line at 0.355 eV. The pump and probe were polarized perpendicular to the c-axis in the remainder of the manuscript.

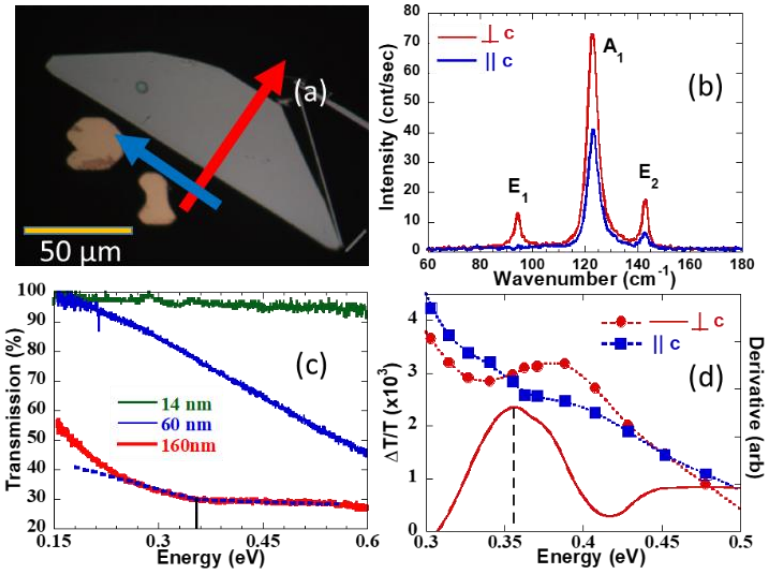

Figure 3.1: Characterization of a 130 nm flake using (a) optical microscopy and (b) Raman spectroscopy to determine orientation. (c) FTIR transmission for flakes with various thicknesses. The change in the slope of the curve for the 160 nm flake corresponds to the bandgap of 0.35 eV. (d) The change in transmission at 7 ps delay for a 130 nm flake as a function of energy for pump and probe polarizations either oriented perpendicular or parallel to the c-axis, with spline fits (dotted lines) and its derivative (solid line). The band edge near 0.35 eV is clearly discernable for light polarization perpendicular to the c-axis.

3.2 Thickness and fluence dependence of transient dynamics

The relaxation dynamics of 40 to 160 nm flakes following excitation by the 800 nm (1.55 eV) pump beam is shown in Figure 3.2a for a bandedge probe wavelength of 3500 nm (0.35eV). The pump fluence is 0.02 mJ/cm^2. Fluence dependent dynamics for 130 nm flake are shown in Figure 3.2b. The recombination dynamics in tellurium has been studied previously using steady state [112] and transient photoconductivity [113], as well as transient microwave conductivity [114]. These studies did not have the time-resolution to determine the recombination time at room temperature. The reported values at low temperature (77 K) range in the 10s of ns to microsecond regime and the authors predicted room temperature recombination time to be several orders smaller than at low temperature. A recent study on recombination dynamics in powdered tellurium obtained few nanosecond lifetimes at room temperature using transient microwave conductivity with a minimum time resolution of 300 ps [115]. Our measurements are the first on thin film tellurium with sub-picosecond time resolution.

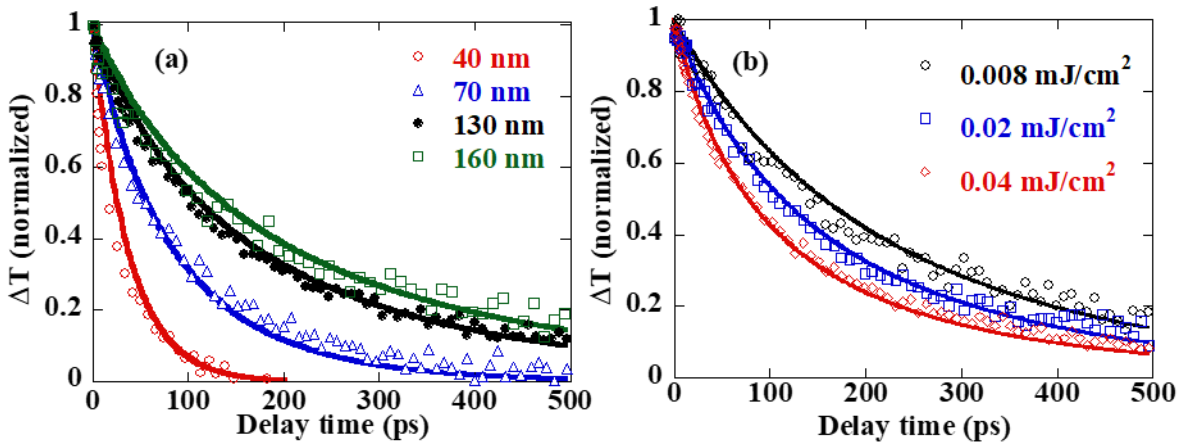

Figure 3.2: (a) Relaxation dynamics in 40 to 160 nm flakes following excitation by 800 nm pump and probing with 3500 nm. The transient curves are normalized, and the point of maximum signal is set as delay time of 0 ps. The solid lines are obtained from diffusion-recombination model simulations. (b) Fluence dependent measurements on a 130 nm flake along with simulation curves.

A diffusion-recombination model was used to simulate the dynamics as shown by the solid lines in Figure 3.2a and Figure 3.2b. Several recombination mechanisms have been proposed for bulk tellurium in literature such as direct recombination [112], trap/defect states near the band edge [113], mid-gap trap states [114], and point defects and dislocations [116]. The TEM cross section of the flakes in a previous study revealed good quality of the flakes in the bulk and hence point defects and dislocations are less likely [13]. Therefore radiative or SRH (Shockley-Read-Hall, trap assisted) recombination are the more probable recombination routes, as was also deduced in a recent study on recombination dynamics in powdered tellurium [115]. Moreover, the authors found that radiative recombination is dominant with 98% radiative yield at room temperature. Hence, we modeled the dynamics with radiative recombination (which accounts for the fluence dependence) and surface recombination (which accounts for the thickness dependence), and the diffusion process.

3.3 Simulation of transient dynamics with diffusion-recombination model

The general diffusion equation with radiative recombination can be written as:

$$\frac{d(\Delta N)}{dt} = D\frac{d^2(\Delta N)}{dx^2} - B(np - {n_i}^2) + G(t,x) \qquad (3\text{-}1)$$

Where ΔN is the excess carrier concentration (m^{-3}), D is the diffusion coefficient (m^2s^{-1}) and B is the radiative recombination coefficient (m^3s^{-1}). G(t,x) is the laser generation term ($m^{-3}s^{-1}$) which is given as:

$$G(t,x) = \exp\left(-2.77 * \frac{(t)^2}{tp^2}\right) * \frac{(1 - R - T) * \frac{fluence}{tp * (\delta)} * \exp(-x/\delta)}{(h * c/\lambda_{pump})} \quad (3\text{-}2)$$

tp is the pulse duration (100 fs), R and T are the reflectance and transmittance of the sample, δ is the penetration depth perpendicular to the c-axis (85 nm), h is the Planck's constant, c is the speed of light and λ_{pump} is the pump wavelength (800 nm). The fluence is calculated as: $\frac{(power)}{Rep\ rate * \pi * r_p^2}$. The repetition rate is 5000 Hz and the pump spot size r_p (radius) is determined from knife edge experiment:

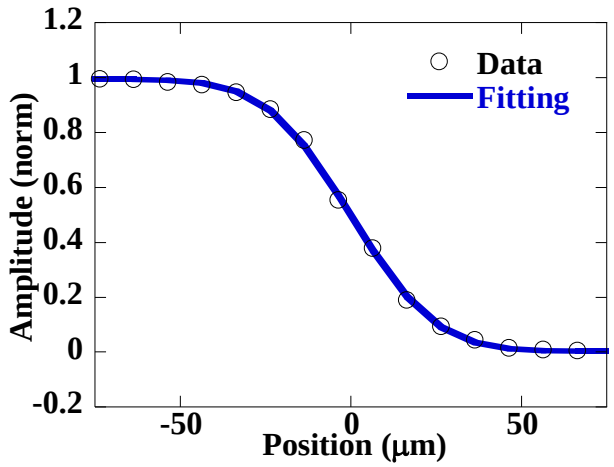

Figure 3.3: Pump beam radius of 39 μm measured by knife edge method.

n_i is calculated as [75]:

$$n_i = 4.9x10^{15}\left(\frac{m_{de}m_{dh}}{m_0^2}\right)^{3/4} T^{3/2} e^{-E_g/2kT} \quad (3\text{-}3)$$

With m_{de} ~ 0.2 and m_{dh} ~ 0.3 [117] and $E_g = 0.35\ eV$, we obtain n_i ~ 3.5 x 10^{15} cm^{-3}.

$$p = p_0 + p_{excited} \sim 5 \times 10^{17} + p_{excited} \quad (3\text{-}4)$$

$$n = n_0 + n_{excited} = \frac{{n_i}^2}{p_0} + n_{excited} = 2.5 \times 10^{13} + n_{excited} \quad (3\text{-}5)$$

$p_{excited} = n_{excited} = \Delta N$ due to optical excitation.

The simulation is carried out in COMSOL Multiphysics commercial software. The surface recombination is prescribed as a boundary term and the surface recombination velocity is expressed as:

$$V_s = 2 \times 10^6 \frac{1\ nm}{thickness\ (nm)}\ \text{[cm/s]} \quad (3\text{-}6)$$

Solving the equations above provides ΔN as a function of time. Finally we compare ΔN(t), which is normalized along the sample depth since the probe penetrates the entire depth of the sample, with the experimentally obtained ΔT (normalized). (Note the computing averaged ΔN or total ΔN along the depth gives the same result as the data is normalized.) Hence we make a one-to-one comparison between our simulations and experiment such that ΔT (normalized) = ΔN (normalized).

By fitting the radiative recombination coefficient and surface recombination term, we obtained good agreements with experiments as seen in Figure 3.2a and Figure 3.2b for both thickness dependent and fluence dependent data. The radiative recombination coefficient was obtained as $1.9 \mp 0.1 \times 10^{-9}$ cm^3/s. Our value is lower than the 1.1×10^{-8} cm^3/s obtained by Bhaskar et al [115] but higher than other traditional direct bandgap semiconductors such as GaAs which has a value of ~7×10^{-10} cm^3/s at room temperature. The surface recombination velocity is found as $V_s = \frac{2 \times 10^6}{t}$ cm/s, where t is the thickness in nm. Typically, the Fuchs-Sondheimer theory was used to account for the thickness dependent electrical resistivity, which has a ~1/t dependence for t>>λ, where λ is the mean free path [118,119]. The 1/t trend obtained from our modeling is likely a lumped effect from a number of phenomena such as scattering and possible thickness dependent surface defects.

3.4 Dynamics of very thin flakes

Flakes with smaller thicknesses show different dynamics, and a transition occurs around 40 nm thickness as shown in Figure 3.4a. The sign of the transmission signal starts flipping from positive to negative accompanied by a shorter time constant of decay. Comparing the 3500 nm

probe and 5800 nm probe for the 40 nm flake, we see that after the change in sign from negative to positive for 5800 nm probe, the curves merge at about 50 ps. This shows that there are two distinct relaxation processes. As the thickness is reduced further, the signs for both probe wavelengths become negative and the lifetime is sub 20 ps, as seen in Figure 3.4b for a 12 nm flake with 3500 nm probe. The simulation reproduces the fast relaxation well, as shown by the blue solid line in Figure 3.4b. Two more flakes with thickness 13 and 17 nm produced similar results.

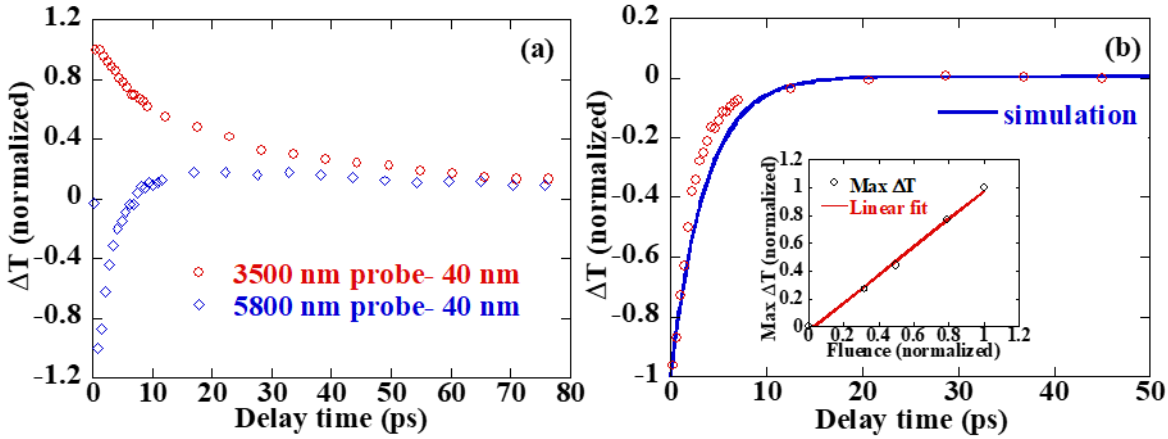

Figure 3.4: (a) Relaxation dynamics in a 40 nm thick flake, showing positive sign (3500nm probe) and sign flipping (5800 nm probe). At delays greater than 50 ps, the curves merge together. (b) Relaxation dynamics in 12 nm flake following excitation by 800 nm pump and probing with 3500 nm. Inset shows pump fluence dependence along with linear fit, confirming absence of any non-linear effects. The blue solid line is from the diffusion-recombination simulation.

In thinner flakes, the observed relaxation is entirely due to carrier capture by surface trap states. The mobility of transistors made from solution grown tellurium was seen to sharply decrease below 20 nm thickness [13] and was ascribed to surface scattering and interface defects.. Such timescales have been previously related to fast capture of carriers by mid gap defect states in MoS_2 [62]. To ensure that the drastic change in the signal is not due to non-linear effects such as Auger recombination, we show the maximum change in transmission as a function of fluence and observe a linear trend as shown in the inset of Figure 3.4b, which rules out such possibilities. A fluence test on relaxation time, as shown in Figure 3.5, revealed fluence independent relaxation which further suggests surface recombination as the dominant mechanism in thin flakes.

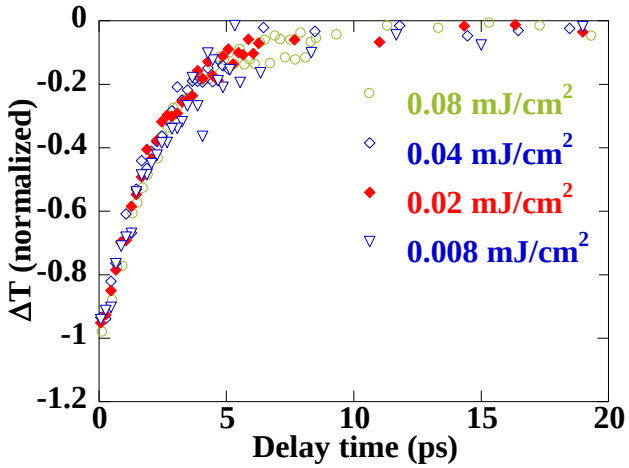

Figure 3.5: Pump fluence dependence for 12 nm film showing fluence independent relaxation.

The fluence dependence for 130 nm sample as shown in Figure 3.2b indicates second order (N^2) or higher order contribution to relaxation mechanism, since the slope changes with fluence. For thin flakes, however, since the fluence dependence vanishes, we expect a first order process to dominate. Since the surface recombination ~ V_s*N, it is linear and hence the main channel of relaxation.

We also address the thickness dependence of the bandgap, as it is known to increase from bulk to monolayer [13]. The thickness dependence of the bandgap is theoretically approximated by calculations as [13]:

$E_g = 0.38 + 0.70/t$ (eV), where t is in nm. Thus for our thinnest flake with 12 nm thickness, the bandgap is expected to increase by ~50 meV and approach ~0.4 eV. We measured the dynamics with a 2800 nm (0.44 eV), but did not observe any difference compared to the 3500 nm (0.35 eV) probe, as shown in Figure 3.6.

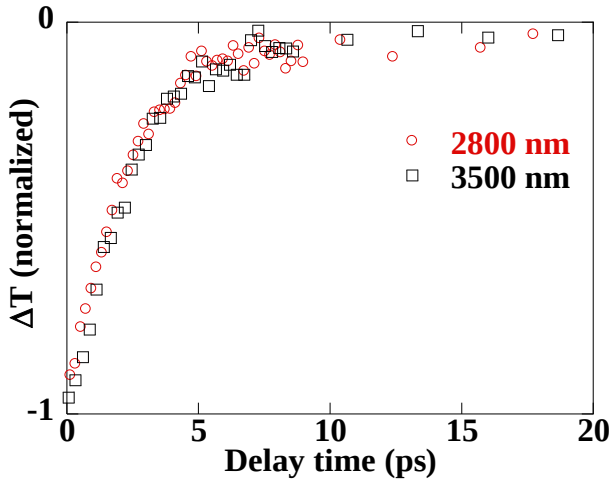

Figure 3.6: Higher probe energy dynamics in 12 nm flake

We also performed a probe wavelength sweep near time delay of 0 ps, as shown in Figure 3.7 and found only weak features similar to the FTIR spectrum shown in Figure 3.1c, 14 nm flake.

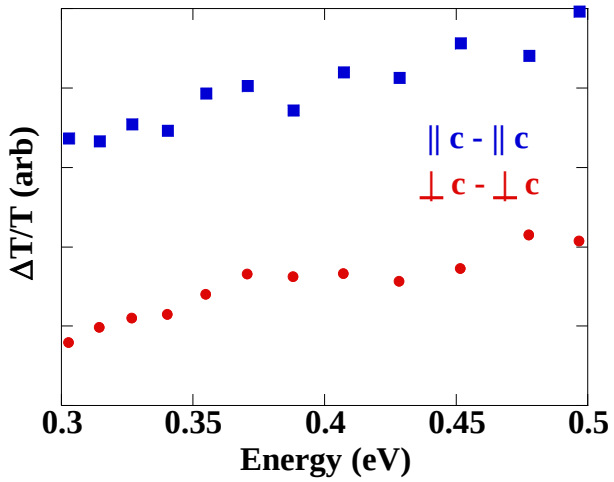

Figure 3.7: Probe wavelength sweep for 12 nm flake at 1 ps delay

Hence we conclude that either the bandgap did not change as predicted or that the 3500 nm probe monitors the free carriers and hence does not show any difference compared to the near bandgap probe of 2800 nm, similar to probing with 5800 nm probe. Excitonic effects could play a role in the thin films as discussed earlier, however the exciton lifetimes are generally in the 100s

of ps to ns range [120–122], unlike the short timescales in our measurements. Some studies found the lifetime to be in <10 ps at very low temperature of 4 K, but 100s of ps at room temperature [123,124]. Furthermore, timescales of <5 ps at room temperature was attributed to trapping of excitons by surface defects in MoS_2 [68]. Therefore, we conclude that even with possible exciton activity for the thin flakes, the surface defect assisted relaxation is the dominant process at room temperature.

3.5 Summary of processes and directional dependence

The excitation and recombination processes can be summarized in Figure 3.8. Figure 3.8a describes thick flakes and Figure 3.8b describes thin flakes. Before the arrival of the pump pulse ($t < 0$, left column), the material is at its ground state (p-type [13]). At the time of excitation, ($t = 0$, center column), the pump pulse completes populating the higher energy states, i.e. conduction band in the thick flakes and both conduction band and mid-gap trap states in the thin flakes. Intraband thermalization process (on the order of 100 fs in common 2D materials [37,60]) occurs within the time resolution of our experiment (500 fs). After rapid carrier-phonon scattering, carrier recombination occurs. In case of thin flakes, since the recombination proceeds through the many mid-gap trap states, it must necessarily be phonon assisted as shown, which explains why the recombination time is on the order the electron-phonon interaction times.

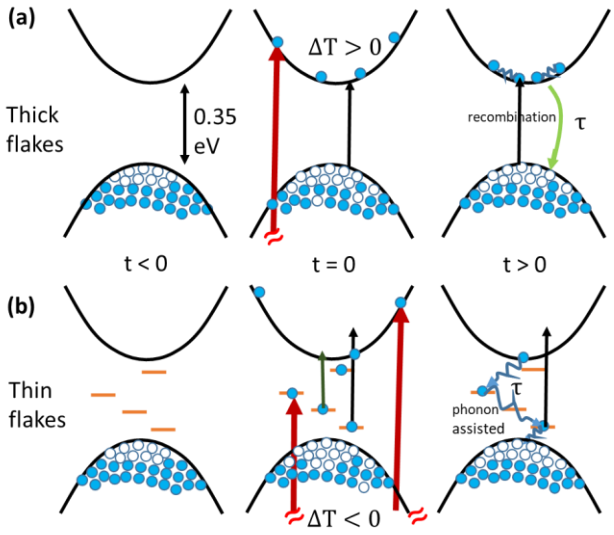

Figure 3.8: Excitation and relaxation mechanism in thick flakes (upper 3 panels), where direct recombination plays a dominant role, and in thin flakes (10-20 nm, lower 3 panels), where the excited carriers recombine predominantly through several mid-gap surface trap states. The red arrow denotes the pump beam (800 nm), the black and dark green arrows represent the 3500 nm and 5800 nm probe respectively. The white circles are the holes and blue circles are the electrons. The orange bars are trap states.

The proposed ultrafast transmission mechanisms in Figure 3.8 also explains the increase or decrease transmission in thick and thin flakes. The positive sign of the transmission signal (induced transmission) in thick flakes indicates Pauli blocking between initial and final states, thus indicating interband probing as shown in Figure 3.8a. The 3500 nm probe monitors the valence band to conduction band transition, whereas the 5800 nm probe monitors inter-valence band transitions, several of which, in the mid-infrared region, have been found in literature [13,117,125–127]. On the other hand, thin flakes show a negative transmission signal (induced absorption), thereby indicating transitions from mid-gap trap states to the conduction band as shown in Figure 3.8b. For the transition flake (40 nm flake, Figure 3.4a), the negative signal from the mid-gap trap states and the positive signal from the Pauli-blocking start to compete. The 3500 nm probe response is dominated by interband transition, due to it being the primary strong transition, whereas the 5800 nm probe starts to encounter a superposition of responses from inter-valence band states and mid-gap trap states, producing a sign change.

Lastly we looked at the transient dynamics with pump and probe polarizations in the direction parallel to the c-axis. The absorption coefficient of the pump laser is different along the

c-axis and perpendicular to it by a factor of 1.8 for 130 nm flake (see section 3.1), and hence pumping and probing along the c-axis should produce a change in the slope of the relaxation due to different initial exited carrier concentration. We observe such a dependence as shown in.

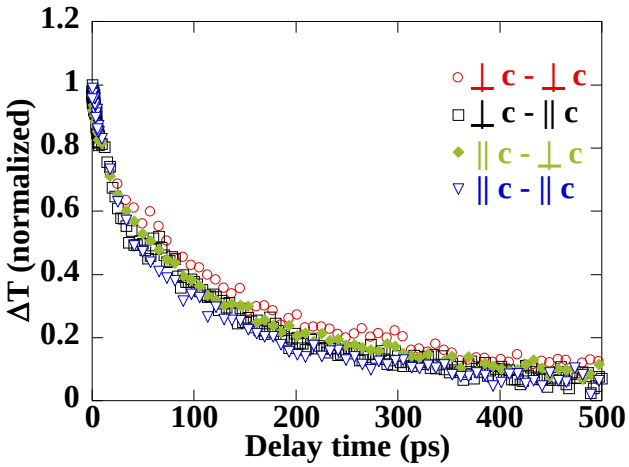

Figure 3.9: Dynamics for 130 nm flake with pump and probe polarized along different directions. ⊥c-|| c indicated that the pump is polarized perpendicular to the c-axis and the probe is polarized along the c-axis. The difference in slope is due to the different excited carrier concentrations from absorptivity difference along the two directions.

The thinner flakes did not show any directional dependence and reinforce the fluence independent surface recombination mechanism as shown in Figure 3.10.

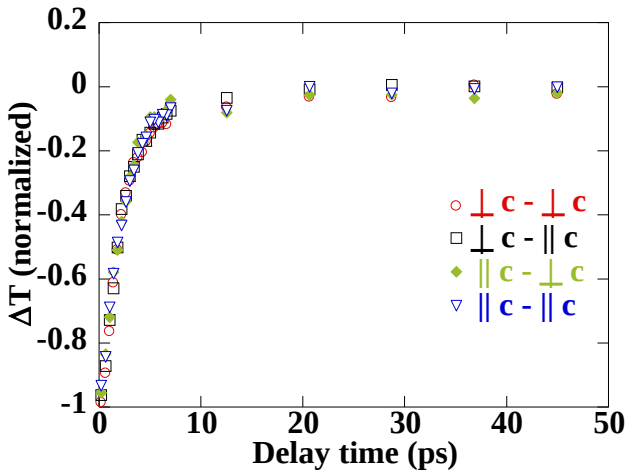

Figure 3.10: Dynamics for 12 nm flake with pump and probe polarized along different directions. The directionally independent dynamics suggests surface recombination dominant relaxation which is independent of initial carrier concentration.

3.6 Modeling mobility with surface and bulk scattering

Thickness dependent electrical measurements on transistors revealed a strongly thickness dependent mobility which was attributed to surface scattering [13]. Here we develop a scattering based model to qualitatively reproduce the observed field-effect mobilities. We begin by using the Matthiessen's rule which states that the reciprocal of the total scattering time, τ_{tot}, equal to the sum of the reciprocals of the individual scattering terms:

$$\frac{1}{\tau_{tot}} = \frac{1}{\tau_{surf}} + \frac{1}{\tau_{bulk}} \tag{3-7}$$

$$\text{Or, } \Gamma_{tot} = \Gamma_{surf} + \Gamma_{bulk} \tag{3-8}$$

We already showed that the surface recombination velocity is inversely proportional to the thickness (Eq. (3-6)), and hence we assume that the surface scattering is also inversely proportional to thickness, i.e. $\Gamma_{surf} = \frac{A}{\delta}$, where δ is the thickness. The bulk scattering is taken to be proportional to the thickness, i.e. $\Gamma_{bulk} = B * \delta$. For back-gated field effect transistors, the entire channel is typically depleted and serves to transport electrons. Hence, with increasing thickness, the electrons see a larger channel depth which can lead to interlayer scattering as was also observed

in MoS_2 [128]. Therefore we assumed a thickness dependent bulk scattering. The mobility can be written as:

$$\mu = \frac{q\tau_{tot}}{m} = \frac{q}{m}\left(\frac{\delta}{A + B\delta^2}\right) \tag{3-9}$$

A and B are fitting parameters to quantitatively reproduce the experimental data observed in literature [13]. The theoretically obtained curve using Eq.(3-9 is overlaid on the experimental graph adopted from [13] and is shown in Figure 3.11.

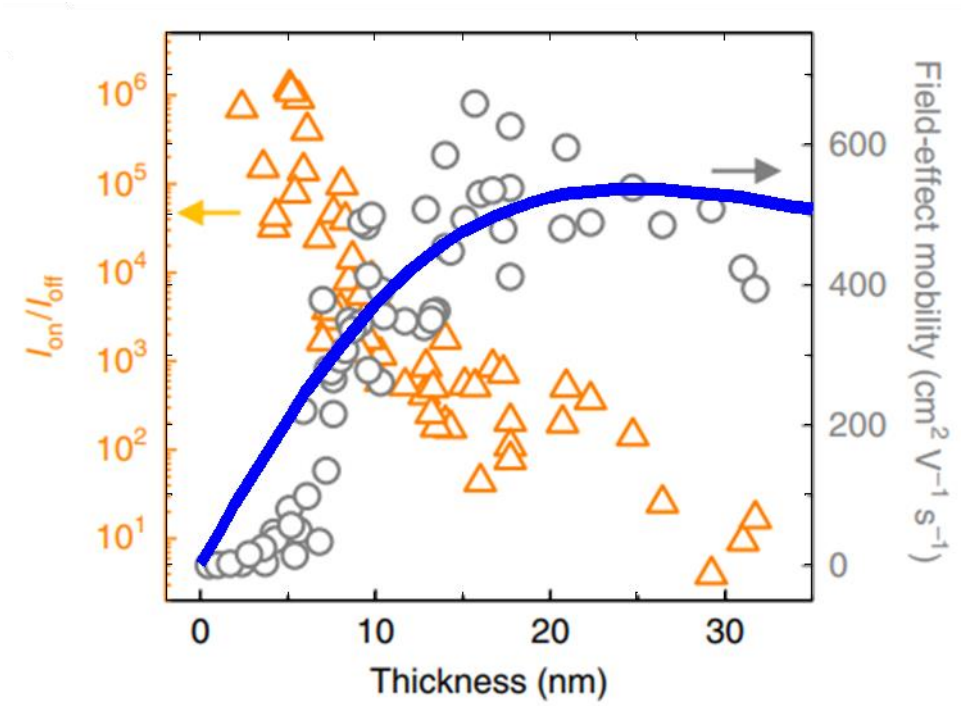

Figure 3.11: Theoretical mobility overlaid on experimental graph reproduced from [13]

The simple theory provides a good fit to the experimental data. Hence the ultrafast studies provide the critical information to assess the surface scattering dependence.

In summary, we have performed ultrafast infrared transmission spectroscopy on tellurium flakes with thicknesses ranging from 12 nm to 160 nm and found a strong dependence of the recombination times on thickness. Thin flakes show a fast decay on the order of 20 ps, whereas thicker flakes have a decay in the 100s of ps range. The recombination mechanism in thin flakes was attributed to fast carrier capture by mid-gap defect states arising from surface defects and that in the thick flakes to radiative recombination. Recombination coefficients were extracted using a

diffusion-recombination model. A bulk and surface scattering model is used to compute thickness dependent mobility and the results agree well with measured field-effect mobility. The fundamental carrier dynamics for tellurium thin films at room temperature aids in the understanding and better design of electronic and opto-electronic devices.

4. ULTRAFAST SURFACE SPIN CARRIER DYNAMICS IN TOPOLOGICAL INSULATOR Bi_2Te_2Se

This chapter has been partially reproduced from a previous publication: *Iyer, V.; Chen, Y. P.; Xu, X. Ultrafast Surface State Spin-Carrier Dynamics in the Topological Insulator Bi_2Te_2Se. Phys. Rev. Lett.* ***2018****, 121 (2), 026807.*

Topological insulator (TI) surface states possess properties such as spin-momentum locking and backscattering protection [129–133], and high mobility [134–136] which makes them suited for spintronics applications [137,138]. Unlike conventional electronics that utilizes electron's charge, spintronics exploits electron's spin to perform logic operations. A long spin lifetime ensures that information carried by spin is not lost during device operation [139,140]. Therefore, surface states (SS) protected from backscattering are natural candidates for the task. Furthermore, their high mobility can afford faster switching of devices. The widely studied Dirac states in graphene exhibit long spin diffusion lengths (upto 20 μm) upon electrical injection of spin [141,142]. However, they lack spin-momentum locking which prevents branch selective optical injection of spin. On the other hand, circularly polarized light has been shown theoretically [143] and experimentally [32,144] to excite only one branch of the spin-momentum locked surface states in TIs. Optical spin control is thus an alternative to conventional magnetic or electric control of devices [145,146]. It is therefore important to examine the interaction of light with SS and understand the resulting charge carrier and spin dynamics.

The fundamental carrier relaxation dynamics of the Dirac like SS following photoexcitation has been studied using angle-resolved photoemission spectroscopy (ARPES) [147–153], terahertz pump-probe spectroscopy [154,155], photoluminescence spectroscopy [156] and optical pump-probe spectroscopy [157–159]. ARPES, performed mostly on doped Bi_2Se_3 and Bi_2Te_3, utilized energy windows to independently track relaxation of conduction band, valence band, SS, and the coupling between bulk and SS. Most studies used an above bandgap pump and probe energy with linear polarization resulting in interband transitions along with uniform excitation of both branches of the Dirac cone. There is, however, very limited literature on using circularly polarized light to create asymmetric excitations in the SS and study spin dynamics, which is more relevant to optical spin control. Most of the aforementioned works focused only on charge dynamics. Wang and co-workers studied the spin dynamics in Bi_2Se_3 of

the second Dirac cone lying above the bulk conduction band and found sub-picosecond relaxation [160]. Similarly, Hsieh et al observed a sub-picosecond spin relaxation in Bi_2Se_3 using second harmonic probing [159]. Recently, Kuroda and co-workers demonstrated asymmetric excitation of SS in Sb_2Te_3 lasting a few picoseconds with excitation energy below the band gap and subsequent photoemission [152,153]. Apart from the all optical studies, an opto-electronic approach demonstrated spin lifetime of several picoseconds in Bi_2Se_3 [161].

Compared to widely studied Bi_2Se_3 and Bi_2Te_3, topological insulators Bi_2Te_2Se (BTS) and $BiSbTeSe_2$ have better bulk insulating properties due to the Fermi-level being situated near the middle of the bandgap [34,35]. Hence, we chose BTS for our study and performed all-optical pump and probe transient reflectance measurements to investigate the time scales of charge and spin relaxation. In this work, we used obliquely incident, circularly polarized mid-infrared/optical pump (7μm, 0.17 eV and 800 nm, 1.55 eV) to excite both below and above the bandgap (0.3 eV, [162]). The probe was fixed at 7 μm. This avoids probing of interband transitions and allows exclusive study of the photon helicity dependent dynamics of SS.

4.1 Experimental setup and sample preparation

A commercial ultrafast laser system (Coherent Legend) was used to generate 40 fs pulses at 5 kHz and 800 nm center wavelength. The beam was sent through an optical parametric amplifier (Light conversion) allowing generation of wavelengths from 1-14 μm (pulse duration of about 150 fs) through non-linear difference frequency generation. Wavelength of 7 μm was chosen to perform the experiment due to its sub-band gap energy, availability of polarizers and waveplates and good transmission of calcium fluoride (CaF_2) substrate. The 7 μm output from the optical parametric amplifier was divided using a CaF_2 beam splitter to obtain the pump and probe beam lines. The probe was sent through a delay stage with 13.3 fs resolution. Polarizer and waveplate was placed just before the focusing parabolic mirrors to obtain about 95% circularly polarized light. The parabolic mirrors focus the beam to a spot size of about 45 μm diameter. A liquid nitrogen cooled mercury-cadmium telluride detector was used to collect the probe beam. The alignment was carried out using a visible diode guide laser. The pump fluence was about 25 nJ/pulse and the probe fluence was about 5 nJ/pulse. A picture of the setup is shown in Figure 4.1.

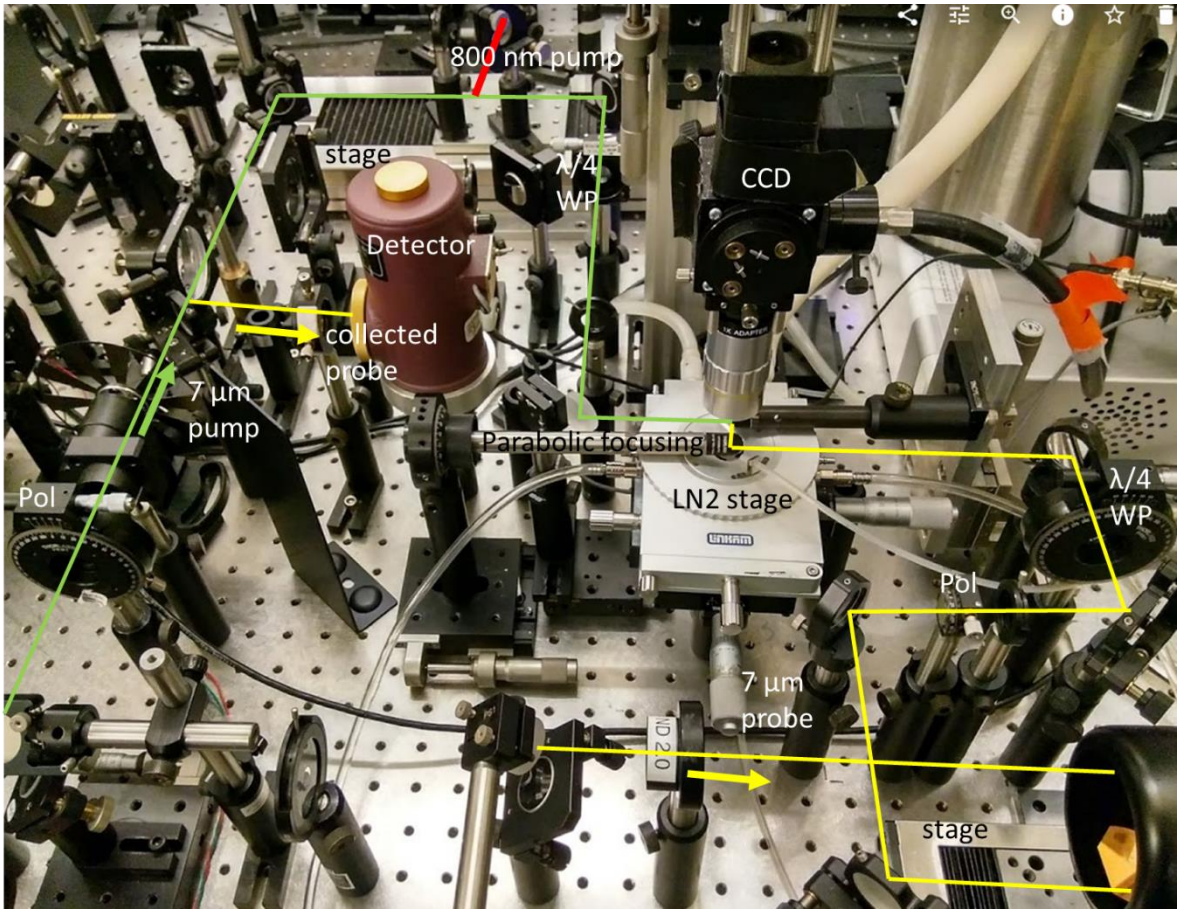

Figure 4.1: Experimental setup. λ/4 WP stands for quarter waveplate and Pol stands for polarizer.

The single crystals of Bi_2Te_2Se are grown by the Bridgman method by our collaborators Dr. Ireneusz Miotkowski and Prof. Yong Chen using a two-step procedure, provided here from reference [163]. In the first step, the raw material is synthesized from high purity elements in a two-zone horizontal furnace with independent temperature control. The starting materials, 6N (99.9999%) purity Bi, Te and Se, are deoxidized before use. Both Te and Se are purified further by multiple vacuum distillations under dynamic vacuum of 10^{-7} torr. The synthesis is made in vitreous carbon boats to avoid possible contamination from quartz. After the synthesis is completed at 900 ˚C, the pre-reacted charge is slowly cooled down under a controlled pressure of Se. The charge is then transferred into a carbonized quartz ampoule. The growth ampoule is placed in a vertical Bridgman three-zone furnace with independent temperature control. The linear gradient in the growth zone is set to 12 ˚C/cm. The radial gradient inside the growth zone is

symmetric and estimated to be less than 0.5 ˚C/cm. The typical speed for moving the ampoule through the temperature gradient is ~1 mm/hour.

Thick sections of BTS on Nitto tape were provided by Prof. Yong Chen. Nitto dicing tape were used to exfoliate thinner sections of the material from the original tape and subsequently further exfoliation (5-6 times) was performed to obtain thin flakes. A special thermal release tape (Nitto) is used to perform the final exfoliation. The peeling must be done rapidly to increase transfer yield and the tape pieces can be gently pressed together with cotton earbud tip to ensure good conformity. The thermal tape is then firmly adhered onto IR grade CaF_2 substrates (Eksma optics). The substrate and tape are heated to 135˚C on a hot plate, which results in the tape lifting off from the substrate, with an almost 100% transfer yield. Flakes in the range of 14 to 75 nm were obtained and a few were chosen based on area (comparable to beam spot size) and their thickness was measured using an AFM (AIST NT). The optical image, AFM image and AFM height profile for four flakes used in this study are shown in Figure 4.2.

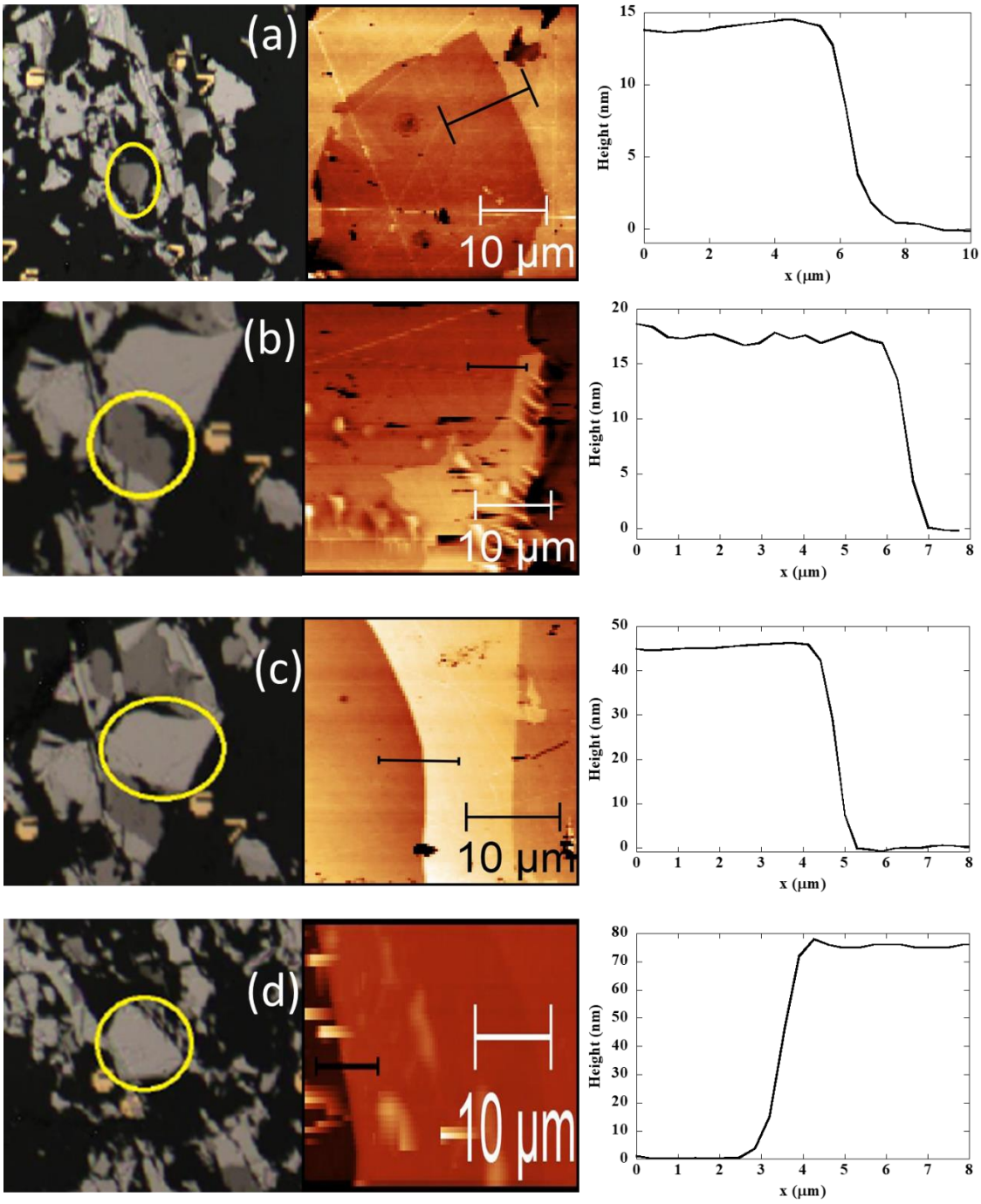

Figure 4.2: From left to right in each panel shows the optical image, AFM image and height profile of (a) 14 nm (b) 18nm (c) 45 nm and (d) 75 nm flake.

The samples were placed in a dark vacuum box to avoid contamination or oxidation. Nitrogen gas was flown over the samples during the experiment. All flakes were confirmed to be

Bi_2Te_2Se by Raman spectroscopy (Horiba LabRAM), and a typical spectrum is shown in Figure 4.3.

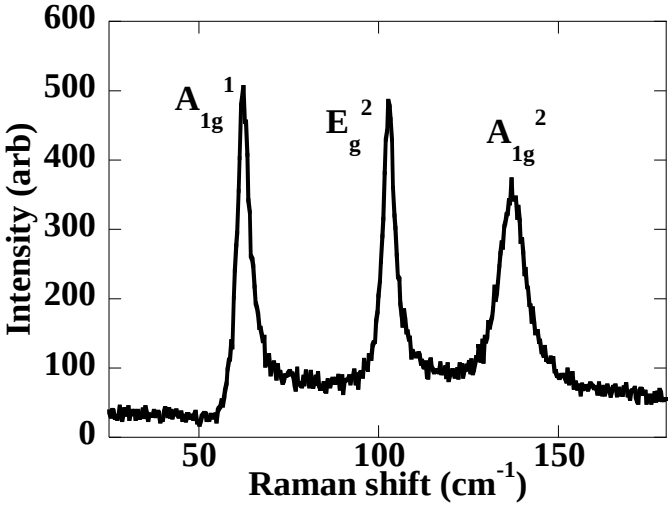

Figure 4.3: Typical Raman spectrum of BTS

4.2 Results for sub-band gap and above band-gap excitation

We first examine transient dynamics with both excitation and probing energies of 0.17 eV (7 μm). Flakes of BTS with thicknesses between 14 and 75 nm were exfoliated on CaF_2. Figure 4.4 shows the helicity and thickness dependent dynamics in these samples at room temperature. ΔR is the change in reflectance of the probe after pump excitation, i.e. $\Delta R = R_{pump} - R$, where R_{pump} and R are the reflectance with and without pump. LL (left circular pump, left circular probe) corresponds to pump and probe having angular momentum pointing in the same direction with respect to the sample surface and RL (right circular pump, left circular probe) corresponds to their angular momentum in opposite directions. A clear difference between RL and LL lasting for more than 10 ps is observed for 14 and 18 nm samples (Figure 4.4a and 4.4b). When the pump and probe have the same helicity, we observe a larger signal amplitude - LL has a larger amplitude than RL.

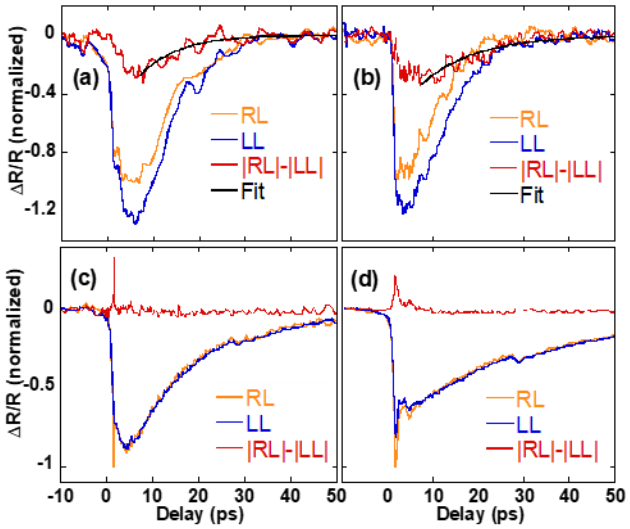

Figure 4.4: Helicity dependent dynamics for (a) 14 nm (b) 18 nm (c) 45 nm (d) 75 nm flake with 7 μm pump and 7 μm probe. The difference, i.e. |RL|-|LL| vs time, can be fit with an exponential decay time τ = 8.2 ps for (a) and τ = 12 ps for (b).

ΔR/R of both RL and LL are normalized to $|RL|_{max}$. The difference between LL and RL is also plotted as |RL|-|LL|. Furthermore, an exponential fit ($e^{\frac{-t}{\tau}}$) can be used to describe the decay of the difference, starting from the point of maximum change. The extracted decay time (τ = 8.2 ps and τ = 12 ps in Figure 4.4a and 4.4b) quantifies spin relaxation due to the branch selective excitations which will be discussed later. The same trend is observed when changing the helicity of the probe instead of the pump - RR shows a larger signal than RL, as shown in Figure 4.5.

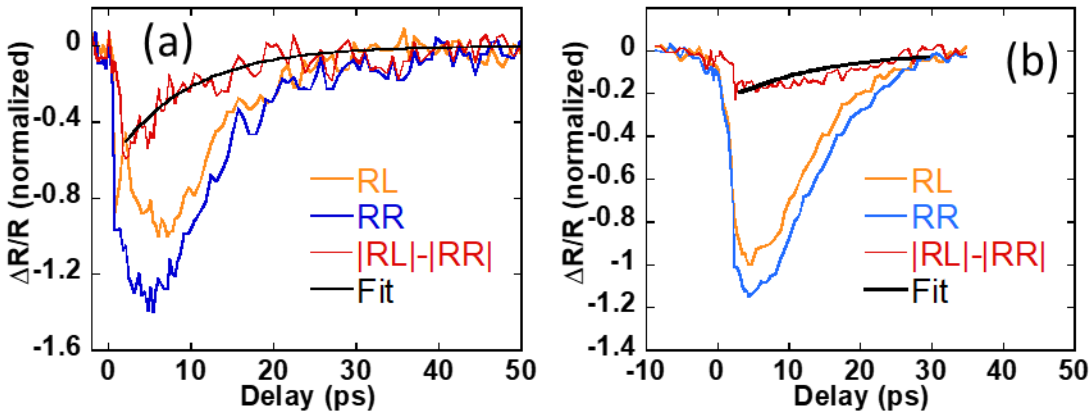

Figure 4.5: Changing the probe polarization instead of the pump polarization also leads to the same result, i.e. for the (a) 14 nm flake and (b) 18 nm flake, the RR case has larger amplitude, which is symmetric with the LL case having larger amplitude as in Figure 4.4. The difference decay time constant from the fit is 9.1 ps for (a) and 13 ps for (b).

The measurement was also conducted at 80 K, as shown in Figure 4.6, but only a slightly greater difference between the RL and LL signals was observed.

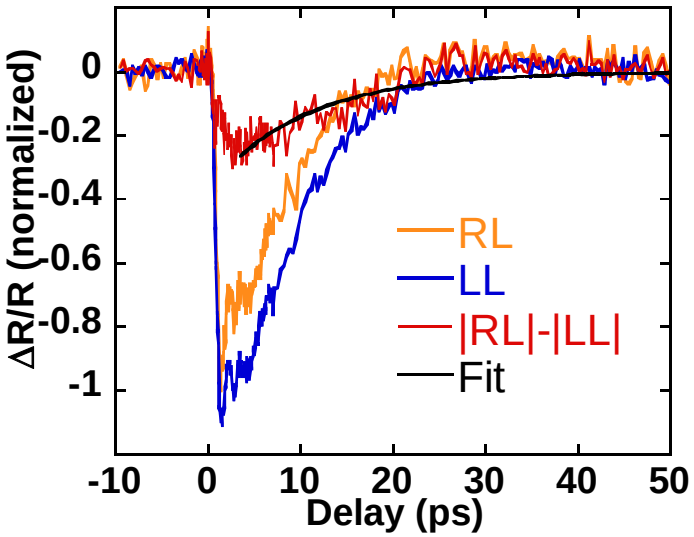

Figure 4.6: Probing 18 nm flake at 80 K resulted in similar relaxation dynamics as the room temperature case. The difference decay time constant is 13.8 ps

For thicker samples (Figure 4.4c and 4.4d), only a short lived difference between the reflectance signals RL and LL is observed around time zero. Its possible origin could be coherent

coupling of pump and probe during their temporal overlap and hence is not related to SS dynamics. The small bump near 30 ps is due to multiple reflection by the neutral density filter.

The decay time of the reflectivity signal quantifies charge relaxation. The charge decay times for 14 and 18 nm flakes are similar to the values reported for SS relaxation in ARPES studies [147,148], indicating the dynamics observed in the thin flakes is dominated by SS. Theoretically it has been predicted that charge and spin relaxation times should be the same on the Dirac cone of TI [164]. From the experimental data, we see that the time duration when LL and RL are different, which indicates the spin decay time, is the same as the total decay time of the reflectivity signal. Hence, the dynamics is completely dominated by SS in thin flakes. We also noticed the decay dynamics of thin flakes are similar to that of graphene, whose dynamics has a Dirac origin. Figure 4.7 shows similar charge decay times for the 14 nm flake and graphene, suggesting a Dirac origin for the BTS flakes. The pump and probe were both 7 μm. CVD grown monolayer graphene was transferred onto CaF_2 substrate by Andres Llascahuanga.

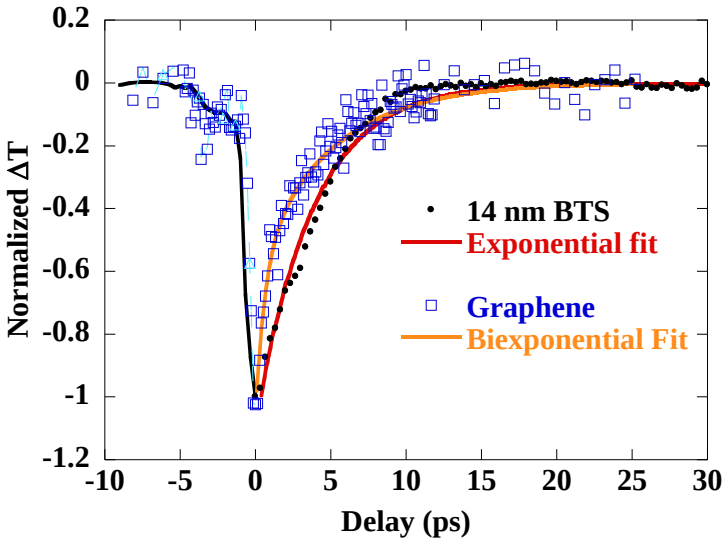

Figure 4.7: Comparison of 14 nm flake with graphene. The decay can be described with an (bi)exponential fit ($\tau 1 = 0.6$, $\tau 2 = 5$ ps for graphene and $\tau = 4.1$ ps for BTS). The measurement was done in transmission mode with higher pump fluence to extract measurable sign from graphene.

The slower charge decay as the flakes get thicker is related to atmospheric doping of the samples due to gas adsorption that raises the fermi level [163,165–168], leading to allowed SS to bulk conduction band transitions and excitations of free carriers. The slow relaxation is thus due

to the interband relaxation from the conduction band to SS/valence band, requiring additional scattering mechanisms such as phonon coupling or defect assisted recombination as observed by other researchers [158]. It is reported that bulk samples undergo short term atmospheric doping [167,168] and hence those flakes were likely to have been doped shortly after exfoliation. For our samples, electrical and thermal transport measurements on thin BTS films (< 20 nm) have shown dominating contribution of SS to thermal and electrical conductivity at room temperature as compared to thicker flakes (> 20 nm) [36].

To further investigate into the assumptions of doping, Hall measurements were carried out on flakes with varying thickness by Dr. Jifa Tian. The carrier concentration with thickness is shown in Figure 4.8. The drastically lower concentration is an indication of reduced band bending at the surface for thin flakes.

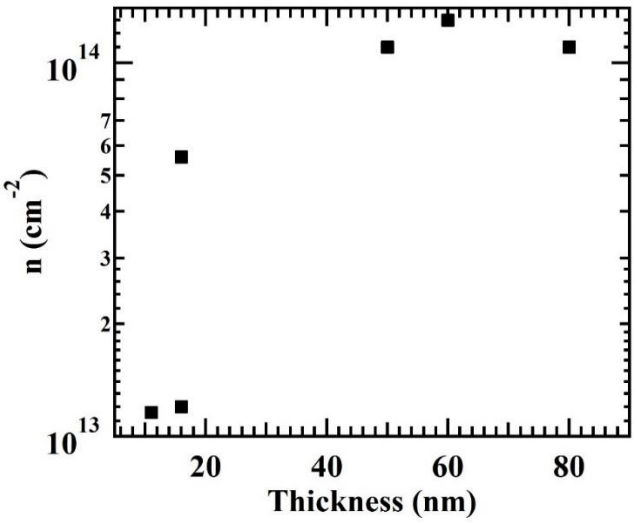

Figure 4.8: Thickness dependent carrier concentration extracted from Hall measurements. Samples thinner than 18 nm show an order of magnitude lower carrier concentration compared to thicker samples.

An optical image and atomic force microscope scan of the sample in Hall bar geometry is provided in Figure 4.9.

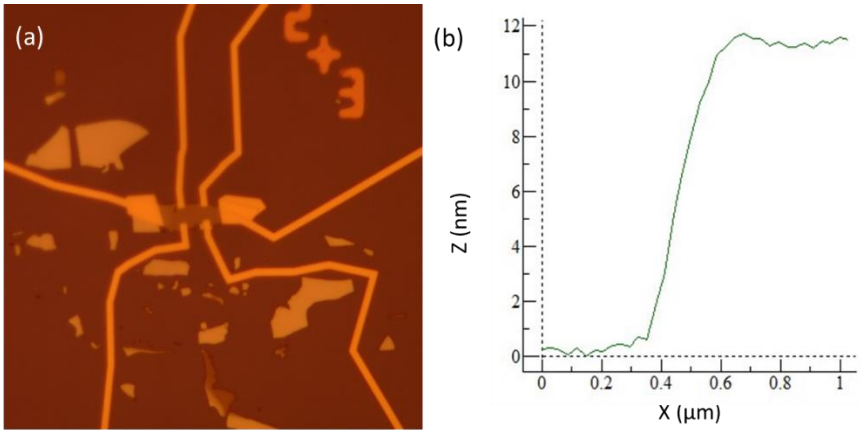

Figure 4.9: The BTS flakes were patterned into a Hall bar geometry for carrier concentration measurements, where (a) shows the optical image of the device and (b) shows the AFM scan of the flake edge with height 11 nm.

The device resistance as a function of magnetic field is shown in Figure 4.10, wherein R_{xy} is fit to obtain carrier concentration *n* following these steps [1]:

$$R_{xy} = \frac{R_H * B}{t} \ [\Omega] \tag{4-1}$$

where R_H is the Hall coefficient, R_{xy} is the transverse Hall resistance, *t* is the thickness, and *B* is the out-of-plane magnetic field. R_H can be expressed as:

$$R_H = -\frac{1}{ne} \ [\mathrm{m^3/A/s}] \tag{4-2}$$

where *n* is the carrier concentration and *e* is the electron charge. Hence,

$$n * t = {}^{-1}/_{(e * slope)} \ [\mathrm{m^{-2}}] \tag{4-3}$$

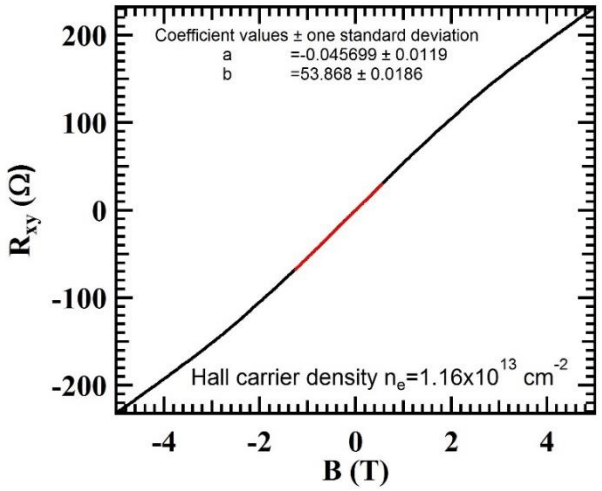

Figure 4.10: Transverse Hall resistance, Rxy as a function of magnetic field B. A linear fit can be used to extract the Hall carrier concentration. Coefficients a and b are the intercept and slope respectively.

The obtained 2D carrier densities of the thin samples from R_H is about 1.0×10^{13} cm^{-2} (5×10^{12} cm^{-2} for one surface). From the ARPES results on bulk samples [163], it was found that Fermi level is located near the conduction band edge, and the carrier density on one surface is ~1.0×10^{13} cm^{-2}, which is two times higher than the carrier density (5×10^{12} cm^{-2} for one surface) obtained from our thin samples. Therefore, the Fermi-level in our thin samples is located closer to the charge neutral point. A more comprehensive set of data and discussion are provided in our previous work [36].

Se vacancy migration to the surface and subsequent gas adsorption has been reported as a mechanism for surface doping [169,170]. Thicker films have many quintuple layers behind their surface allowing for vacancy migration and formation of 2D electron gas and subsequent band bending at the surface. Thin flakes on the other hand have fewer migrating sites due to the thinner bulk region and hence do not undergo as much of the surface doping.

We now proceed to explain the helicity dependent dynamics using the band structure (E vs *k*) in Figure 4.11a, which depicts the Fermi-level at 148 meV above the Dirac point as observed in ARPES measurement for freshly cleaved sample in vacuum, not affected by atmospheric doping [163]. RL implies σ+ pump and σ- probe having angular momentum +1 and -1, respectively. We set the spin on the right side branch of SS +1/2 and on the left side -1/2. Hence the in-plane component of a circularly polarized pump (black arrow) at an oblique incidence

excites only the depicted transition due to conservation of in-plane angular momentum. For example, the σ+ pump excites electrons in the valence band with -1/2 spin into the +1/2 branch of the Dirac cone, whereas excitation into the -1/2 branch is forbidden. Likewise, the circularly polarized probe (orange arrow) at an oblique incidence monitors only the depicted transition. The mid-infrared pump pulses excite electrons from the valence band to the energy levels around the Fermi-energy. In principal, transition from SS to conduction band is also possible. However, the large pool of valence electrons transitioning to SS competes with the SS to conduction band transition, making the latter less probable. The probe, being of the same energy, monitors only SS. Therefore, when probing with the same helicity, the change in reflectance is expected to be larger because $\Delta R \sim \Delta f_1 * \Delta f_2$, where $f_1(k)$ and $f_2(k)$ are momentum dependent Fermi occupation probabilities of the initial and final states. The holes generated in the valence band rapidly (<100 fs) redistribute in k-space making f_1 momentum independent whereas the asymmetrically generated electrons in SS do not redistribute as fast due to the back-scattering protection, making f_2 larger for pumping side of the k-space. Hence the difference in the signals (RL-LL) gives the back-scattering time, which is a net result of many small angle scattering events, and will be discussed in more details later. The difference between the RL and LL in the thin flakes is about 20% of the signal amplitude, which is due to the out-of-plane component of the pump and probe that excite both branches of the Dirac cone simultaneously, giving rise to at least half of the total signal amplitude.

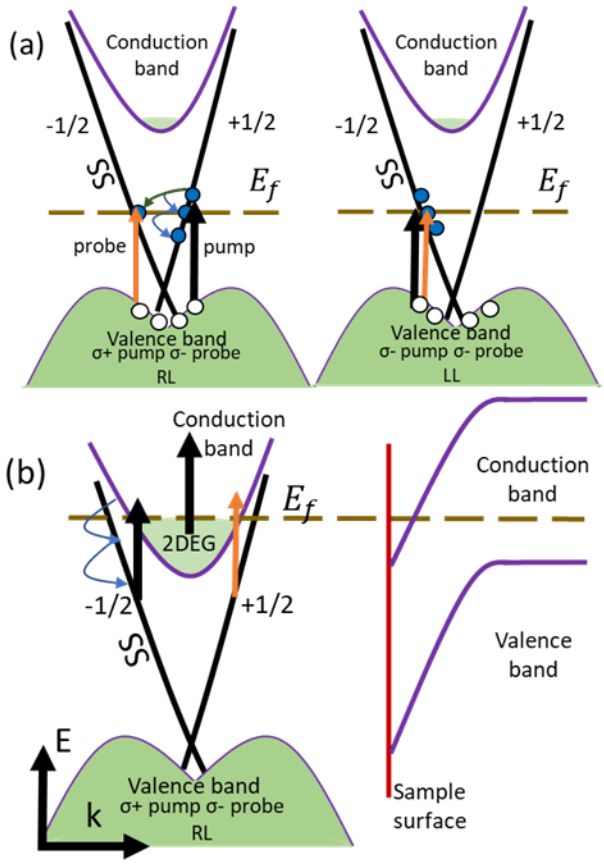

Figure 4.11: Transition diagram with 7 μm pump and 7 μm probe for (a) thin samples with relatively low Fermi-level. The left figure illustrates σ+ pump and σ- probe (RL), and the right figure σ- pump and σ- probe (LL). LL produces a stronger probe response than RL. (b) Thick samples with high Fermi-level for σ+ pump and σ- probe (RL), which does not produce a helicity dependent signal (see text). The black arrow represents the pump and the orange arrow represents the probe.

For thicker flakes, the Fermi-level is raised (inversely, band is bent) as depicted in Figure 4.11b [163]. The SS to conduction band excitation is now possible which leads to interband relaxation and manifests as a slower decay in the signals. An important consideration is the hexagonal warping of the higher energy surface states lying closer to the conduction band, resulting in out-of-plane spin components on an otherwise in-plane spin texture carried by the SS [171–174]. This could be one of the main reasons for the lack of clear helicity dependence in thick flakes owing to excitation of the higher energy portion of the SS. The excitation of 2D gas electrons or defect states is another reason as they do not have a helicity dependence.

We now examine above bandgap excitation. Figure 4.12 shows flakes of all thicknesses exhibit a helicity dependence, but with reducing magnitude of the difference (|RL|-|LL|) as the

flakes become thicker. The difference can be once again fit with an exponential. For the 14 nm flake (Figure 4.12a), the total signal decays rapidly, with a spin relaxation time (the time when RL and LL is different) of 2.8 ps, same as the total signal decay time. The spin relaxation is hence limited by the charge relaxation itself, similar to what is observed with below bandgap excitation (Figure 4.4a). It is known that excitation/probing close to the Fermi-level shows a slower decay than excitations away from it due to the requirement of phonons for relaxation [56,175]. This is in good agreement with our observed timescales, since the 800 nm light can excite carriers much above the Fermi-level within the Dirac state, whereas the 7 μm excites carriers in close proximity to the Fermi-level. Here again LL has a larger signal than RL and can be explained using the transition diagram, Figure 4.13a, where electrons are promoted to states near the Fermi-level from deeper lying levels in the valence band. The sharp peak near time zero has been truncated for easier visualization.

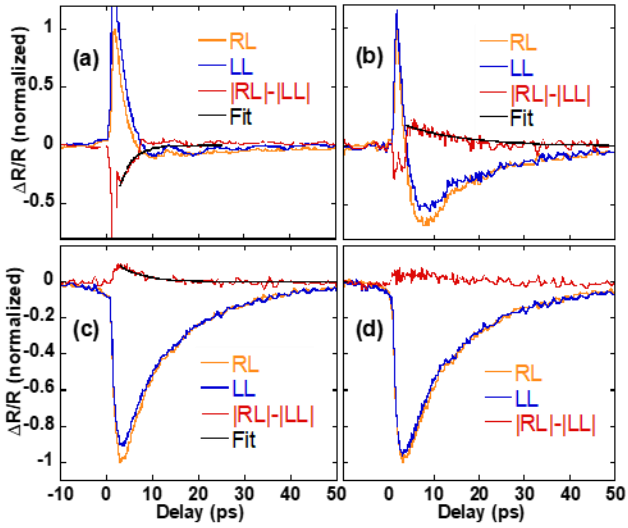

Figure 4.12: Helicity dependence of (a) 14 nm (b) 18 nm (c) 45 nm and (d) 75 nm sample with 800 nm pump and 7 μm probe. The difference, |RL|-|LL|, is fit with an exponential, τ = 2.8 ps for (a), τ = 12.5 ps for the positive part in (b), and τ = 5.3 ps for (c). The fitting is poor for (d) and hence not shown.

Helicity dependence is also observed for the thicker flakes as shown in Figure 4.12c and Figure 4.12d, which was absent with the 7 μm pump. This is because 800 nm pump can excite almost all energy levels on SS, unlike the 7 μm pump, as illustrated in the transition diagram Figure 4.13b. Moreover, the RL case has a larger signal amplitude, whereas in the 7 μm and 800 nm case

for thin flakes, the LL combination has a larger amplitude. This can be explained based on Figure 4.13b. The allowed excitation for 800 nm pump is reversed when the Fermi-level is higher, because the initial state is now SS instead of the valence band. For example, a σ+ pump must excite electrons from the -1/2 branch of SS and result in +1/2 spin electrons in the conduction band (Δ = ½-(-½) = 1). This means electrons from the left side (-1/2) branch are preferentially depopulated by the right circular (σ+) pump, but the left circular probe (σ-) interrogates the left branch, thereby giving a larger signal magnitude. The obtained spin relaxation time is 5.3 ps for the 45 nm sample, but a spin relaxation time is not obtained for the 75 nm sample due to the very low differential signal. It is also not surprising to observe a charge decay time of close to 50 ps, which is similar to that for thick samples when pumped with 7 μm light. This leads us to the conclusion that the bulk states continuously feed the surface states and relax via this channel as observed in literature [145,156].

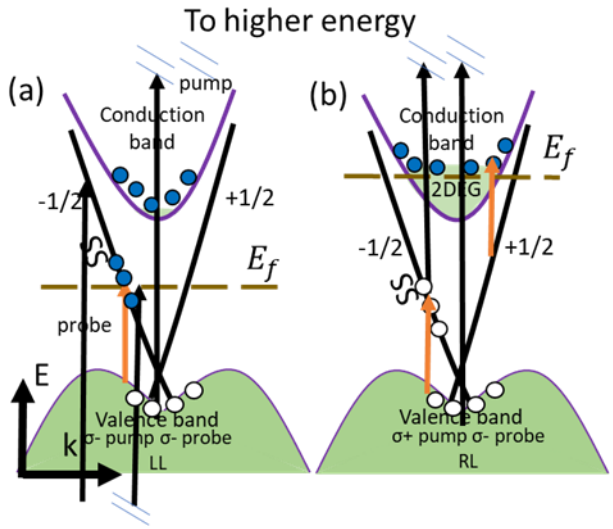

Figure 4.13: Transition diagram for 800 nm pump and 7 μm probe for (a) thin samples with low Fermi-level for σ- pump and σ- probe (LL), resulting in a stronger probe response for LL, (b) thick samples with high Fermi-level, where RL has a stronger probe response (see text). The black arrow is the pump and orange arrow is the probe.

We now examine the data of the 18 nm flake, Figure 4.12b. We see that it shows features possessed by both 14 nm and 45/75 nm flakes, i.e. a negative and positive difference between RL and LL (τ = 12.5 ps). This, along with the diminishing difference (|RL|-|LL|, Figure 4.12a-d) with thickness is an indicator of enhanced surface to bulk coupling as the flakes get thicker. A rapid

flow of electrons and holes from the deeper layers towards the surface and subsequent relaxation through the Dirac states is a possible mechanism that reconciles the observation. That is, the influx of unpolarized carriers would diminish the difference signal and at the same time those carriers would account for interband relaxation, which leads to slower relaxation. The 18 nm flake shows similar spin-relaxation timescale with 7 μm and 800 nm excitation because the expected faster relaxation (e.g. 14 nm flake) is offset by the bulk contribution in the latter case, prolonging the carrier lifetime. The influx of carriers could also explain the faster spin relaxation in the 45 nm flake (5.3 ps).

Another important perspective regarding the thickness dependent spin and charge dynamics is small angle scattering of electrons due to phonons. Surface state electrons in 3D topological insulators are only forbidden from 180˚ backscattering in the k-space, but can undergo small angle scattering [131]. SS electrons in the very thin samples have little access to scattering with bulk phonons, resulting in reduced small angle scattering, and thus competing charge and spin relaxation is observed in our experiments (Figure 4.4a, Figure 4.4b, Figure 4.12a). In contrast, thick samples can supply phonons and allow for faster decoherence of the SS electrons. This mechanism is in parallel to the influx of unpolarized carriers discussed previously.

Topologically protected metallic surface states have been experimentally shown to have long mean free paths for charge and spin diffusion which could be as much as 2 μm [176–178]. A few pure metals have also been reported to have spin diffusion lengths of 100 nm or more [179]. With an asymmetry lasting more than 10 ps and a fermi velocity of $1x10^5$ m/s [163], we can estimate a spin diffusion length of longer than 1μm in our samples. This is in reasonable agreement with aforementioned literature, especially for doping compensated materials. A perfectly tuned Fermi-level in BTS shows SS population lasting as long as 6 μs [180,181]. Hence, along with a long spin-diffusion length, BTS can be promising for spintronics if its Fermi-level is well tuned and defects and vacancies reduced. Also, spin relaxation times obtained in this work are comparable to valley depolarization times of few picoseconds observed in valley non-degenerate transition metal dichalcogenides (TMDs) such as MoS_2, $MoSe_2$ and WS_2 [182–184]. However, due to the massless nature of the Dirac like fermions in TIs, we can expect them to perform comparable to or better than TMDs in spintronics.

4.3 Study of laser induced coherent oscillations in Bi_2Te_2Se

Previous studies on topological insulators such as Bi_2Se_3 and Bi_2Te_3 has revealed femtosecond laser induced coherent optical and acoustic phonon, with oscillation periods ranging from 300 fs upto 10s of picoseconds [79,185,186]. Study of phonon dynamics is important for potential use in high frequency acoustic transducers and to better understand electron-phonon interactions. Electrons excited to high temperatures by the ultrafast laser pulse rapidly dissipate their energy to the lattice which leads to localized stress generation due to higher lattice temperature. This leads to strain and subsequently manifests as coherent oscillations that travel longitudinally into the sample, originating from the surface (absorption depth of the laser). Several models such as impulsive stimulated Raman scattering, displacive excitation of coherent phonon, impulsive stimulated Brillouin Scattering, laser induced thermo-modulation etc have been used to describe these processes. Studies involving more fundamental approaches such as molecular dynamics simulation have also been carried out [187].

Most studies have focused on generation of bulk phonon modes such as A_{1g} mode, which are quite strongly observed in Raman spectroscopy as well. Some of the recent Raman studies have shown that there exist surface phonon modes which are accessible at low temperatures such as shown in Figure 4.14 [188].

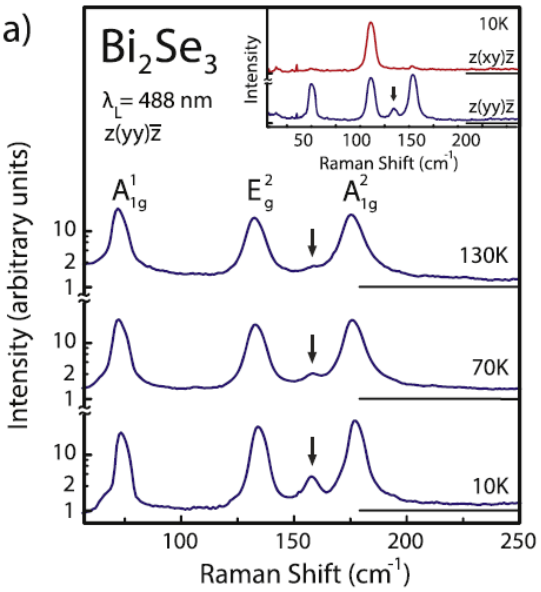

Figure 4.14: Appearance of surface phonon (shown by black arrow) at low temperature in Bi_2Se_3 [188].

We carried out a similar study at low temperature for Bi_2Te_2Se, but could not observe appearance of surface modes, which was expected between 100 and 150 cm^{-1}. The low temperature Raman signals at 10 K are shown in Figure 4.15. The measurement was performed by Andres Llacsahuanga in Prof. Yong Chen's low temperature facility.

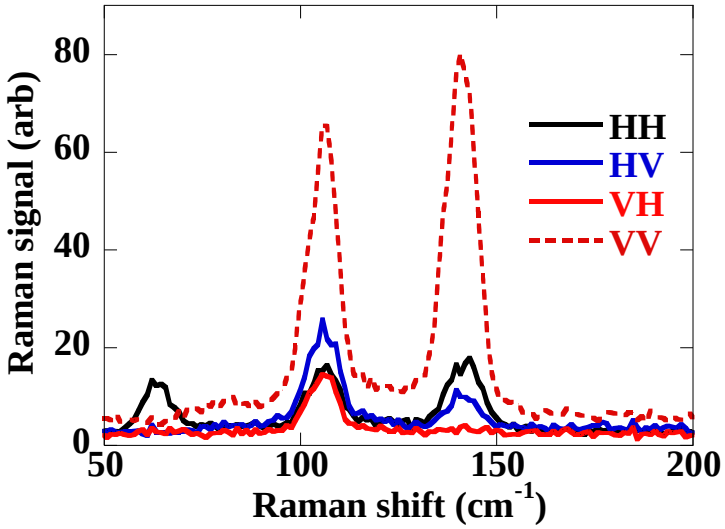

Figure 4.15: Low temperature (10K) Raman shift in Bi_2Te_2Se for various combinations of polarizer and analyzer.

We proceed to carry out the pump-probe experiments to study the coherent phonon oscillations, an example of which is shown for 260 nm BTS flake in Figure 4.15. The material shows strong A_{1g} coherent phonon oscillations. This measurement was carried out with 800 nm pump and probe.

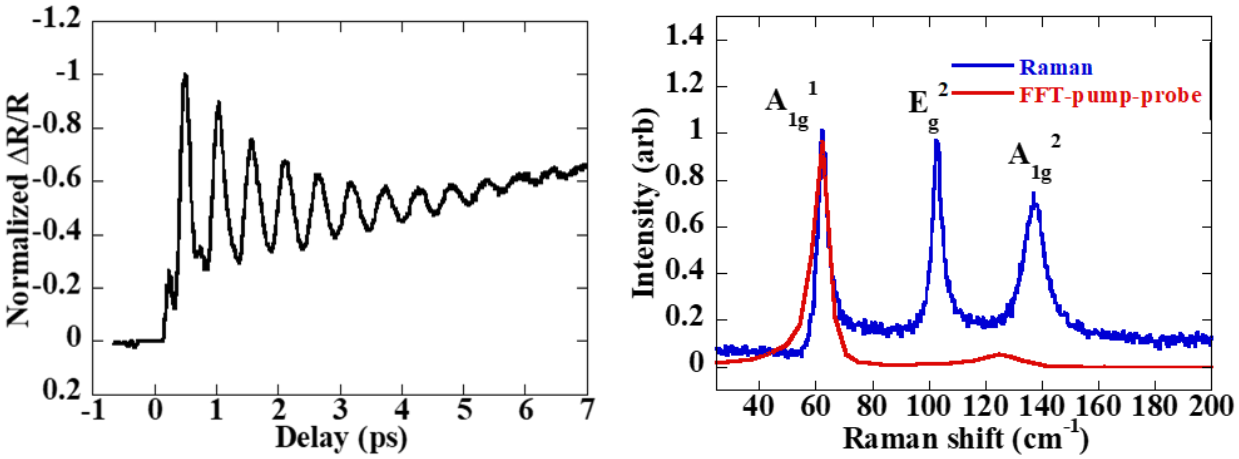

Figure 4.16: Coherent phonon oscillation in BTS (left). Fourier transform of the signal after applying a second order Butterworth bandpass filter to reject the non-oscillating components (right). The oscillation corresponds to the A_{1g} optical phonon by comparison with Raman spectrum.

The experimental microscopy setup (Figure 4.17) can be used to study flakes as small as 2 μm in size. The pulse duration should be much shorter than the phonon oscillation period to ensure that coherent phonons can be excited. The autocorrelation of the pump-probe pulses is shown in Figure 4.18. A pulse duration of 100 fs could be obtained.

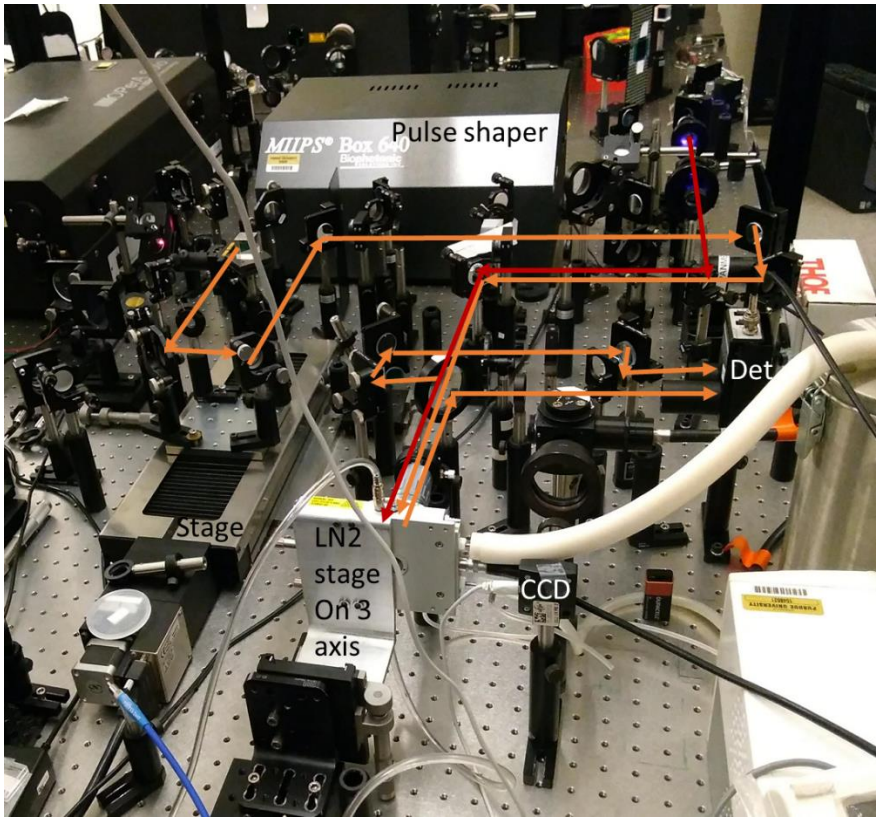

Figure 4.17: Experimental setup for coherent phonon study. A pulse shaper can be used to independently control the pulse shape if necessary. The sample can be cooled to 80 K in the cryogenic stage.

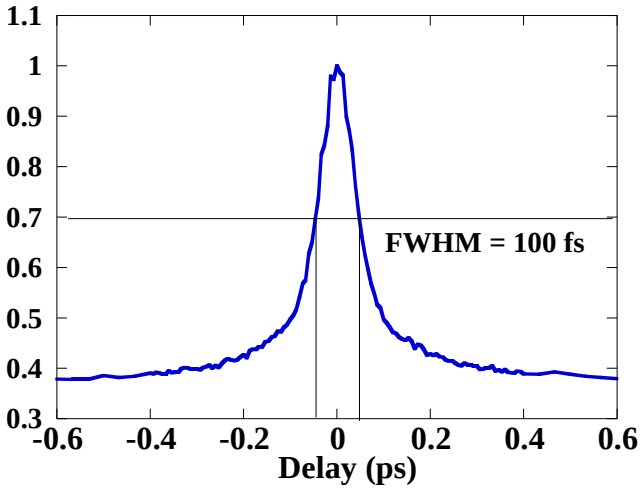

Figure 4.18: Autocorrelation of 800 nm pump and probe pulses showing pulse duration of 100 fs.

Furthermore, the thickness dependence of the phonon oscillations was studied, which revealed that coherent phonons are not excited in thinner flakes, as shown in Figure 4.19. Moreover, the amplitude of the signal increased, indicating that the deposited energy is retained in the electron population and not transferred to the phonons.

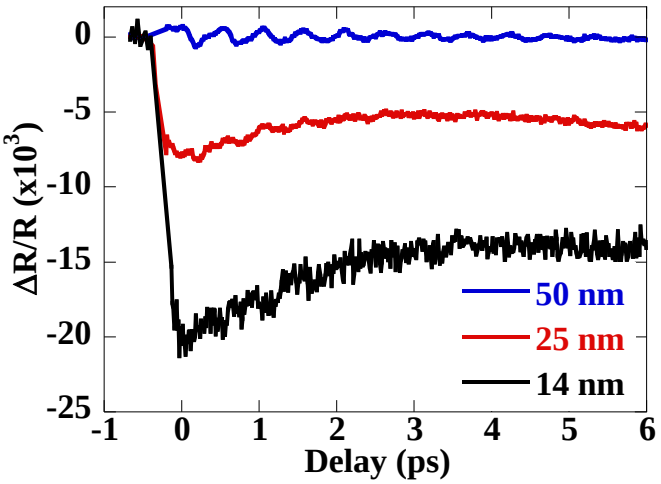

Figure 4.19: Thickness dependent coherent phonon oscillations in BTS. The amplitude of the signal increases for thinner samples with decreasing oscillatory component.

4.4 Summary

In summary, we have carried out oblique incidence, helicity resolved optical pump-probe spectroscopy on topological insulator Bi_2Te_2Se using below/above band gap excitation and shown that this technique is a useful tool to study spin relaxation dynamics in topological insulators. With below bandgap excitation, a clear helicity dependence was observed for flakes thinner than 20 nm. The vanishing helicity dependence in thick samples was attributed to formation of 2D electron gas on the surface of the material due to gas adsorption at vacancy sites. Above bandgap excitation resulted in asymmetric excitation of surface states for both thin and thick samples. The polarization resolved dynamics reveals the helical spin texture of the surface states and spin relaxation times in the 5-15 ps range, which translates to μm range spin diffusion length. Excitations with mid-infrared circularly polarized light is therefore a possible route to control spintronic devices involving thin film topological insulators.

5. MAGENETO OPTIC EFFECTS AND SPATIALLY RESOLVED ULTRAFAST DYNAMICS

Magneto-optic effect, as the name suggests, is the result of the interaction between a magnetically polarized material and light. During the early development of the electromagnetic field theory, magneto-optic effects played an important role to provide experimental evidence for the electromagnetic nature of light. In the 19th century, Michael Faraday observed that the polarization of a linearly polarized light rotates as it passes through a material placed in a magnetic field that is parallel to the direction of propagation. This was the first demonstration of the effect of magnetic field on light. Subsequently, a counterpart of the Faraday effect, the Magneto-optic Kerr effect (MOKE) was discovered, wherein the polarization of light reflected from a magnetically polarized medium is rotated. In modern times, crystals possessing strong magneto-optic properties are used as optical isolators (Faraday isolator) and for optical data storage and mode conversion waveguides [189]. Furthermore, MOKE is a sensitive technique to optically determine the magnetic state of thin films. To address the need for faster data storage devices, we propose optical control of magnetization through coupling of ferromagnetic thin-films with topological insulators. As discussed in the previous chapter, circularly polarized light can generate spin population on the surface of topological insulators. This photo-generated spin can be potentially transferred to a ferromagnet by placing it in physical contact with the TI. The spin transfer can result in magnetization switching and has been demonstrated in literature for electrically injected spin [190]. The first part of this chapter will describe the principle of MOKE and experimental setup to study magnetization state of thin films, both with CW and ultrafast laser. All optical switching and detection of ferromagnetic thin films via spin-transfer torque from topological insulators will be discussed subsequently.

The second part of the chapter deals with spatially resolved ultrafast dynamics to enable the study of the carrier diffusion and extract transport properties such as diffusion coefficient and mobility [191]. Time resolved measurements discussed previously enable indirect estimates of transport properties through scattering and electron-phonon interaction lifetimes, whereas spatially resolved studies provide a more direct visualization of the photoexcited carrier transport. Moreover, ultrafast scanning microscopy can also reveal exciton transport properties and charge transport across grain boundaries [192,193]. Recently, it was shown that early stage hot carrier diffusion

can be spatially resolved with this technique, providing valuable information about electron thermal conductivity independently from phonon thermal conductivity [194]. To explore this dimension of ultrafast dynamics, the newly built experimental setup with laser scanning capability along with preliminary results will be presented.

5.1 Magneto Optic Kerr Effect

In its simplest form, the magneto-optic Kerr effect results in the rotation of polarization of linearly polarized light as it reflects from a magnetically polarized medium. Electrons in the medium oscillate at the frequency of the incident electric field (light field) and hence possess velocities along the direction of the field polarization. When a magnetic field is present inside the medium, the electrons experience a Lorentz force given by $F_{lorentz} = q * v \times B$, where q is the charge of the electron, v is the electron velocity and B is the magnetic field inside the medium. Because of the cross product, the force is perpendicular to the direction of the initial velocity. Hence the electron picks up another component of velocity. Since the reflected light is a result of the light emission from the oscillating electrons, the reflected light possess a perpendicular component of polarization, leading to a rotation. Depending on the incidence plane and the direction of the magnetic field inside the medium, MOKE is classified into three categories [195]:

1. Polar MOKE: $\vec{m} \parallel \vec{n}$, and $\vec{m} \parallel plane$

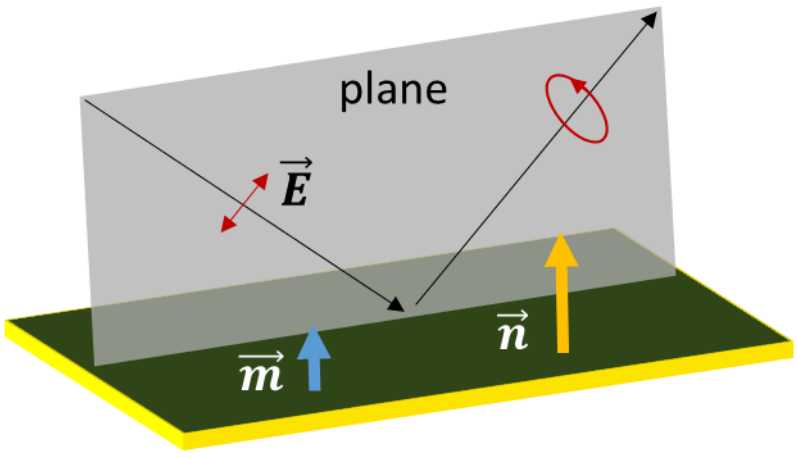

Figure 5.1: Polar MOKE geometry showing material magnetization $\vec{m}$, surface normal $\vec{n}$ and plane of incidence. The light can be incident normal to the surface or at an angle and can be *s* or *p* polarized. The reflected light is elliptically polarized.

2. Longitudinal MOKE: $\vec{m} \perp \vec{n}$, and $\vec{m} \parallel plane$

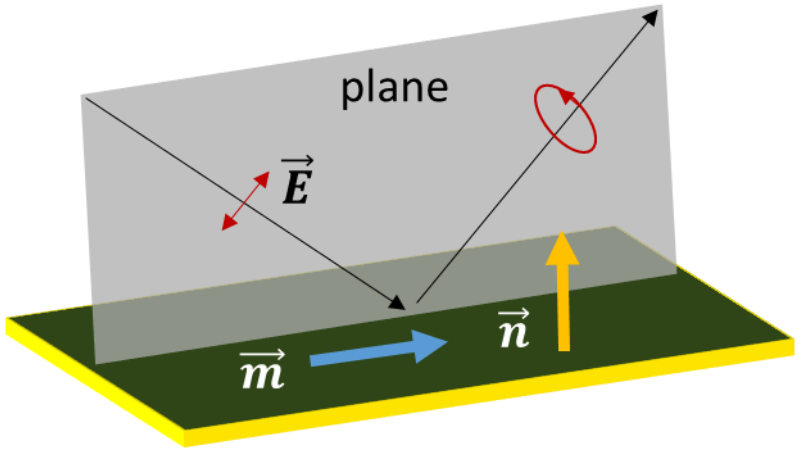

Figure 5.2: Longitudinal MOKE geometry showing material magnetization $\vec{m}$, surface normal $\vec{n}$ and plane of incidence. The light can only be obliquely incident on the surface and can be *s* or *p* polarized. The reflected light is elliptically polarized.

3. Transverse MOKE: $\vec{m} \perp \vec{n}$, and $\vec{m} \perp plane$

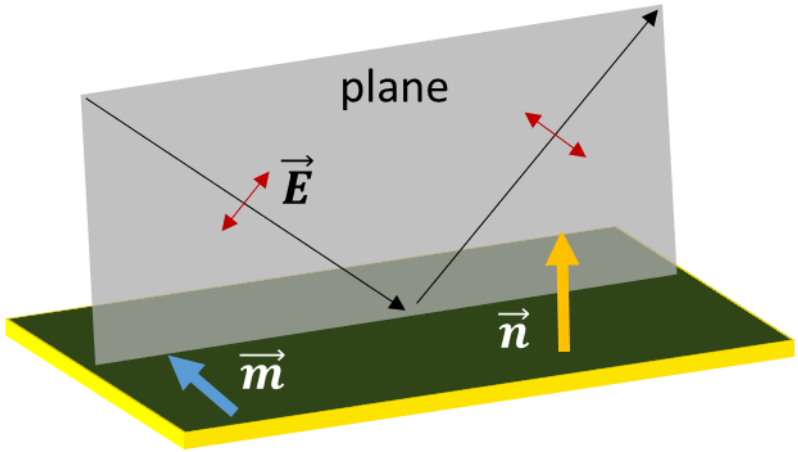

Figure 5.3: Transverse MOKE geometry showing material magnetization $\vec{m}$, surface normal $\vec{n}$ and plane of incidence. The light can only be obliquely incident on the surface and can only be *p* polarized. Note that the output polarization is also linear, unlike the previous cases and the detection is based on the change in reflected intensity.

5.1.1 Kerr Rotation and Ellipticity

The degree of polarization rotation can be quantitatively expressed in terms of Kerr rotation angle and Kerr ellipticity. The process of polarization rotation is illustrated in Figure 5.4 for polar MOKE geometry.

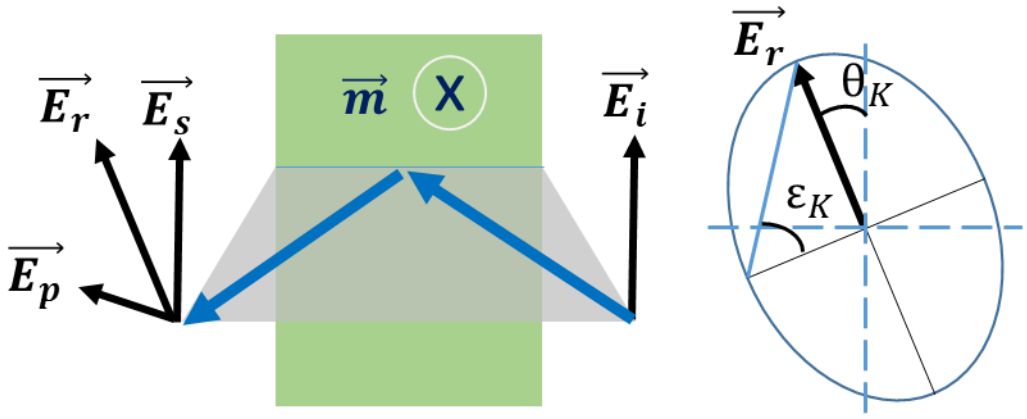

Figure 5.4: *p* polarized light produced from *s* polarized input due to polar MOKE (left). The magnetization $\vec{m}$ points into the page. The output polarization is typically elliptical with the ellipse tilt θ_K and ellipticity ε_K that depend on the magnitude and phase of the *p* polarized component (right).

5.2 MOKE Setup

As discussed in the previous section, the Kerr angle and ellipticity depends on the phase and magnitude of the Kerr generated perpendicular polarization. This in turn depends on the magnetization $\vec{m}$ of the sample, which can be controlled by applying an external magnetic field. For this purpose an electro-magnet is used which can generate upto 800 Oe field. The electro-magnet is a circular coil with a cylindrical opening in the center. The field strength measured with a Gauss meter at 10 V bias as a function distance from the edge, along the center line of the coil, is shown in Figure 5.5.

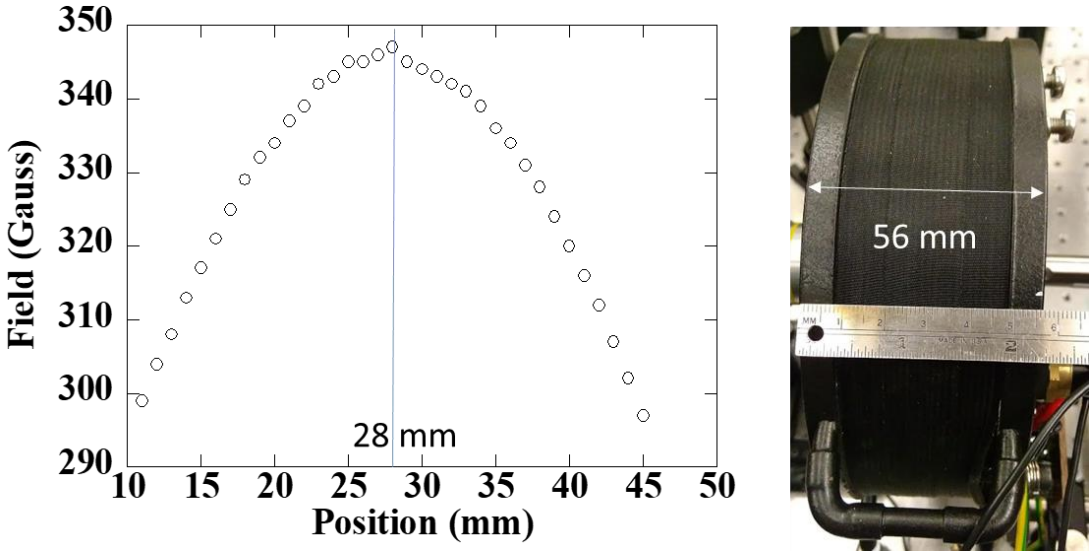

Figure 5.5: Spatial calibration of electro-magnet. Field vs position at 10 V bias along the center line (left) and image of electromagnet coil with dimensions (right).

A unipolar power source (Hewlett Packard) operating upto 20 V and 6 A is used to vary the field. A manual switch is used to reverse the direction of the field. For low-field, automated bi-polar operation, a Keithley voltage source is used, producing upto 4V and 1 A. The field at the center of the coil as a function of voltage is shown in Figure 5.6.

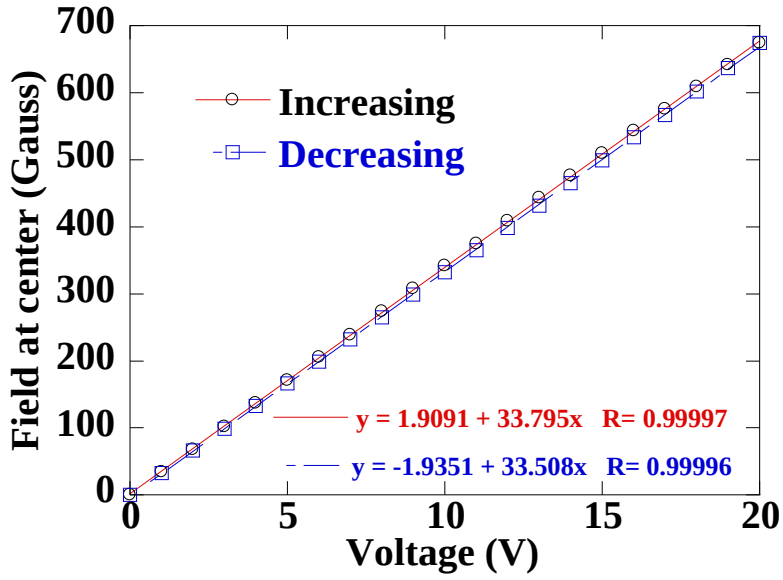

Figure 5.6: Field vs voltage calibration of magnet. No significant hysteresis is observed.

A schematic of the setup is shown in Figure 5.7. The laser beam can be configured to have an oblique angle to the sample surface for detecting both in- and out-of-plane magnetization, or along the normal direction of the sample for detecting out-of-pane magnetization, enabling both longitudinal and polar MOKE. The half waveplate and polarizer 2 (pol2) produce equal intensities of two beams from a linearly polarized light. When the magnet switches its direction, θ_K goes to $-\theta_K$ and the reflected light rotates about the original polarization, resulting in a decrease in one arm of the detector and increase in the other, and is hence detected. The electro-magnet can be tilted with respect to the sample normal to produce both out-of-plane and in-pane magnetic field. Using the calibration and tilt angle, the two components of magnetization can be determined. In-plane switching (of in-plane magnets) and out-of-plane switching (of out-of-plane magnets) of magnets such as YIG, CoFeB and permalloy can be studied with this setup since the switching fields are usually < 100 Oe (1 Oe = 1 Gauss in air). Switching an in-plane magnet to out of plane and vice versa requires fields on the order of 1 Tesla (1 T = 10,000 Gauss) which can be achieved using superconducting electro-magnets, dipole electro-magnets or projected field electro-magnets [196]. Apart from the Kerr rotation of the incident light, rotation can also occur due to Faraday effect in the optics placed near the magnetic field and due to reflection from the substrate. This results in a field dependent linear change in the observed signal, i.e. a tilted hysteresis loop.

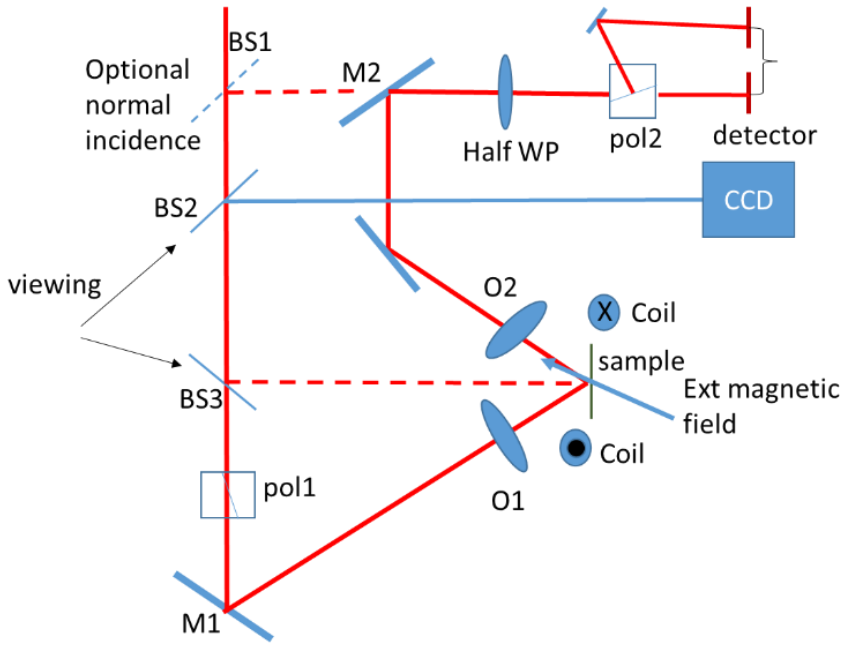

Figure 5.7: Schematic of magnetic field tilted with respect to the sample surface. BS: beam splitter, M: mirror. Half WP: half wave plate. Pol: polarizer. The optical incidence can be either normal or have an incident angle. For oblique incidence: BS1 is not used, and BS2 and BS3 are used for viewing (50 mm lens). For normal incidence, BS1 is used (1000:1 polarizing beam splitter), BS3 is replaced with a mirror and M2 removed. The dashed lines are the beam path for normal incidence. 10x objective provides spot size of ~10 um.

Typical results obtained with normal (out-of-plane magnet, 0.8 nm CoFeB) and oblique (in-plane magnet, 20 nm permalloy) incidence with a He-Ne CW laser are shown in Figure 5.8. Similar result was obtained with an 800 nm ultrafast laser. The absolute magnitude of polarization rotation is in the 0.5-5 mrad range. The samples were provided by Punyashloka Debashis and Prof. Zhihong Chen.

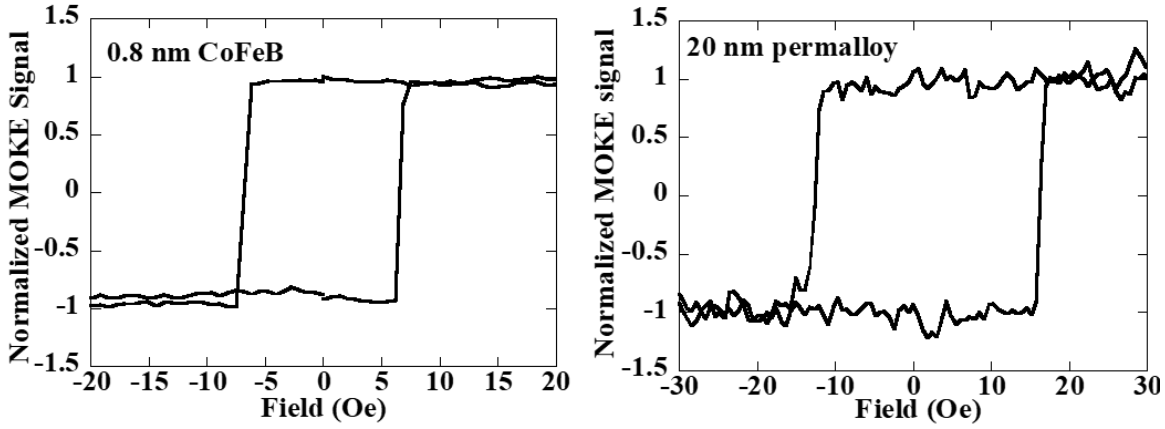

Figure 5.8: Normalized MOKE signal for 0.8 nm CoFeB obtained using normal incidence configuration (left), and for 20 nm permalloy obtained using oblique incidence setup (right).

5.3 Optical switching of ferromagnetic thin films using spin-transfer torque

Novel two-dimensional materials are being discovered on a regular basis and provide a platform for investigation of interesting physical phenomena which could possibly be translated for commercial applications in the future. One such application, closely related to spintronics, as discussed in Chapter 4, is data storage. Emerging ultrathin Van der Waals magnets such as CrI_3 and $Cr_2Ge_2Te_6$ [197] could find applications in ultra-compact storage devices. The devices could be made even faster by optical control of magnetization. To this end, we have proposed coupling of topological insulator materials with two-dimensional magnets to achieve optical excitation of spins in the TI, which upon being transferred to the magnets can lead to optical switching. An all optical approach to excitation and measurement, wherein the magnetization state of the magnet can be read out with the Magneto-optic Kerr effect (MOKE) is being undertaken. The idea is illustrated in Figure 5.9. A circularly polarized pump light passes through a thin (1-5 nm) layer of in-plane ferromagnet (CoFeB, permalloy) and generates spin current in the underlying TI. The spin polarized electrons exert a torque, τ_{spin}, on the ferromagnet's magnetization. The torque can be exerted efficiently since both the photogenerated spin in the TI and the magnetization of the ferromagnet are in-plane. Applying an additional external magnetic field, H_{ext} aids the process of switching, since the threshold switching field is reduced. A linearly polarized probe light (*s* or *p*) is used to perform longitudinal MOKE measurement and detect the magnetization state of the FM after the action of the pump.

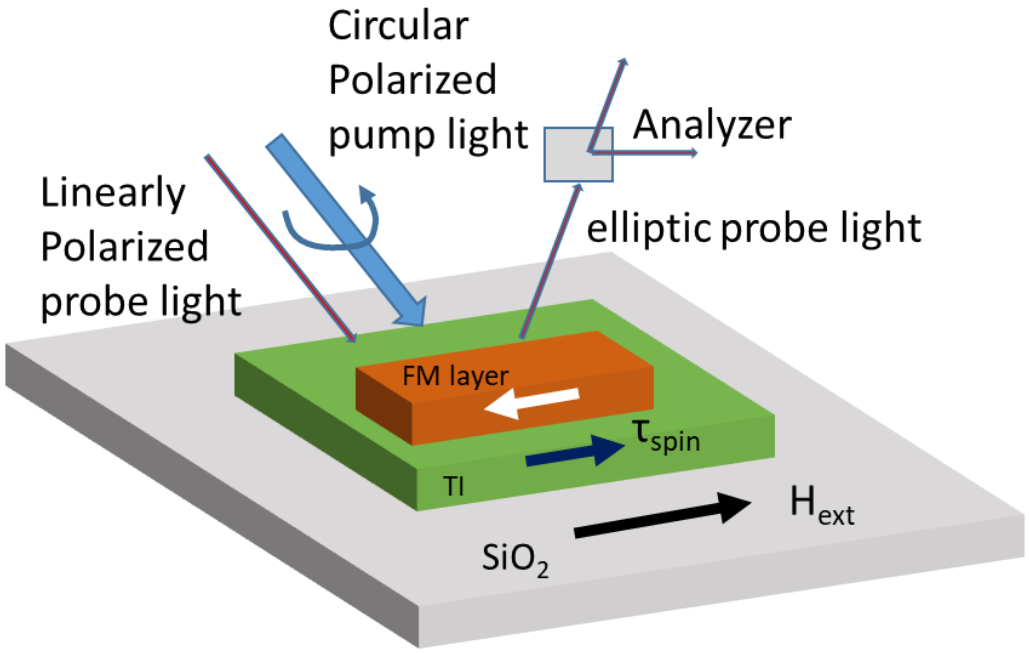

Figure 5.9: Schematic of all optical switching of thin ferromagnet (FM) layer via spin-transfer torque from topological insulator (TI). A circularly polarized light generates spin current in the TI, which exerts a torque, τ_{spin}, on the FM layer. Applying an additional external magnetic field, H_{ext} aids the process of switching. A linearly polarized light is used to perform longitudinal MOKE measurement and detect the magnetization state of the FM.

The ongoing work involves deposition of CoFeB thin film on top of TI, BTS, followed by excitation of the TI with circularly polarized light and detection of CoFeB magnetization switching by MOKE. Primarily CoFeB is an in-plane magnet, but at low thicknesses, it becomes an out-of-plane magnet as shown in Figure 5.10 [198]. Hence, films with thickness of around 1.05 nm (as-deposited) and 1.4 nm (annealed) would be ideally suited, providing in-pane behavior, maximum light transmission and low switching field. However, the MOKE signal strength is also strongly dependent on the thickness, with low signal for thinner films due to smaller light-matter interaction volume. This problem can potentially be overcome by enhancing the signal through interference effects in the underlying substrate, as recently demonstrated [199]. Additionally, out-of-plane CoFeB can also be switched by in-plane spins generated in the TI, but with additional perpendicular in-plane magnetic field requirement [200] as shown in Figure 5.11.

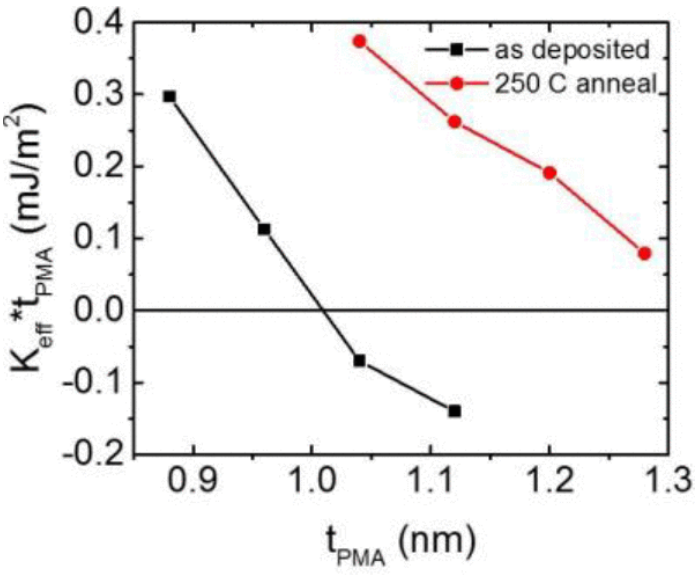

Figure 5.10: K_{eff}*t_{pma} as a function of thickness t_{pma}. Negative values imply in-plane magnetization and positive values imply out-of-plane magnetization [198].

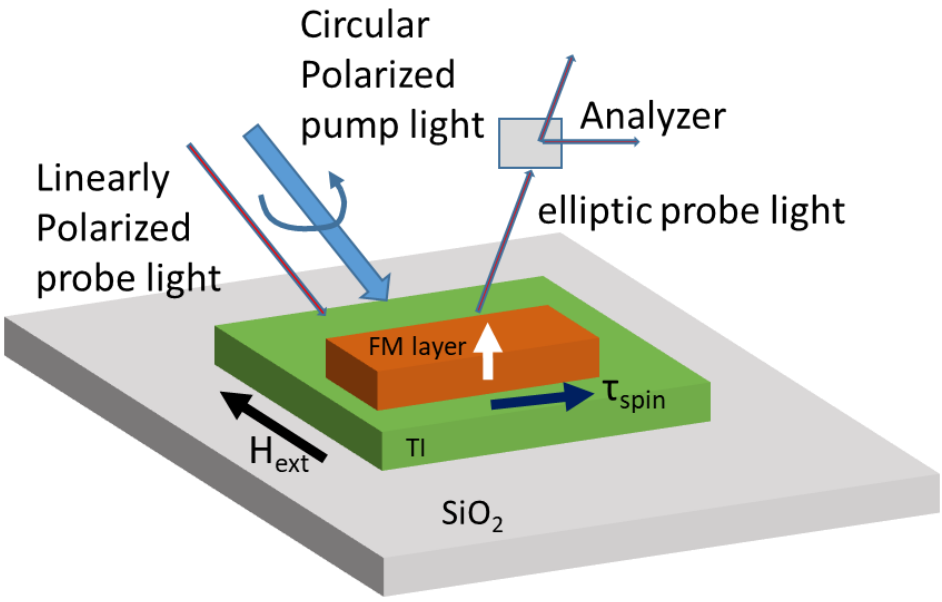

Figure 5.11: Switching of out-of-plane ferromagnet with in-plane spins generated on the surface of the TI. An external magnetic field H_{ext}, perpendicular to both the magnetization and spin direction, is a necessary requirement for the switching process due to torque balance [200].

5.4 Spatially resolved ultrafast dynamics

To study the spatial diffusion of photoexcited carriers over picosecond timescales, a scanning pump-probe system is built, wherein the pump beam is scanned with respect to the probe beam in order to spatially map the carrier distribution and observe effects such as hot carrier and thermal diffusion. The setup is shown in Figure 5.12.

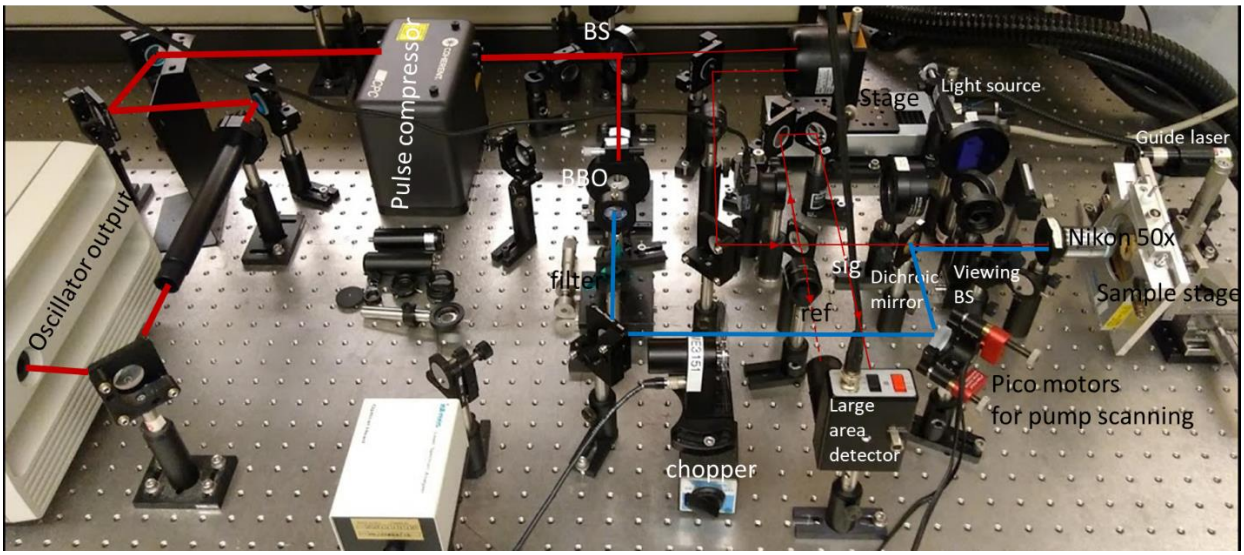

Figure 5.12: Setup for spatially resolved pump-probe spectroscopy.

A pair of pico-motors (Newport Corporation) are retro-fitted on a mirror mount to enable the displacement of the pump beam with respect to the probe beam with a resolution of ~100 nm. A heating stage (Linkam) can be used to control the sample temperature from -190 ^{0}C to 400 ^{0}C. A compact pulse compressor (Coherent Inc) is used to optimized the pulse duration and compensate for the dispersion introduced by the 50x objective.

For diffusive spatial expansion of the excited carriers, the density can be modeled as [201]:

$$\frac{\partial n}{\partial t} = -\frac{n}{\tau_1} + D\nabla^2 n \tag{5-1}$$

where ambipolar diffusion coefficient D and carrier lifetime τ_1 are assumed to be independent of carrier density. The solution is given as:

$$n(r,t) = \frac{1}{4\pi Dt} e^{-r^2/4Dt} e^{-t/\tau_1} \tag{5-2}$$

The time dependence of the full width at half maximum is given by

$$\Delta^2(t) = 11.08Dt + \Delta_0^2 \quad (5\text{-}3)$$

By scanning the pump beam with respect to the probe beam at each time delay, the full width at half maximum of the change in reflectivity, ΔR, can be plotted, which is taken to be directly proportional to the photoexcited carrier density *n*. Hence the diffusion coefficient, *D*, can be obtained by performing a linear fit to the full width half maximum. An example of the evolution of the Gaussian width (w^2) as a function delay along with linear fit for intrinsic GaAs sample is shown in Figure 5.13. The change in reflectance, ΔR is also shown for reference (when pump and probe are overlapped entirely). The obtained value of D is 38 cm^2/s.

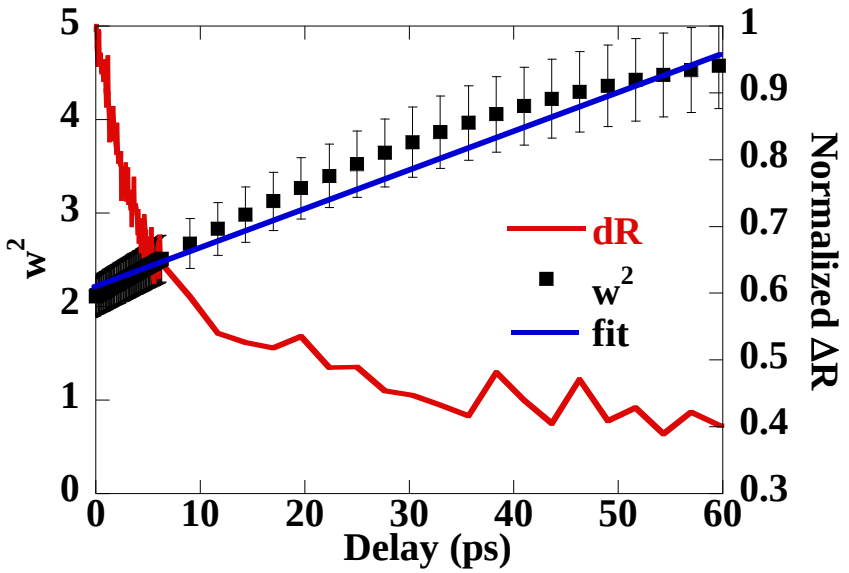

Figure 5.13: Gaussian width squared (w^2) vs delay along with change in reflectance, ΔR, when pump and probe are overlapped. The solid blue line is the linear fit.

The diffusion can be also visualized through an intensity plot as shown in Figure 5.14 for black phosphorus. The expansion in the ΔR profile is clearly observed starting from 20 ps. The obtained value of D is 13.8 cm^2/s translating to a mobility of μ = 540 $cm^2/V.s$ using the formula $\frac{D}{\mu} = \frac{k_B T}{q}$.

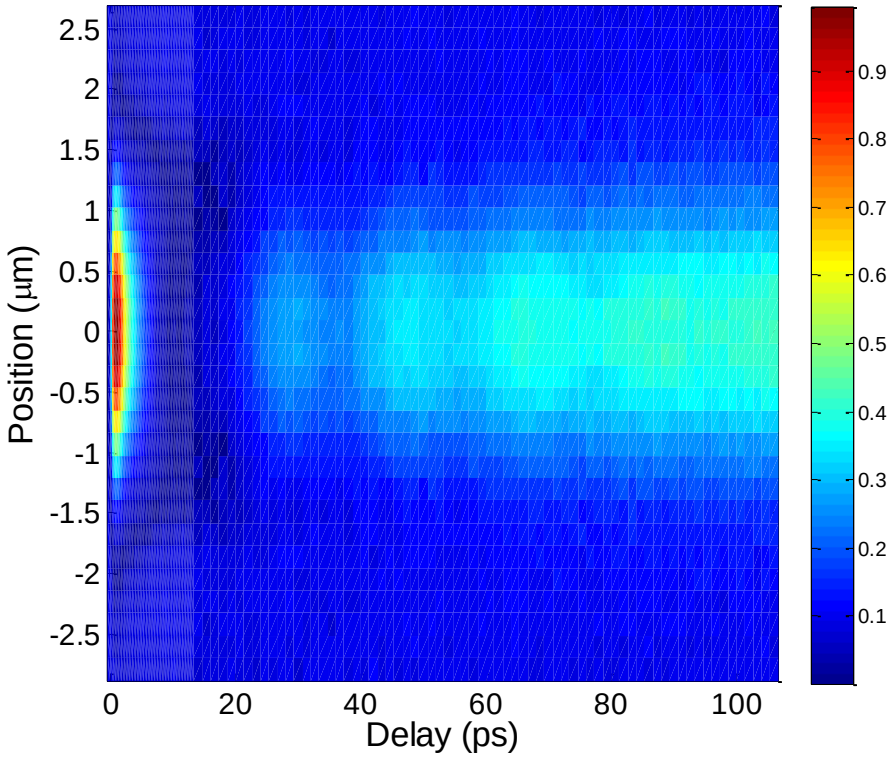

Figure 5.14: Intensity plot of normalized ΔR for black phosphorus as a function of relative pump and probe position and delay. The expansion of the profile is clearly visible.

5.5 Gate dependent spatial dynamics in Bi_2Te_2Se

As discussed in Chapter 4, the surface properties of Bi_2Te_2Se are very different from its bulk properties. The surface behaves like a metal with no bandgap and continuous energy states, along with protection from disorder during transport. These properties implore the question of distinguishing the surface from the bulk diffusion. We utilized the spatially resolved technique along with back-gating of thin flakes of Bi_2Te_2Se in an attempt to controllably identify the surface diffusion phenomena. Figure 5.15 shows the evolution of w^2 and ΔR with delay at various back gate voltages. The w^2 initially drops and then rapidly rises again, followed by a slow increase. Such features were also observed in Bi_2Se_3 [202]. The diffusion coefficient for the different features in the data are summarized in Table 1. We observe that the fast fall and rise more or less follow the dip and rise in the ΔR signal as seen in Figure 5.15b. Moreover, the magnitude of fast fast rise is greatest at 0V bias and drops for higher or lower voltages. A similar drop in the surface state induced photo-current was observed for this sample as shown in Figure 5.16, when the gate

voltage was tuned away from 0V, indicating possible correlation between ultrafast studies and photocurrent measurements. The correlation could imply surface state contribution to the fast rising signal seen in Figure 5.15a.

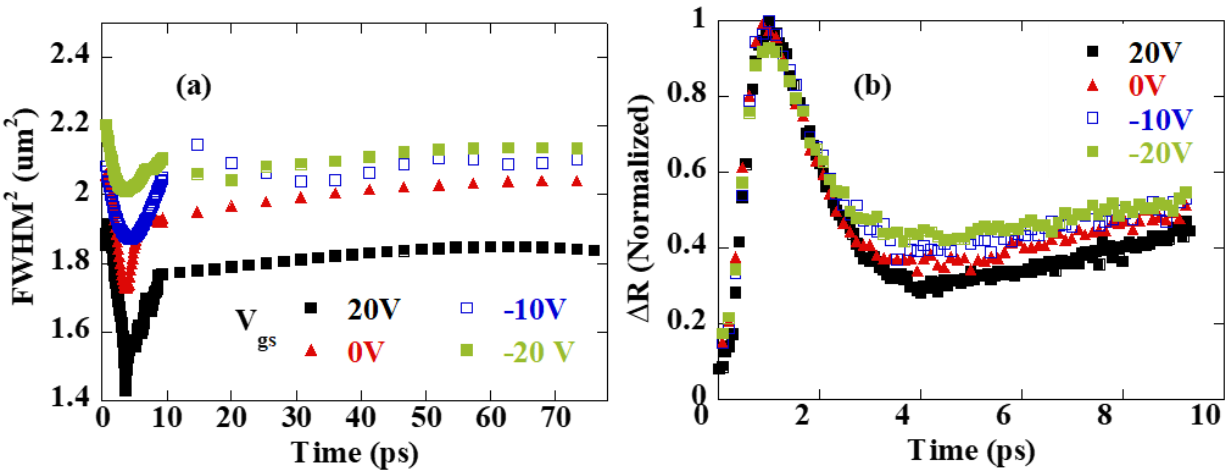

Figure 5.15: (a) Gaussian FWHM^2 vs delay and (b) ΔR vs delay for the first 10 ps at various back gate voltages (V_{gs})

Table 1: Gate voltage dependent diffusion coefficients in Bi_2Te_2Se

V_{gs} (V)	**Fast fall (cm^2/s)**	**Fast rise (cm^2/s)**	**Slow rise (cm^2/s)**
20	128	39	1.4
0	114	80	1.2
-10	61	25	0.84
-20	60	20	1.2

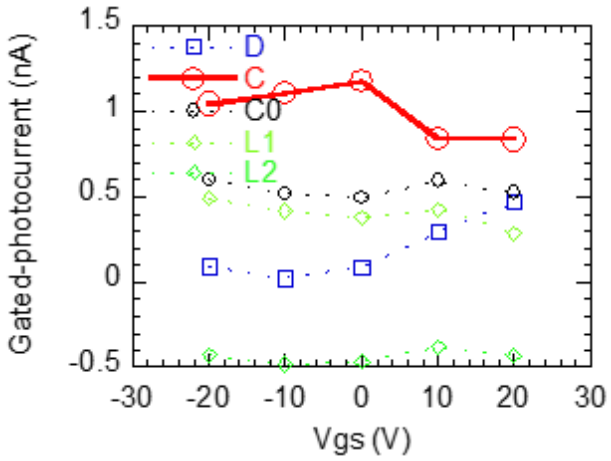

Figure 5.16: Polarization dependent photocurrent terms as a function of gate voltage in Bi_2Te_2Se (Courtesy Shouyuan Huang). The C terms indicates the surface state contribution [31].

6. SUMMARY AND OUTLOOK

To shed light on the fundamental energy interaction processes in emerging two-dimensional semiconductor materials, this dissertation presents studies using ultrafast laser spectroscopy technique. Carrier relaxation dynamics of black phosphorus has been studied using 800 nm excitation and varying probe wavelengths, both above and below the bandgap. The photoexcited carriers form the expected Fermi-Dirac distribution near the bandedge, which was clearly captured in the experiments. Energy dependent electron phonon coupling time and recombination time was extracted by fitting the data with bi-exponential function. More intricate details in the modeling revealed surface oxidation of the samples. The experiments and analysis resulted in the understanding of microscopic energy relaxation processes, and were related to more macroscopic quantities such as electron mobility. As a result of the study, techniques for carrying out mid-infrared pump-probe on 2D materials were better established in the research group, extending the capabilities.

Following the development of the mid-infrared technique, thin films of elemental semiconducting tellurium were investigated. It was found that the ultrafast response of the material was strongly thickness dependent when pumping with 800 nm light and probing with near bandedge 3500 nm probe. A diffusion recombination model accounting for the thickness dependent surface recombination, attributed to mid-gap defect states, was used to quantitatively explain the observations. The material is found to have strong radiative recombination. Furthermore, using the obtained thickness dependence of surface recombination, surface scattering along with bulk scattering terms is proposed to explain the trends in device mobility.

To further explore the exciting properties of 2D materials, topological insulator Bi_2Te_2Se has been studied with special focus on understanding the spin-relaxation timescales. Spintronics is a growing field and promises new kind of logic devices with lossless operation. By using below and above bandgap oblique circular excitation light, surface states in BTS were preferentially excited and their relaxation was studied using a below bandgap probe. It is found that spin population can last greater than 10 ps in thin (<20 nm) samples, which translates to μm spin diffusion length. Several other phenomena such as bulk state to surface state coupling, surface state to bulk phonon coupling and surface band bending could be inferred from the obtained data

and corroborated well with other studies in literature. The study enables a new way to study spin-dynamics by using circularly polarized oblique incident light at ultrafast timescales.

Lastly, a magneto-optic Kerr effect setup has been built to study the generation and coupling of spins in topological insulator/ferromagnetic systems. Preliminary characterization has been performed. A spatially resolved pump-probe system is also in place to study the diffusion of photoexcited carriers on the picosecond timescale.

The techniques developed in the aforementioned projects can be used for further studying other technologically relevant 2D materials.

6.1 Outlook

The ever-increasing demand for higher performance and speed in computing, sensing, automation and electronics has led to far-reaching research efforts in almost all fields of engineering and science. Combined with the emerging power of artificial intelligence and machine learning, new material discovery, device optimization and novel applications are being addressed like never before. Furthermore, the relentless push to take mankind into the quantum age needs efforts in both fundamental physics and device technologies. Quantum information, quantum computing and quantum communications are expected play a central role towards this end in the near future. For this purpose, the microscopic optical, electrical and thermal properties of several emerging platforms such as quantum dots, 2D materials, topological insulators, spin-hall materials, single photon emitters etc. need to be thoroughly understood in order to realize the next generation of quantum devices. Laser spectroscopy is a powerful tool to uncover the mysteries of the aforementioned quantum materials and provide useful characterization information. Spectroscopy with ultrafast lasers provides foundational insights into the study of the interaction and dynamics of fundamental quantum carriers such as electrons, excitons, magnons and phonons. Ultrafast spectroscopy, when closely integrated with other device characterization techniques, will provide unprecedented detail of both the microscopic and macroscopic properties. Several challenging problems in quantum materials can greatly benefit from ultrafast spectroscopy techniques described here. The work presented in this thesis is a stepping stone towards understanding novel material systems and eventual exploration of modern quantum materials. The author firmly believes that this unique spectroscopy technique can play a key role in the forthcoming quantum era.

APPENDIX A. REFLECTIVITY CALCULATION IN BLACK PHOSPHORUS

The MATLAB code use to compute the change in reflectivity following photoexcitation in black phosphorus in Chapter 2, section 2.3 is provided here. The supporting functions in the main code are not included. All the plots in section 2.3 are output from this code.

```
%% code to compute change in refractive index due to optical pumping
clc
clear all

t1 = 5.7e-9;     %doped surface layer thickness
t2 = 59.3e-9;    %bulk thickness

%% photoexcited carrier density

Nex = (0.5e-9*792e-9)/(6.626e-34*3e8)/(pi*(100e-12)*65e-9)/10e6;

T = 300;                %temperature
k = 1.38e-23;           %Boltzmann constant
c = 3*10^8;             %speed of light
h = 6.626*10^-34;       %Plank constant
ma = 0.076*9.1*10^-31; %armchair effective mass
mz = 0.648*9.1*10^-31; %zigzag effective mass
mp = 0.280*9.1*10^-31; %perpendicular effective mass
mef = (ma*mz*mp)^(1/3);%density of states effective mass
hbar = 1.054*10^-34;    %Reduced planck constant

E = -0.4:0.001:0;       %Energy for plotting

fDs = zeros(length(E),4);
for i = 1:4
    if i == 1
    Ef = -0.077;     % equilibrium surface
    end
    if i == 2
    Ef = -0.0771;    % perturbation surface
    end
    if i == 3
    Ef = 0.15;       % equilibrium bulk
    end
    if i == 4
    Ef = 0.149;      % perturbation bulk
    end

% Fermi-dirac* density of states :
fD               =               @(E)               (1.6*10^-19)*(1-(1./(exp((E-
Ef)*1.6/((10^19)*k*T))+1)))*(sqrt(2)/(pi)^2).*sqrt((1.6*10^-19)*(-
E))*(mef^1.5)/(hbar^3);
N(i) = integral(fD,-1,0)/10^6;       % total carrier density
Nsurf(i) = N(i)*(5.75e-7);           % surface carrier density
```

```
%population distribution :

fDs(:,i)                                =                                (1-(1./(exp((E-
Ef)*1.6/((10^19)*k*T))+1)))*(sqrt(2)/(pi)^2).*sqrt((1.6*10^-19)*(-
E))*(ma^1.5)/(hbar^3);
end


dfDs_surf1 = fDs(:,1)-fDs(:,2);              % change in population
dfDs_bulk1 = fDs(:,3)-fDs(:,4);
dE_surf = -dfDs_surf1/min(dfDs_surf1);       % normalized change in epsilon 2
dE_bulk = -dfDs_bulk1/min(dfDs_bulk1);
NfDs_surf1 = fDs(:,1)/max(fDs(:,1));        % normalized population distribution
at equilibrium
NfDs_bulk1 = fDs(:,3)/max(fDs(:,3));

%% kramers kronig

E = 0:0.001:0.4;                          % changing to positive energy to call
function
lamb = h*c./((2*E+0.3)*1.6*10^-19); % wavelength units, including bandgap
w = transpose((E*1.6*10^-19)/hbar); % changing to frequency from energy to call
function
lambda1 = (3e8)*(hbar*2*pi)./(2*E+0.31)/(1.6e-19);
for i = 1:length(E)                  % resorting dE2 to call function
    lambda(i) = lambda1(end+1-i);
end
for i = 1:length(E)                  % resorting dE2 to call function
    dE2_surf(i) = dE_surf(end+1-i);
end
for i = 1:length(E)                  % resorting dE2 to call function
    dE2_bulk(i) = dE_bulk(end+1-i);
end

for i = 1:length(E)                    % resorting normalized distribution for
plotting
    NfDs_surf(i) = NfDs_surf1(end+1-i);
end
for i = 1:length(E)                    % resorting normalized distribution for
plotting
    NfDs_bulk(i) = NfDs_bulk1(end+1-i);
end
for i = 1:length(E)                    % resorting normalized distribution for
plotting
    dfDs_surf(i) = dfDs_surf1(end+1-i);
end
for i = 1:length(E)                    % resorting normalized distribution for
plotting
    dfDs_bulk(i) = dfDs_bulk1(end+1-i);
end

dE1_surf = kkrebook2(w,dE2_surf,0);            % call kramers kronig function
dE1_bulk = kkrebook2(w,dE2_bulk,0);
```

```
dE1surf_lamb = [lamb;dE1_surf];
dE2surf_lamb = [lamb;dE2_surf];
dE1bulk_lamb = [lamb;dE1_bulk];
dE2bulk_lamb = [lamb;dE2_bulk];

[dRe1,dRe2,dRe3,dRe4,WL,R4]=  multiLayer_reflection(t1,t2);  %call  multilayer
function

%% Plotting
for i = 1:length(E)                    % resorting normalized distribution for
plotting
    fDs_surf(i,1) = fDs(end+1-i,1)/max(fDs(:,1));
end
for i = 1:length(E)                    % resorting normalized distribution for
plotting
    fDs_bulk(i,3) = fDs(end+1-i,3)/max(fDs(:,3));
end
figure(1)
plot(E,fDs_surf)       %plot equilibrium surface population
hold on
plot(E,fDs_bulk,'r')   %plot equilibrium bulk population
xlabel('Energy (eV)')
ylabel({'Normalized equilibrium population','(red is bulk)'})

figure(2)
plot(E,dE1_surf)        %plot change in epsilon 1 surface
hold on
plot(E,dE2_surf,'r')    %plot change in epsilon 2 surface
xlabel('Energy (eV)')
ylabel({'dE surface','(red dE2)'});

figure(3)
plot(E,dE1_bulk,'g')    %plot change in epsilon 1 bulk
hold on
plot(E,dE2_bulk,'b')    %plot change in epsilon 2 bulk
xlabel('Energy (eV)')
ylabel({'dE bulk','(blue dE2)'});

%% change in carrier population due to perturbation
figure(4)
plot(E,dfDs_surf/min(dfDs_surf),'r')     %plot change in N due to perturbation
on surface
hold on
plot(E,dfDs_bulk/min(dfDs_bulk),'b')     %plot change in N due to perturbation
in bulk
xlabel('Energy (eV)')
ylabel({'dN perturbation','(blue is bulk)'});

NdfDs_surf =  dfDs_surf/min(dfDs_surf);
NdfDs_bulk = dfDs_bulk/min(dfDs_bulk);

dE1surf_WL = zeros(length(WL),1);
dE2surf_WL = zeros(length(WL),1);
dE1bulk_WL = zeros(length(WL),1);
dE2bulk_WL = zeros(length(WL),1);
```

```
for i = 1:length(WL)
    [c, index] = min(abs(dE1surf_lamb(1,:)-WL(i)));
    dE1surf_WL(i) = dE1surf_lamb(2,index);
    dE2surf_WL(i) = dE2surf_lamb(2,index);
    dE1bulk_WL(i) = dE1bulk_lamb(2,index);
    dE2bulk_WL(i) = dE2bulk_lamb(2,index);
end

dR   =   dRe1'.*dE1surf_WL   +   dRe2'.*dE2surf_WL   +   dRe3'.*dE1bulk_WL   +
dRe4'.*dE2bulk_WL;
NdR = dR/max(dR);

figure(5)
plot(WL*10^6,dR)
xlabel('Wavelength (\mum)')
ylabel('Normalized dR');
```

REFERENCES

[1] N. W. Ashcroft and D. N. Mermin, *Solid State Physics* (Brooks/Cole, 1976).

[2] C. Kittel, *Introduction to Solid State Physics* (John Wiley and Sons, Inc., New York, 2004).

[3] R. F. Pierret, *Advanced Semiconductor Fundamentals* (Pearson Education, New Jersey, 1987).

[4] Nobelprize.org, (2010).

[5] P. Avouris, Nano Lett. **10**, 4285 (2010).

[6] E. Pop, V. Varshney, and A. K. Roy, MRS Bull. **37**, 1273 (2012).

[7] S. V. Morozov, K. S. Novoselov, M. I. Katsnelson, F. Schedin, D. C. Elias, J. A. Jaszczak, and A. K. Geim, Phys. Rev. Lett. **100**, 016602 (2008).

[8] C. Lee, X. Wei, J. W. Kysar, and J. Hone, Science **321**, 385 (2008).

[9] A. B. Kuzmenko, E. Van Heumen, F. Carbone, and D. Van Der Marel, Phys. Rev. Lett. **100**, 117401 (2008).

[10] D. L. Duong, S. J. Yun, and Y. H. Lee, ACS Nano **11**, 11803−11830 (2017).

[11] Z. Zhang, X. Ji, J. Shi, X. Zhou, S. Zhang, Y. Hou, Y. Qi, Q. Fang, Q. Ji, Y. Zhang, M. Hong, P. Yang, X. Liu, Q. Zhang, L. Liao, C. Jin, Z. Liu, and Y. Zhang, ACS Nano **11**, 4328 (2017).

[12] H. Liu, A. T. Neal, Z. Zhu, Z. Luo, X. Xu, D. Tománek, and P. D. Ye, ACS Nano **8**, 4033 (2014).

[13] Y. Wang, G. Qiu, R. Wang, S. Huang, Q. Wang, Y. Liu, Y. Du, W. A. Goddard, M. J. Kim, X. Xu, P. D. Ye, and W. Wu, Nat. Electron. **1**, 228 (2018).

[14] P. K. Venuthurumilli, P. D. Ye, and X. Xu, ACS Nano **12**, 4861 (2018).

[15] H. Liu, Y. Du, Y. Deng, and P. D. Ye, Chem. Soc. Rev. **44**, 2732 (2015).

[16] Z. Luo, J. Maassen, Y. Deng, Y. Du, R. P. Garrelts, M. S. Lundstrom, P. D. Ye, and X. Xu, Nat. Commun. 8572 (2015).

[17] T. Low, A. S. Rodin, A. Carvalho, Y. Jiang, H. Wang, F. Xia, and A. H. Castro Neto, Phys. Rev. B **90**, 075434 (2014).

[18] G. Zhang, S. Huang, A. Chaves, C. Song, V. O. Özçelik, T. Low, and H. Yan, Nat. Commun. **8**, 14071 (2017).

[19] J. Qiao, X. Kong, Z. X. Hu, F. Yang, and W. Ji, Nat. Commun. 4475 (2014).

[20] A. Castellanos-Gomez, J. Phys. Chem. Lett. **6**, 4280 (2015).

[21] S. Huang, M. Segovia, X. Yang, Y. R. Koh, Y. Wang, P. D. Ye, W. Wu, A. Shakouri, X. Ruan, and X. Xu, Unpublished (n.d.).

[22] S. Tutihasi, G. G. Roberts, R. C. Keezer, and R. E. Drews, Phys. Rev. **177**, 1143 (1969).

[23] Nobelprize.org, (2016).

[24] C. L. Kane and E. J. Mele, Phys. Rev. Lett. **95**, 146802 (2005).

[25] M. König, S. Wiedmann, C. Brüne, A. Roth, H. Buhmann, L. W. Molenkamp, X.-L. Qi, and S.-C. Zhang, Science **318**, 766 (2007).

[26] J. E. Moore, Nature **464**, 194 (2010).

[27] M. Golden, (2011).

[28] J. K. Asboth, L. Oroszlany, and A. Palyi, Arxiv **919**, (2015).

[29] H. Li, L. Sheng, D. N. Sheng, and D. Y. Xing, Phys. Rev. B - Condens. Matter Mater. Phys. (2010).

[30] M. Z. Hasan and C. L. Kane, Rev. Mod. Phys. **82**, 3045 (2010).

[31] J. W. McIver, D. Hsieh, H. Steinberg, P. Jarillo-Herrero, and N. Gedik, Nat. Nanotechnol. **7**, 96 (2012).

[32] M. R. Scholz, J. Sanchez-Barriga, J. Braun, D. Marchenko, A. Varykhalov, M. Lindroos, Y. J. Wang, H. Lin, A. Bansil, J. Minar, H. Ebert, A. Volykhov, L. V Yashina, and O. Rader, Phys. Rev. Lett. **110**, 216801 (2013).

[33] W. Yan, O. Txoperena, R. Llopis, H. Dery, L. E. Hueso, and F. Casanova, Nat. Commun. **7**, 13372 (2016).

[34] Y. Xu, I. Miotkowski, C. Liu, J. F. Tian, H. Nam, N. Alidoust, J. N. Hu, C. K. Shih, M. Z. Hasan, and Y. P. Chen, Nat. Phys. **10**, 956 (2014).

[35] Z. Ren, A. A. Taskin, S. Sasaki, K. Segawa, and Y. Ando, Phys. Rev. B **82**, 241306(R) (2010).

[36] Z. Luo, J. Tian, S. Huang, M. Srinivasan, J. Maassen, Y. P. Chen, and X. Xu, ACS Nano **12**, 1120 (2018).

[37] J. M. Dawlaty, S. Shivaraman, M. Chandrashekhar, F. Rana, and M. G. Spencer, Appl. Phys. Lett. **92**, 042116 (2008).

[38] L. Guo and X. Xu, J. Heat Transfer **136**, 122401 (2014).

[39] N. Kumar, J. He, D. He, Y. Wang, and H. Zhao, J. Appl. Phys. **113**, 133702 (2013).

[40] Q. Bao and K. P. Loh, ACS Nano **6**, 3677 (2012).

[41] R. Ganatra and Q. Zhang, ACS Nano (2014).

[42] S. Z. Butler, S. M. Hollen, L. Cao, Y. Cui, J. A. Gupta, H. R. Gutiérrez, T. F. Heinz, S. S. Hong, J. Huang, A. F. Ismach, E. Johnston-Halperin, M. Kuno, V. V. Plashnitsa, R. D. Robinson, R. S. Ruoff, S. Salahuddin, J. Shan, L. Shi, M. G. Spencer, M. Terrones, W. Windl, and J. E. Goldberger, ACS Nano (2013).

[43] G. Fiori, F. Bonaccorso, G. Iannaccone, T. Palacios, D. Neumaier, A. Seabaugh, S. K. Banerjee, and L. Colombo, Nat. Nanotechnol. **9**, 768 (2014).

[44] M. Xu, T. Liang, M. Shi, and H. Chen, Chem. Rev. **113**, 3766 (2013).

[45] F. Xia, H. Wang, and Y. Jia, Nat. Commun. **5**, 4458 (2014).

[46] V. Tran, R. Soklaski, Y. Liang, and L. Yang, Phys. Rev. B - Condens. Matter Mater. Phys. **89**, 235319 (2014).

[47] S. Zhang, J. Yang, R. Xu, F. Wang, W. Li, M. Ghufran, Y. W. Zhang, Z. Yu, G. Zhang, Q. Qin, and Y. Lu, ACS Nano **8**, 9590 (2014).

[48] R. W. Keyes, Phys. Rev. **92**, 580 (1953).

[49] M. Buscema, D. J. Groenendijk, G. A. Steele, H. S. J. Van Der Zant, and A. Castellanos-Gomez, Nat. Commun. 4651 (2014).

[50] L. Bai, L. Sun, Y. Wang, Z. Liu, Q. Gao, H. Xiang, H. Xie, and Y. Zhao, J. Mater. Chem. A **5**, 8280 (2017).

[51] Q. Guo, A. Pospischil, M. Bhuiyan, H. Jiang, H. Tian, D. Farmer, B. Deng, C. Li, S. J. Han, H. Wang, Q. Xia, T. P. Ma, T. Mueller, and F. Xia, Nano Lett. **16**, 4648 (2016).

[52] M. Engel, M. Steiner, and P. Avouris, Nano Lett. **14**, 6414 (2014).

[53] N. Youngblood, C. Chen, S. J. Koester, and M. Li, Nat. Photonics **9**, 247 (2015).

[54] L. Li, Y. Yu, G. J. Ye, Q. Ge, X. Ou, H. Wu, D. Feng, X. H. Chen, and Y. Zhang, Nat. Nanotechnol. **9**, 372 (2014).

[55] L. Li, M. Engel, D. B. Farmer, S. J. Han, and H. S. P. Wong, ACS Nano **10**, 4672 (2016).

[56] S. Winnerl, M. Orlita, P. Plochocka, P. Kossacki, M. Potemski, T. Winzer, E. Malic, A. Knorr, M. Sprinkle, C. Berger, W. A. de Heer, H. Schneider, and M. Helm, Phys. Rev. Lett. **107**, 237401 (2011).

[57] F. Carbone, G. Aubock, A. Cannizzo, F. Van Mourik, R. R. Nair, A. K. Geim, K. S. Novoselov, and M. Chergui, Chem. Phys. Lett. **504**, 37 (2011).

[58] L. Huang, B. Gao, G. Hartland, M. Kelly, and H. Xing, Surf. Sci. **605**, 1657 (2011).

[59] H. Wang, J. H. Strait, P. A. George, S. Shivaraman, V. B. Shields, M. Chandrashekhar, J. Hwang, F. Rana, M. G. Spencer, C. S. Ruiz-Vargas, and J. Park, Appl. Phys. Lett. **96**, 081917 (2010).

[60] Z. Nie, R. Long, L. Sun, C. C. Huang, J. Zhang, Q. Xiong, D. W. Hewak, Z. Shen, O. V. Prezhdo, and Z. H. Loh, ACS Nano **8**, 10931 (2014).

[61] J. H. Strait, P. Nene, and F. Rana, Phys. Rev. B - Condens. Matter Mater. Phys. **90**, 245402 (2014).

[62] H. Wang, C. Zhang, and F. Rana, Nano Lett. **15**, 339 (2015).

[63] S. Ge, C. Li, Z. Zhang, C. Zhang, Y. Zhang, J. Qiu, Q. Wang, J. Liu, S. Jia, J. Feng, and D. Sun, Nano Lett. **15**, 4650 (2015).

[64] J. He, D. He, Y. Wang, Q. Cui, M. Z. Bellus, H. Y. Chiu, and H. Zhao, ACS Nano **9**, 6436 (2015).

[65] R. J. Suess, M. M. Jadidi, T. E. Murphy, and M. Mittendorff, Appl. Phys. Lett. **107**, 081103 (2015).

[66] K. Wang, B. M. Szydłowska, G. Wang, X. Zhang, J. J. Wang, J. J. Magan, L. Zhang, J. N. Coleman, J. Wang, and W. J. Blau, ACS Nano **10**, 6923 (2016).

[67] J. Shang, T. Yu, J. Lin, and G. G. Gurzadyan, ACS Nano **5**, 3278 (2011).

[68] H. Shi, R. Yan, S. Bertolazzi, J. Brivio, B. Gao, A. Kis, D. Jena, H. G. Xing, and L. Huang, ACS Nano **7**, 1072 (2013).

[69] M. Baba, F. Izumida, Y. Takeda, K. Shibata, A. Morita, Y. Koike, and T. Fukase, J. Phys. Soc. Japan **60**, 3777 (1991).

[70] Y. Akahama, S. Endo, and S. Narita, Phys. B+C **139**, 397 (1986).

[71] T. R. Harris, Optical Properties of Si, Ge, GaAs, GaSb, InAs, and InP at Elevated Temperatures, Ohio Air Force Institute of Technology, 2010.

[72] S. ichiro Narita, S. ichi Terada, S. Mori, K. Muro, Y. Akahama, and S. Endo, J. Phys. Soc. Japan **52**, 3544 (1983).

[73] Y. Du, L. Yang, H. Zhou, and P. D. Ye, IEEE Electron Device Lett. **37**, 429 (2016).

[74] Y. C. Du, A. T. Neal, H. Zhou, and P. D. Ye, J. Physics-Condensed Matter **28**, 263002 (2016).

[75] S. M. Sze and K. K. Ng, *Physics of Semiconductor Devices* (John Wiley & Sons, New Jersey, 2006).

[76] S. Ramo, W. J.R, and T. Van Duzer, *Fields and Waves in Communication Electronics* (John Wiley and Sons, New York, 1994).

[77] F. L. Pedrotti, L. M. S. Pedrotti, L. M. S. Pedrotti, and Pedrotti, *Introduction to Optics (3rd Edition)* (2006).

[78] S. Ge, X. Liu, X. Qiao, Q. Wang, Z. Xu, J. Qiu, P. H. Tan, J. Zhao, and D. Sun, Sci. Rep. **4**, 5722 (2014).

[79] Y. D. Glinka, S. Babakiray, T. A. Johnson, M. B. Holcomb, and D. Lederman, J. Appl. Phys. **117**, 165703 (2015).

[80] E. P. N. Damen, A. F. M. Arts, and H. W. de Wijn, Phys. Rev. Lett. **74**, 4249 (1995).

[81] Y. Yan, E. B. Gamble, and K. A. Nelson, J. Chem. Phys. **83**, 5391 (1985).

[82] X. Peng, Q. Wei, and A. Copple, Phys. Rev. B - Condens. Matter Mater. Phys. **90**, 085402 (2014).

[83] J. W. Jiang and H. S. Park, Phys. Rev. B - Condens. Matter Mater. Phys. **91**, 235118 (2015).

[84] N. Briggs, S. Subramanian, Z. Lin, X. Li, X. Zhang, K. Zhang, K. Xiao, D. Geohegan, R. Wallace, L.-Q. Chen, M. Terrones, A. Ebrahimi, S. Das, J. Redwing, C. Hinkle, K. Momeni, A. van Duin, V. Crespi, S. Kar, and J. A. Robinson, 2D Mater. **6**, 022001 (2019).

[85] F. Schwierz, Nat. Nanotechnol. **5**, 487 (2010).

[86] Q. H. Wang, K. Kalantar-Zadeh, A. Kis, J. N. Coleman, and M. S. Strano, Nat. Nanotechnol. **7**, 699 (2012).

[87] Y. L. Chen, J. G. Analytis, J.-H. Chu, Z. K. Liu, S.-K. Mo, X. L. Qi, H. J. Zhang, D. H. Lu, X. Dai, Z. Fang, S. C. Zhang, I. R. Fisher, Z. Hussain, and Z.-X. Shen, Science **325**, 178 (2009).

[88] L. Cheng and Y. Liu, J. Am. Chem. Soc. **140**, 17895 (2018).

[89] Z. Yu, Z.-Y. Ong, S. Li, J.-B. Xu, G. Zhang, Y.-W. Zhang, Y. Shi, and X. Wang, Adv. Funct. Mater. **27**, 1604093 (2017).

[90] J. O. Island, G. A. Steele, H. S. J. van der Zant, and A. Castellanos-Gomez, 2D Mater. **2**, 011002 (2015).

[91] C. Durand, X.-G. Zhang, S. M. Hus, C. Ma, M. A. McGuire, Y. Xu, H. Cao, I. Miotkowski, Y. P. Chen, and A.-P. Li, Nano Lett. **16**, 2213 (2016).

[92] A. Reina, X. Jia, J. Ho, D. Nezich, H. Son, V. Bulovic, M. S. Dresselhaus, and J. Kong, Nano Lett. **9**, 30 (2009).

[93] A. Roy, H. C. P. Movva, B. Satpati, K. Kim, R. Dey, A. Rai, T. Pramanik, S. Guchhait, E. Tutuc, and S. K. Banerjee, ACS Appl. Mater. Interfaces **8**, 7396 (2016).

[94] J. Kang, J. D. Wood, S. A. Wells, J.-H. Lee, X. Liu, K.-S. Chen, and M. C. Hersam, ACS Nano **9**, 3596 (2015).

[95] Y.-C. Lin, W. Zhang, J.-K. Huang, K.-K. Liu, Y.-H. Lee, C.-T. Liang, C.-W. Chu, and L.-J. Li, Nanoscale **4**, 6637 (2012).

[96] Y. Lee, S. Bae, H. Jang, S. Jang, S.-E. Zhu, S. H. Sim, Y. Il Song, B. H. Hong, and J.-H. Ahn, Nano Lett. **10**, 490 (2010).

[97] Y. Wang, R. de Souza Borges Ferreira, R. Wang, G. Qiu, G. Li, Y. Qin, P. D. Ye, A. Sabbaghi, and W. Wu, Nano Energy **57**, 480 (2019).

[98] M. Amani, C. Tan, G. Zhang, C. Zhao, J. Bullock, X. Song, H. Kim, V. R. Shrestha, Y. Gao, K. B. Crozier, M. Scott, and A. Javey, ACS Nano **12**, 7253 (2018).

[99] S. Berweger, G. Qiu, Y. Wang, B. Pollard, K. L. Genter, R. Tyrrell-Ead, T. M. Wallis, W. Wu, P. D. Ye, and P. Kabos, Nano Lett. **19**, 1289 (2019).

[100] G. Qiu, Y. Wang, Y. Nie, Y. Zheng, K. Cho, W. Wu, and P. D. Ye, Nano Lett. **18**, 5760 (2018).

[101] W. Wu, G. Qiu, Y. Wang, R. Wang, and P. Ye, Chem. Soc. Rev. **47**, 7203 (2018).

[102] C. Chen, I. Vasudevan, Z. Du, X. Xu, and L. Pan, Appl. Phys. Lett. **112**, 253105 (2018).

[103] B. T. Spann and X. Xu, Appl. Phys. Lett. **105**, 083111 (2014).

[104] F. Ceballos and H. Zhao, Adv. Funct. Mater. **27**, 1604509 (2017).

[105] V. Iyer, Y. P. Chen, and X. Xu, Phys. Rev. Lett. **121**, 026807 (2018).

[106] S. Hunsche, K. Wienecke, T. Dekorsy, and H. Kurz, Phys. Rev. Lett. **75**, 1815 (1995).

[107] N. Kamaraju, S. Kumar, M. Anija, and A. K. Sood, Phys. Rev. B **82**, 195202 (2010).

[108] Y. Pan, S. Gao, L. Yang, and J. Lu, Phys. Rev. B **98**, 085135 (2018).

[109] H. M. Hill, A. F. Rigosi, C. Roquelet, A. Chernikov, T. C. Berkelbach, D. R. Reichman, M. S. Hybertsen, L. E. Brus, and T. F. Heinz, Nano Lett. **15**, 2992 (2015).

[110] K. Yao, A. Yan, S. Kahn, A. Suslu, Y. Liang, E. S. Barnard, S. Tongay, A. Zettl, N. J. Borys, and P. J. Schuck, Phys. Rev. Lett. **119**, 087401 (2017).

[111] A. Ferreira da Silva, N. Veissid, C. Y. An, I. Pepe, N. Barros de Oliveira, and A. V. Batista da Silva, Appl. Phys. Lett. **69**, 1930 (1996).

[112] D. Redfield, Phys. Rev. **100**, 1094 (1955).

[113] V. A. Vis, J. Appl. Phys. **35**, 360 (1964).

[114] A. Bringer and G. Nimtz, Phys. Status Solidi **46**, 235 (1971).

[115] P. Bhaskar, A. W. Achtstein, M. J. W. Vermeulen, and L. D. A. Siebbeles, J. Phys. Chem. C **123**, 841 (2019).

[116] J. S. Blakemore, J. W. Schultz, and K. C. Nomura, J. Appl. Phys. **31**, 2226 (1960).

[117] J. Qiao, Y. Pan, F. Yang, C. Wang, Y. Chai, and W. Ji, Sci. Bull. **63**, 159 (2018).

[118] E. H. Sondheimer, Adv. Phys. **1**, 1 (1952).

[119] F. Lacy, Nanoscale Res. Lett. **6**, 636 (2011).

[120] L. Yuan and L. Huang, Nanoscale **7**, 7402 (2015).

[121] T. Wang, Y. Zhang, Y. Liu, J. Li, D. Liu, J. Luo, and K. Ge, J. Phys. Chem. C **122**, 18651 (2018).

[122] N. Kumar, Q. Cui, F. Ceballos, D. He, Y. Wang, and H. Zhao, Nanoscale **6**, 4915 (2014).

[123] T. Korn, S. Heydrich, M. Hirmer, J. Schmutzler, and C. Schüller, Appl. Phys. Lett. **99**, 102109 (2011).

[124] C. Robert, D. Lagarde, F. Cadiz, G. Wang, B. Lassagne, T. Amand, A. Balocchi, P. Renucci, S. Tongay, B. Urbaszek, and X. Marie, Phys. Rev. B **93**, 205423 (2016).

[125] E. Bangert, D. Fischer, and P. Grosse, Phys. Status Solidi **59**, 419 (1973).

[126] D. Fischer, E. Bangert, and P. Grosse, Phys. Status Solidi **55**, 527 (1973).

[127] R. Enderlein and A. Hache, Phys. Status Solidi **60**, 739 (1973).

[128] S. Das, H. Y. Chen, A. V. Penumatcha, and J. Appenzeller, Nano Lett. **13**, 100 (2013).

[129] L. Fu and C. L. Kane, Phys. Rev. B - Condens. Matter Mater. Phys. **76**, 045302 (2007).

[130] Y. Xia, D. Qian, D. Hsieh, L. Wray, A. Pal, H. Lin, A. Bansil, D. Grauer, Y. S. Hor, R. J. Cava, and M. Z. Hasan, Nat. Phys. **5**, 398 (2009).

[131] P. Roushan, J. Seo, C. V Parker, Y. S. Hor, D. Hsieh, D. Qian, A. Richardella, M. Z. Hasan, R. J. Cava, and A. Yazdani, Nature **460**, 1106 (2009).

[132] T. Zhang, P. Cheng, X. Chen, J. F. Jia, X. C. Ma, K. He, L. L. Wang, H. J. Zhang, X. Dai, Z. Fang, X. C. Xie, and Q. K. Xue, Phys. Rev. Lett. **103**, 266803 (2009).

[133] J. F. Tian, I. Miotkowski, S. Hong, and Y. P. Chen, Sci. Rep. **5**, 14293 (2015).

[134] J. G. Checkelsky, Y. S. Hor, R. J. Cava, and N. P. Ong, Phys. Rev. Lett. **106**, 196801 (2011).

[135] N. Koirala, M. Brahlek, M. Salehi, L. Wu, J. X. Dai, J. Waugh, T. Nummy, M. G. Han, J. Moon, Y. M. Zhu, D. Dessau, W. D. Wu, N. P. Armitage, and S. Oh, Nano Lett. **15**, 8245 (2015).

[136] N. P. Butch, K. Kirshenbaum, P. Syers, A. B. Sushkov, G. S. Jenkins, H. D. Drew, and J. Paglione, Phys. Rev. B **81**, 241301 (2010).

[137] Y. Q. Huang, Y. X. Song, S. M. Wang, I. A. Buyanova, and W. M. Chen, Nat. Commun. **8**, 15401 (2017).

[138] A. A. Baker, A. I. Figueroa, L. J. Collins-McIntyre, G. van der Laan, and T. Hesjedal, Sci. Rep. **5**, 7907 (2015).

[139] P. Chuang, S.-C. Ho, L. W. Smith, F. Sfigakis, M. Pepper, C.-H. Chen, J.-C. Fan, J. P. Griffiths, I. Farrer, H. E. Beere, G. A. C. Jones, D. A. Ritchie, and T.-M. Chen, Nat. Nanotechnol. **10**, 35 (2014).

[140] Y. G. Semenov, K. W. Kim, and J. M. Zavada, Appl. Phys. Lett. **91**, 153105 (2007).

[141] C. C. Lin, A. V Penumatcha, Y. F. Gao, V. Q. Diep, J. Appenzeller, and Z. H. Chen, Nano Lett. **13**, 5177 (2013).

[142] P. J. Zomer, M. H. D. Guimaraes, N. Tombros, and B. J. van Wees, Phys. Rev. B **86**, 161416(R) (2012).

[143] P. Hosur, Phys. Rev. B **83**, 035309 (2011).

[144] M. Xia, J. Jiang, Z. R. Ye, Y. H. Wang, Y. Zhang, S. D. Chen, X. H. Niu, D. F. Xu, F. Chen, X. H. Chen, B. P. Xie, T. Zhang, and D. L. Feng, Sci. Rep. **4**, 5999 (2014).

[145] J. H. Han, A. Richardella, S. A. Siddiqui, J. Finley, N. Samarth, and L. Q. Liu, Phys. Rev. Lett. **119**, 077702 (2017).

[146] Y. Wang, D. P. Zhu, Y. Wu, Y. M. Yang, J. W. Yu, R. Ramaswamy, R. Mishra, S. Y. Shi, M. Elyasi, K. L. Teo, Y. H. Wu, and H. Yang, Nat. Commun. **8**, 1364 (2017).

[147] J. A. Sobota, S. Yang, J. G. Analytis, Y. L. Chen, I. R. Fisher, P. S. Kirchmann, and Z. X. Shen, Phys. Rev. Lett. **108**, 117403 (2012).

[148] Y. H. Wang, D. Hsieh, E. J. Sie, H. Steinberg, D. R. Gardner, Y. S. Lee, P. Jarillo-Herrero, and N. Gedik, Phys. Rev. Lett. **109**, 127401 (2012).

[149] S. Souma, K. Kosaka, T. Sato, M. Komatsu, A. Takayama, T. Takahashi, M. Kriener, K. Segawa, and Y. Ando, Phys. Rev. Lett. **106**, 216803 (2011).

[150] A. Crepaldi, B. Ressel, F. Cilento, M. Zacchigna, C. Grazioli, H. Berger, P. Bugnon, K. Kern, M. Grioni, and F. Parmigiani, Phys. Rev. B **86**, 205133 (2012).

[151] J. Sanchez-Barriga, E. Golias, A. Varykhalov, J. Braun, L. V Yashina, R. Schumann, J. Minar, H. Ebert, O. Kornilov, and O. Rader, Phys. Rev. B **93**, 155426 (2016).

[152] K. Kuroda, J. Reimann, J. Gudde, and U. Hofer, Phys. Rev. Lett. **116**, 076801 (2016).

[153] K. Kuroda, J. Reimann, K. A. Kokh, O. E. Tereshchenko, A. Kimura, J. Gudde, and U. Hofer, Phys. Rev. B **95**, 081103(R) (2017).

[154] R. V Aguilar, J. Qi, M. Brahlek, N. Bansal, A. Azad, J. Bowlan, S. Oh, A. J. Taylor, R. P. Prasankumar, and D. A. Yarotski, Appl. Phys. Lett. **106**, 011901 (2015).

[155] S. Sim, M. Brahlek, N. Koirala, S. Cha, S. Oh, and H. Choi, Phys. Rev. B **89**, 165137 (2014).

[156] S. Y. Maezawa, H. Watanabe, M. Takeda, K. Kuroda, T. Someya, I. Matsuda, and T. Suemoto, Sci. Rep. **5**, 16443 (2015).

[157] A. Q. Wu, X. Xu, and R. Venkatasubramanian, Appl. Phys. Lett. **92**, 011108 (2008).

[158] C. W. Luo, H. J. Wang, S. A. Ku, H. J. Chen, T. T. Yeh, J. Y. Lin, K. H. Wu, J. Y. Juang, B. L. Young, T. Kobayashi, C. M. Cheng, C. H. Chen, K. D. Tsuei, R. Sankar, F. C. Chou, K. A. Kokh, O. E. Tereshchenko, E. V Chulkov, Y. M. Andreev, and G. D. Gu, Nano Lett. **13**, 5797 (2013).

[159] D. Hsieh, F. Mahmood, J. W. McIver, D. R. Gardner, Y. S. Lee, and N. Gedik, Phys. Rev. Lett. **107**, 077401 (2011).

[160] M. C. Wang, S. Qiao, Z. Jiang, S. N. Luo, and J. Qi, Phys. Rev. Lett. **116**, 036601 (2016).

[161] C. Kastl, C. Karnetzky, H. Karl, and A. W. Holleitner, Nat. Commun. **6**, 6617 (2015).

[162] A. Akrap, M. Tran, A. Ubaldini, J. Teyssier, E. Giannini, D. van der Marel, P. Lerch, and C. C. Homes, Phys. Rev. B **86**, 235207 (2012).

[163] H. Cao, C. Liu, J. Tian, and Y. Xu, ArXiv Prepr. ArXiv … (2014).

[164] X. Liu and J. Sinova, Phys. Rev. Lett. **111**, 166801 (2013).

[165] S. R. Park, W. S. Jung, C. Kim, D. J. Song, S. Kimura, K. D. Lee, and N. Hur, Phys. Rev. B **81**, 041405(R) (2010).

[166] Z. H. Zhu, G. Levy, B. Ludbrook, C. N. Veenstra, J. A. Rosen, R. Comin, D. Wong, P. Dosanjh, A. Ubaldini, P. Syers, N. P. Butch, J. Paglione, I. S. Elfimov, and A. Damascelli, Phys. Rev. Lett. **107**, 186405 (2011).

[167] C. T. Y. Chen, S. L. He, H. Weng, W. T. Zhang, L. Zhao, H. Y. Liu, X. W. Jia, D. X. Mou, S. Y. Liu, J. F. He, Y. Y. Peng, Y. Feng, Z. J. Xie, G. D. Liu, X. L. Dong, J. Zhang, X. Y. Wang, Q. J. Peng, Z. M. Wang, S. J. Zhang, F. Yang, C. T. Y. Chen, Z. Y. Xu, X. Dai, Z. Fang, and X. J. Zhou, Proc. Natl. Acad. Sci. U. S. A. **109**, 3694 (2012).

[168] M. Bianchi, D. D. Guan, S. N. Bao, J. L. Mi, B. B. Iversen, P. D. C. King, and P. Hofmann, Nat. Commun. **1**, 128 (2010).

[169] D. Hsieh, J. W. McIver, D. H. Torchinsky, D. R. Gardner, Y. S. Lee, and N. Gedik, Phys. Rev. Lett. **106**, 057401 (2011).

[170] D. Hsieh, Y. Xia, D. Qian, L. Wray, J. H. Dil, F. Meier, J. Osterwalder, L. Patthey, J. G. Checkelsky, N. P. Ong, A. V Fedorov, H. Lin, A. Bansil, D. Grauer, Y. S. Hor, R. J. Cava, and M. Z. Hasan, Nature **460**, 1101 (2009).

[171] L. Fu, Phys. Rev. Lett. **103**, 266801 (2009).

[172] M. S. Bahramy, P. D. C. King, A. de la Torre, J. Chang, M. Shi, L. Patthey, G. Balakrishnan, P. Hofmann, R. Arita, N. Nagaosa, and F. Baumberger, Nat. Commun. **3**, 1159 (2012).

[173] W. Jung, Y. Kim, B. Kim, Y. Koh, C. Kim, M. Matsunami, S. Kimura, M. Arita, K. Shimada, J. H. Han, J. Kim, and B. Cho, Phys. Rev. B **84**, 245435 (2011).

[174] Y. H. Wang, D. Hsieh, D. Pilon, L. Fu, D. R. Gardner, Y. S. Lee, and N. Gedik, Phys. Rev. Lett. **107**, 207602 (2011).

[175] V. Iyer, P. Ye, and X. Xu, 2D Mater. **4**, 021032 (2017).

[176] F. X. Xiu, L. A. He, Y. Wang, L. N. Cheng, L. T. Chang, M. R. Lang, G. A. Huang, X. F. Kou, Y. Zhou, X. W. Jiang, Z. G. Chen, J. Zou, A. Shailos, and K. L. Wang, Nat. Nanotechnol. **6**, 216 (2011).

[177] M. Konig, M. Baenninger, A. G. F. Garcia, N. Harjee, B. L. Pruitt, C. Ames, P. Leubner, C. Brune, H. Buhmann, L. W. Molenkamp, and D. Goldhaber-Gordon, Phys. Rev. X **3**, 021003 (2013).

[178] J. Dufouleur, L. Veyrat, B. Dassonneville, C. Nowka, S. Hampel, P. Leksin, B. Eichler, O. G. Schmidt, B. Buchner, and R. Giraud, Nano Lett. **16**, 6733 (2016).

[179] J. Bass and W. P. Pratt, J. Physics-Condensed Matter **19**, 183201 (2007).

[180] J. Sanchez-Barriga, M. Battiato, E. Golias, A. Varykhalov, L. V Yashina, O. Kornilov, and O. Rader, Appl. Phys. Lett. **110**, 141605 (2017).

[181] M. Neupane, S. Y. Xu, Y. Ishida, S. Jia, B. M. Fregoso, C. Liu, I. Belopolski, G. Bian, N. Alidoust, T. Durakiewicz, V. Galitski, S. Shin, R. J. Cava, and M. Z. Hasan, Phys. Rev. Lett. **115**, 116801 (2015).

[182] C. Mai, A. Barrette, Y. F. Yu, Y. G. Semenov, K. W. Kim, L. Y. Cao, and K. Gundogdu, Nano Lett. **14**, 202 (2014).

[183] F. Mahmood, Z. Alpichshev, Y. H. Lee, J. Kong, and N. Gedik, Nano Lett. **18**, 223 (2018).

[184] R. Schmidt, G. Berghauser, R. Schneider, M. Selig, P. Tonndorf, E. Malic, A. Knorr, S. M. de Vasconcellos, and R. Bratschitsch, Nano Lett. **16**, 2945 (2016).

[185] J. L. Wang, L. Guo, C. H. Liu, X. Xu, and Y. F. Chen, Appl. Phys. Lett. **107**, 063107 (2015).

[186] K. Norimatsu, J. Hu, A. Goto, K. Igarashi, T. Sasagawa, and K. G. Nakamura, Solid State Commun. **157**, 58 (2013).

[187] Y. Wang, L. Guo, X. Xu, J. Pierce, and R. Venkatasubramanian, Phys. Rev. B **88**, 064307 (2013).

[188] I. Boulares, G. Shi, E. Kioupakis, P. Lošťák, C. Uher, and R. Merlin, Solid State Commun. **271**, 1 (2018).

[189] T. Haider, Int. J. Electromagn. Appl. (2017).

[190] Y. Wang, D. Zhu, Y. Wu, Y. Yang, J. Yu, R. Ramaswamy, R. Mishra, S. Shi, M. Elyasi, K.-L. Teo, Y. Wu, and H. Yang, Nat. Commun. **8**, 1364 (2017).

[191] S. Pan, W. Kong, J. Liu, X. Ge, P. Zereshki, S. Hao, D. He, Y. Wang, and H. Zhao, ACS Appl. Nano Mater. (2019).

[192] T. Zhu, J. M. Snaider, L. Yuan, and L. Huang, Annu. Rev. Phys. Chem. (2019).

[193] J. M. Snaider, Z. Guo, T. Wang, M. Yang, L. Yuan, K. Zhu, and L. Huang, ACS Energy Lett. (2018).

[194] A. Block, M. Liebel, R. Yu, M. Spector, Y. Sivan, F. J. García De Abajo, and N. F. Van Hulst, Sci. Adv. (2019).

[195] S. Yamamoto and I. Matsuda, Appl. Sci. (2017).

[196] (n.d.).

[197] K. S. Burch, D. Mandrus, and J.-G. Park, Nature **563**, 47 (2018).

[198] P. Debashis, R. Faria, K. Y. Camsari, S. Datta, and Z. Chen, (2019).

[199] S. Sumi, H. Awano, and M. Hayashi, Sci. Rep. **8**, (2018).

[200] L. Liu, O. J. Lee, T. J. Gudmundsen, D. C. Ralph, and R. A. Buhrman, Phys. Rev. Lett. **109**, 096602 (2012).

[201] L. M. Smith, D. R. Wake, J. P. Wolfe, D. Levi, M. V. Klein, J. Klem, T. Henderson, and H. Morkoç, Phys. Rev. B **38**, 5788 (1988).

[202] N. Kumar, B. A. Ruzicka, N. P. Butch, P. Syers, K. Kirshenbaum, J. Paglione, and H. Zhao, Phys. Rev. B - Condens. Matter Mater. Phys. (2011).

VITA

Vasudevan Rajagopal Iyer

Education

Purdue University, USA West Lafayette, IN

Ph.D. in Mechanical Engineering, **GPA: 3.90/4** Feb 2020

Indian Institute of Technology Madras Chennai, India

B.Tech (Hons.) in Mechanical Engineering, **GPA: 9.21/10** May 2014

Skills

Characterization: Laser spectroscopy, Raman spectroscopy, FTIR, UV-VIS, AFM, two/four probe.

Computer: C++, MS Office, MATLAB, Python, LabVIEW, AutoCAD, COMSOL, ANSYS.

Conferences

1. "Ultrafast carrier dynamics in topological insulator Bi_2Te_2Se", **Iyer, V.,** Xu, X. *Gordon Research Conference on Ultrafast Phenomena in Cooperative systems*, Galveston, TX, February 4-9, 2018.
2. "Carrier dynamics of topological insulator surface states", **Iyer, V.,** Xu, X. *International Mechanical Engineering Congress and Exposition*, Tampa, FL, USA, November 6-9, 2017.
3. "Carrier dynamics in black phosphorus for applications in 2D electronics", **Iyer, V**., Ye, P. and Xu, X., *Electronic Materials Conference*, South Bend, IN, USA, June 29-30, 2017.

Teaching Experience

Graduate Teaching Assistant - Purdue University, USA (Aug'18-May'19)

- Served as teaching assistant for undergraduate heat and mass transfer course. Conducted recitation sessions for problem solving and supervised students for lab sessions and projects.

Affiliations

- Student member of the American Society of Mechanical Engineers (ASME)
- Student member of the Institute of Electrical and Electronics Engineers (IEEE)

PUBLICATIONS

1. **Iyer, V**., Segovia, M., Wang, Y., Wu, W., Ye, P., Xu, X. Infrared Ultrafast Spectroscopy of Solution Grown Thin Film Tellurium, *Phys. Rev. B* 100 (7), 075436, 2019.
2. Venuthurumilli, P., Wen, X., **Iyer, V.,** Chen, Y.P., Xu, X. Near-Field Imaging of Surface Plasmons from the Bulk and Surface State of Topological Insulator Bi_2Te_2Se, *ACS Photonics.* 6 (10), 2492-2498, 2019.
3. Salihoglu, H., **Iyer, V.,** Taniguchi, T., Watanabe, K., Xu, X. Energy Transport by Electromagnetic Waves Comparable to Phonon Conduction in Natural Hyperbolic Material, *Advanced Functional Materials* 1905830, 2019.
4. Chi, T., Somers, P., Wilcox, D., Schuman, A, **Iyer, V.,** Le, R., Gengler, J., Ferdinandus, M., Liebig, C., Pan, L., Xu, X., and Boudouris, B. Tailored Thioxanthone-based Photoinitiators for Two-Photon-Controllable Polymerization and Nanolithographic Printing, *Journal of Polymer Science, Part B:Polymer Physics.*57 (21) 1462-1475, 2019.
5. Yao, Q., Guo, L., **Iyer, V.**, Xu, X. Ultrafast Electron–Phonon Coupling at Metal-Dielectric Interface, *Heat Transfer Engineering*. 40:13-14, 1211-1219, 2019.
6. **Iyer, V.**, Chen, Y., Xu, X. Ultrafast Surface State Spin-Carrier Dynamics in the Topological Insulator Bi_2Te_2Se, *Physical Review Letters*. 121 (2), 026807, 2018.
7. Chen, C., **Iyer, V.**, Du, Z., Xu, X., Pan, L. Ultrafast Time-Resolved Measurement of Energy Transport at the Metal-Liquid Interfaces, *Applied Physics Letters*. 112 (25), 253105, 2018.
8. **Iyer, V.**, Ye, P., Xu, X. Mid-infrared Ultrafast Carrier Dynamics in Thin Film Black Phosphorus, *2D Materials*. 4 (2), 021032, 2017.